GIUSEPPE DILILLO

HERMES MISSION

RADIATION DAMAGE AND IMPLEMENTATION OF SDD-SCINTILLATOR COUPLED DETECTORS

GIUSEPPE DILILLO

HERMES MISSION

RADIATION DAMAGE AND IMPLEMENTATION OF SDD-SCINTILLATOR COUPLED DETECTORS

Relatore: Prof. ANNA GREGORIO | Correlatore: Prof. FABRIZIO FIORE
Controrelatore: Prof. MAURO MESSEROTTI

Department of Physics
Università di Trieste
22 October 2018

Giuseppe Dilillo: *HERMES mission* , Radiation damage and implementation of SDD-Scintillator coupled detectors, October 2018

Questo lavoro è dedicato alla memoria di un amico, Daniel Langlotz.
1991 – 2016

ABSTRACT

HERMES is a project which aims at providing an all-sky monitor for the prompt localization of high-energy transients - such as Gamma Ray Bursts - with arcmin uncertainty through a network of satellites. HERMES will be capable of autonomously investigate transients' sub-millisecond time structure while providing an unprecedented broad-band spectroscopy which spans the energy range between 1 keV and 1 MeV. The project will allow the study of the radiation mechanisms, the jet composition and the activity of the inner engine behind the still mysterious gamma ray bursts prompt emission.

The realization of a full constellation system depend on the success of HERMES Pathfinder missions, in which framework this thesis will unfold. These missions are funded by ASI and the EU H2020 programme and are currently under development.

An unique Silicon Drift Detector-Scintillator coupled detector is HERMES's enabling technology. The leakage current in silicon drift detectors is expected to increase with space radiation exposure leading to a progressive degradation of the spectroscopic performances. For the sake of this study, we have estimated a worst case scenario in increase the of leakage current due to trapped protons after 6 months, 1 year and 2 years of orbital operations over a wide variety of inclinations and initial altitudes of 500 km and 550 km. The low-Earth trapped protons radiation environment was estimated with the NASA-CCMC's AP8 model package, considered as the standard for radiation belt modeling by ESA. Realistic orbit degradation was taken into account using calculations performed by the Aerospace Science and Technology Dept. of *Politecnico di Milano* specifically for HERMES.

The scintillator selected for HERMES application is Gadolinium Aluminium Gallium Garnet (GAGG): a novel and promising crystal which has never flown before. During the week spent at Bologna INAF laboratory, we studied the performances of a simple SDD-scintillator optical coupling technique: a teflon-wrapped GAGG crystal coupled to a SDD by its polished face and silicon grease. After a careful system set-up, we measured the scintillator's effective light output and energy resolution. A relatively low effective light output was achieved, indicating poor efficiency for this simple coupling technique.

Both the studies should be intended in the grand scheme of efforts preliminary to the opening of the detector test campaign that will be held at the Trento Institute for Fundamentals Physics Applications in winter 2019.

SOMMARIO

Il progetto HERMES intende realizzare una costellazione di microsatelliti che possa servire come monitor per una rapida localizzazione di fenomeni astronomici transienti delle alte energie provenienti dall'intera sfera celeste - come i lampi gamma veloci - con incertezze nell'ordine dell'arcominuto. HERMES sarà capace di portare avanti una propria campagna di osservazioni con lo scopo di indagare la struttura temporale fine dei transienti al di sotto del millisecondo e fare spettroscopia dei transienti su una banda energetica di inedita estensione. Questo renderà possibile studiare i meccanismi di radiazione, la composizione dei jet relativistici e l'attività del motore centrale responsabile dell'emissione dei lampi gamma.

La realizzazione di HERMES nella sua configurazione finale, una costellazione di piu' di 50 microsatelliti, dipende dalla buona riuscita delle missioni HERMES Pathfinder. Le missioni HERMES pathfinder sono state finanziate da ASI e dal programma europeo H2020 e costituiscono l'argomento di questa tesi.

La chiave per la buona riuscita del progetto è da ricercarsi nella corretta implementazione e caratterizzazione del sistema di detector pensato per HERMES: un innovativo sistema accoppiato di scintillatore e camera a deriva di silicio.L'impatto della radiazione spaziale sui detector al silicio comporta un incremento della corrente di buio e quindi un progressivo degradarsi delle performance spettroscopiche. In questa tesi, abbiamo stimato l'incremento della corrente di buio dovuto all'interazione tra detector e protoni energitici facendo uso di modelli SPENVIS dell'ambiente di radiazione, in conformità con gli standard ESA. Lo studio è stato effettuato per una varietà di orbite ad altitudine iniziale 500 km e 550 km e diverse inclinazioni, considerando periodi di attività orbitale di 1 mese, 1 anno e 2 anni. Il decadimento orbitale è stato analizzato e tenuto in conto facendo uso di simulazioni realistiche operate specificamente per le unità HERMES dal Dipartimento Scienze e Tecnologie Aerospaziali del *Politecnico di Milano*.

Lo scintillatore (GAGG) selezionato per i detector di HERMES è un nuovo e promettente cristallo mai impiegato prima dall'industria aerospaziale. Presso i laboratori del centro INAF di Bologna, abbiamo studiato le performance di una strategia di accoppiamento ottico tra cristallo scintillatore e camera a deriva di silicio: un campione di GAGG fasciato con teflon posto a contatto ottico con una camera a deriva di silicio mediante un tappetino di silicone. Dopo aver installato e caratterizzato le componenti della catena spettroscopica, abbiamo misurato risoluzione energetica e uscita luce del cristallo scintillatore in questa configurazione di accoppiamento. È stato misurato un basso

valore di uscita luce efficace indicativo della scarsa efficienza della semplice strategia di accoppiamento adottata.
Entrambi gli studi vanno intesi nel contesto delle operazioni preliminari all'apertura della campagna di test sui detector di HERMES, che verrà aperta il prossimo inverno presso le strutture del Trento Institute for Fundamentals Physics Applications.

RINGRAZIAMENTI

In primo luogo sento il dovere di ringraziare la guida della relatrice di questo lavoro, Prof.ssa Anna Gregorio, del correlatore Prof. Fabrizio Fiore e del contro-relatore Prof. Mauro Messerotti.
In particolare, ringrazio la Prof.ssa Gregorio per essere stata un esempio straordinario di dedizione al lavoro, preparazione e umanità. Spero un giorno di poter rappresentare queste qualità per qualcuno almeno la metà di quanto lei abbia fatto per me. Ringrazio il Prof. Fiore per essere stato una fonte di ispirazione scientifica insostituibile, nonchè per avermi dato l'opportunità di partecipare al progetto HERMES in primo luogo. Infine, se posso dirmi finalmente soddisfatto da questo lavoro, lo devo alla revisione e ai consigli del Prof. Messerotti. Continuerò a tenerli a mente e farò del mio meglio per applicarli ai miei futuri lavori. Sono grato di aver avuto la fortuna di essere un loro allievo e li porterò nel cuore come alcuni dei migliori maestri incontrati durante il mio ciclo di studi.
Ringrazio Riccardo Campana, Daniela Cirrincione, Fabio Fuschino e Claudio Labanti per avermi accolto affettuosamente nella famiglia HERMES e per avermi seguito nella settimana di laboratorio tenutasi a Bologna, da cui ho imparato molto.
Ringrazio la Dott.ssa Lara Nava per il suo affascinante lavoro scientifico, la gentilezza e i preziosi consigli sulla stesura dei primi due capitoli di questo lavoro di tesi.
Un grazie affettuoso va anche a Titti Desario e Sara Bucciarelli per avermi aiutato con la lingua e l'ortografia.
Concludo ringraziando la mia famiglia, senza la quale questo momento semplicemente non sarebbe stato possibile.

Il lavoro che segue è stato realizzato nonostante la cattiva compagnia e la discutible influenza di Alessandro Angioi, Jacopo Bassi, Laura Cataldi, Marco Delvecchio, Matilde Ferrante, Francesco Lomuscio, Antonio Ricatti, Antonio Rosa e Amanda Vecchiato.

CONTENTS

LIST OF FIGURES

LIST OF TABLES

ACRONYMS

ACS	Attitude Control System
ADC	Analog-to-Digital Converter
ASIC	Application Specific Integrated Circuit
BEE	Back-End Electronic
BNS	Binary Neutron Stars
FEE	Front-End Electronics
GAGG	Gadolinium Aluminium Gallium Garnet
GBM	Gamma-ray Burst Monitor
IPN	InterPlanetary Network
LEO	Low Earth Orbit
LOFT	Large Observatory for X-ray Timing
NIEL	Non-Ionizing Energy Loss
PCB	Printed Circuit Board
RAAN	Right Ascension of the Ascending Node
SDD	Silicon Drift Device

INTRODUCTION

This thesis is divided into two major parts.
In the first part we analyse the physics and the motivations behind the HERMES mission.
Multi-messenger astronomy is the field that has begun to characterize single cosmic events through different signal 'messengers' such as gravitational waves and electromagnetic radiation. In Chapter 1 we will briefly discuss the state of the art of multi-messenger astronomy and its motivating influence over HERMES missions design. HERMES's spacecrafts will observe Gamma-Ray Bursts (GRBs) and other high-energy transients - the subject of Chapter 2 - possibly associated to gravitational events. Not only will HERMES have a supportive role in multi-messenger astronomy, but it will also be capable of making new, exciting science on its own. How this will be possible within the framework of small (and cheap) microsatellites will be discussed in Chapter 3, from which the second part of this thesis builds on.
The first original result will be presented in Chapter 4: an estimate of the increase in the leakage current of HERMES's silicon drift detector expected from space radiation exposure, calculated for a wide variety of realistic orbits after different orbital activity periods. During the last week of July 2018 we held a hand-on analyses on the detector system at the INAF laboratories in Bologna, the goal of which has been to characterize the performances of a particular solution for scintillator implementation and to train with a full-fledged silicon detector system in a laboratory environment in view of the upcoming HERMES detector test campaign.
The results of this analyses will be presented in Chapter 5.
Finally, we will draw conclusions and discuss the possible future developments of this work.

Part I

THE PHYSICS OF HERMES

1

MULTI-MESSENGER ASTRONOMY

In this chapter we will cover the state of the art of multi-messenger astronomy, the field that has recently begun to characterize single cosmic events through multiple signal types, and its relation to gamma-ray bursts.

In Section 1.1 the observations and results of the joint observation of gravitational signal from a neutron stars mergers and a short gamma ray bursts of the 17 August 2017 are presented. Particular attention will be payed to the role played by Fermi and INTEGRAL space observatories. Understanding their role in the successes of the 17 August 2017 implies understanding the urge for an all-sky gamma ray bursts monitor for prompt emission localization in the next decade, henceforth HERMES. The challenges that the next decade poses to multi-messenger observations and the state of the art of X-ray space observations will be the object of Sections 1.2 and 1.3.

1.1 A CRUCIAL DAY IN ASTROPHYSICS: AUGUST 17 2017

August 17 2017 12:41:06 UTC, the Gamma-ray Burst Monitor (GBM) instrument aboard the Fermi Space Telescope is triggered by a Gamma-ray Burst (GRB). The GRB was soon classified and localized, and later designated as GRB170817.

Just 6 minutes later, based on a single-detector analyses of the Laser Interferometer Gravitational-wave Observatory (LIGO) Hanford data, a gravitational-wave event is registered. The same signal is detected at LIGO-Livingston and Virgo interferometers. In a similar fashion to the GRB, it will be named GW170817. The signal was soon determined to be consistent with a binary neutron stars coalescence event with merger time t_c =12:41:04 UTC, ending less than 2 seconds before GRB170817 triggered the GBM instrument.

A Gamma-ray Coordinates Network notice is issued at 13:21:42 UTC, reporting that a highly significant gravitational wave candidate event consistent with a binary neutron star coalescence was associated with the time of the GRB. A rapid re-analyses of data from LIGO-Hanford, LIGO-Livingston and Virgo confirmed a highly significant, coincident signal. The data from the three interferometers were combined. The first three-instrument skymap is produced at 17:54:51 UTC, five hours after the first detection. It places the source nearby, at a luminosity distance about 40 ± 8 Mpc from Earth, somewhere in an elongated region of the celestial sphere covering about 31 deg^2.

Source localization

The source position is also constrained by Fermi-GBM data analyses

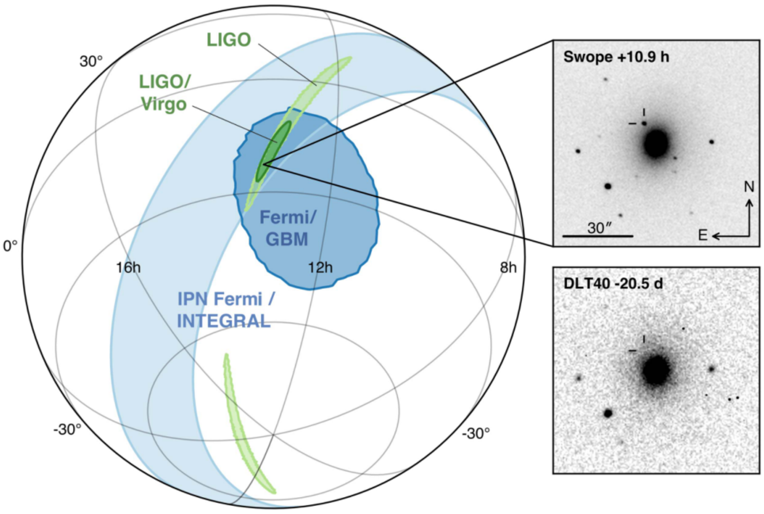

Figure 1.1: Localization of the gravitational-wave, gamma-ray, and optical signals. The left panel shows an orthographic projection of the 90% credible regions from LIGO (190 deg^2 ; light green), the initial LIGO-Virgo localization (31 deg^2 ; dark green), IPN triangulation from the time delay between Fermi and INTEGRAL (light blue), and Fermi-GBM (dark blue). The inset shows the location of the apparent host galaxy NGC4993 in the Swope optical discovery image at 10.9 hr after the merger (top right) and the DLT40 pre-discovery image from 20.5 days prior to merger (bottom right). The reticle marks the position of the transient in both images [2].

to a region of $\sim 1000\ \text{deg}^2$ overlapping that identified by the ground interferometers. Observed time delay between the signal detected by Fermi and spacecraft INTEGRAL's spectrometer SPI make possible for triangulation of GRB position. The electromagnetic signal was coming from a region of $\sim 100\ \text{deg}^2$ extended along the area identified by the ground interferometers, as in Figure 1.1.

Both Fermi and INTEGRAL analyses agreed in classifying the burst as a *short* GRB, a subclass of burst with duration less than 2 seconds. During the 2000's, strong theoretical hints suggested an association between short GRBs and mergers of neutron stars with other neutron stars or black holes. Neutron star binary mergers were expected to be associated with isotropic electromagnetic signal which included optical and infrared emission, the *kilonova*, and delayed radio emission from interaction between ejecta and the circumburst matter. It is hardly suprising that the announcements of FERMI and LIGO-Virgo detections was hailed with immense enthusiasm from different research groups all around the world. Astrophysicists were finally having a chance to directly prove their models of bursts and binary mergers, and the relations between the two. However, by this time, the fact that the two signals were in fact coming from the same source was still to be established with statistical certainty. In order to do so, promptly

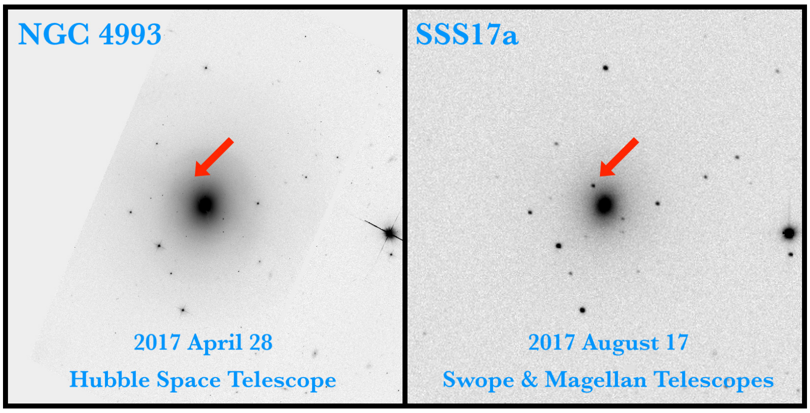

Figure 1.2: The UC Santa Cruz - 1M2H team found SSS17a by comparing a new image of the galaxy N4993 (right) with images taken four months earlier by the Hubble Space Telescope (left). The arrows indicate where the transient event SSS17a was identified absent from the Hubble image and visible in the new image from the Swope Telescope [9].

localizing an optical counterpart to the event was top priority. In order to rule out the possibility that the two signals were related by chance, scientists had to identify an host galaxy that was: 1. located at a distance compatible with the LIGO data and 2. exhibiting unexpected activity related to the burst emission.
An unprecedentedly large broadband campaign of observation soon started. An optical transient counterpart, SSS17A (Figure 1.2), was observed from Chile for the first time at $t_c + 10.87$ hr by the One-Meter, Two-Hemisphere team. The transient was associated with the galaxy NGC4993 at distance ~ 40 Mpc, in line with the gravitational-wave source distance. In the following two weeks, different telescopes from all over the world investigated the fading electromagnetic counterpart of GW170817 in bands spanning the entire spectra between IR and UV, looking for activity related to the burst emission. The evolution of the spectral energy distribution, particularly the IR emission features, were suggesting that the source was coherent with theoretical models of kilonovae.

Optical counterpart

IR and UV observations

For the first time direct observations were supporting the hypothesis that GW170817 was produced as a result of the merging of two neutron stars in galaxy NGC4993 and that the event was in fact followed by short GRB GRB170817 and a kilonova, as predicted by theory.

If UV to IR observations made possible to study sub-relativistic ejecta, an analyses of fast-moving matter resulting from the coalescence event could not prescind from observations in the X and Radio bands. Chandra and VLA were the first observatories to claim founding afterglows to GW170817 in X and Radio bands respectively.

X and radio emission.

NGC4993's X and Radio emissions have been closely monitored in the months following August 2017, making possible to constrain the geometry and dynamic of the event.
In particular, the standard model for short GRB afterglows describes these in term of synchrotron emission from a decelerating and decollimating relativistic jet, as we will see in 2.4. Recent studies purposed the presence of an additional, slower-moving component: the cocoon. These models predict that if the jet initially propagates through a baryon contaminated region surrounding the merger site, a hot cocoon forms around it from which the jet could emerge collimated (successful jet) or not emerge (choked jet). The cocoon subsequently expands almost isotropically producing its own prompt emission and external shock powered afterglow [.]
Very long-baseline interferometry radio observations seem to suggest a very precise scenario in which early-time radio emission was powered by the cocoon while the late-time emission was dominated by an energetic and narrowly collimated jet, observed from a viewing angle of about 20 degrees [.] This observation seems to suggest GW170817 did launch in fact a successful relativistic jet and provides new evidence linking BNS mergers and short bursts.

1.2 CHALLENGES TO THE NEXT DECADE OF MULTI-MESSENGER OBSERVATIONS

We can identify the key point that made characterization of GW170817 event possible: the quick identification of an optic counterpart to the event in galaxy NGC4993. The unambiguous identification of a source has in turn been possible only thanks to the relatively closeness of the event at 40 Mpc and the combined Advanced Ligo/Virgo - GBM ~ 30 deg^2 accuracy. These made possible to reduce the sources pool to just ~ 50 candidate galaxies.
In the next decade LIGO is expected to improve its sensitivity while two new detectors will become operational: the japanese KAGRA and the indian third detector of the LIGO family, colloquially known as IndIGO. If, on one hand, the enlarged detector network will make possible for improved localization accuracy below ~ 10 deg^2, on the other hand, a large fraction of the BNS events will be discovered at increasing distance, up to almost 200 Mpc, because of improvement to LIGO detector sensitivity. With increasing source distance come an increasing source candidate pool, hosting possibly thousands of galaxies. A larger candidate pool makes for hard unambigous, prompt identification of the source. Will the new interferometers positioning accuracy be enough to keep the pace with increasing detection distance? Making use of simple geometry we can assert that this will not be the case and that *arcmin localization* will reveal to be the goal accuracy in the next decade of multi-messenger astronomy observations.

Gravitational interferometry in the 2020s

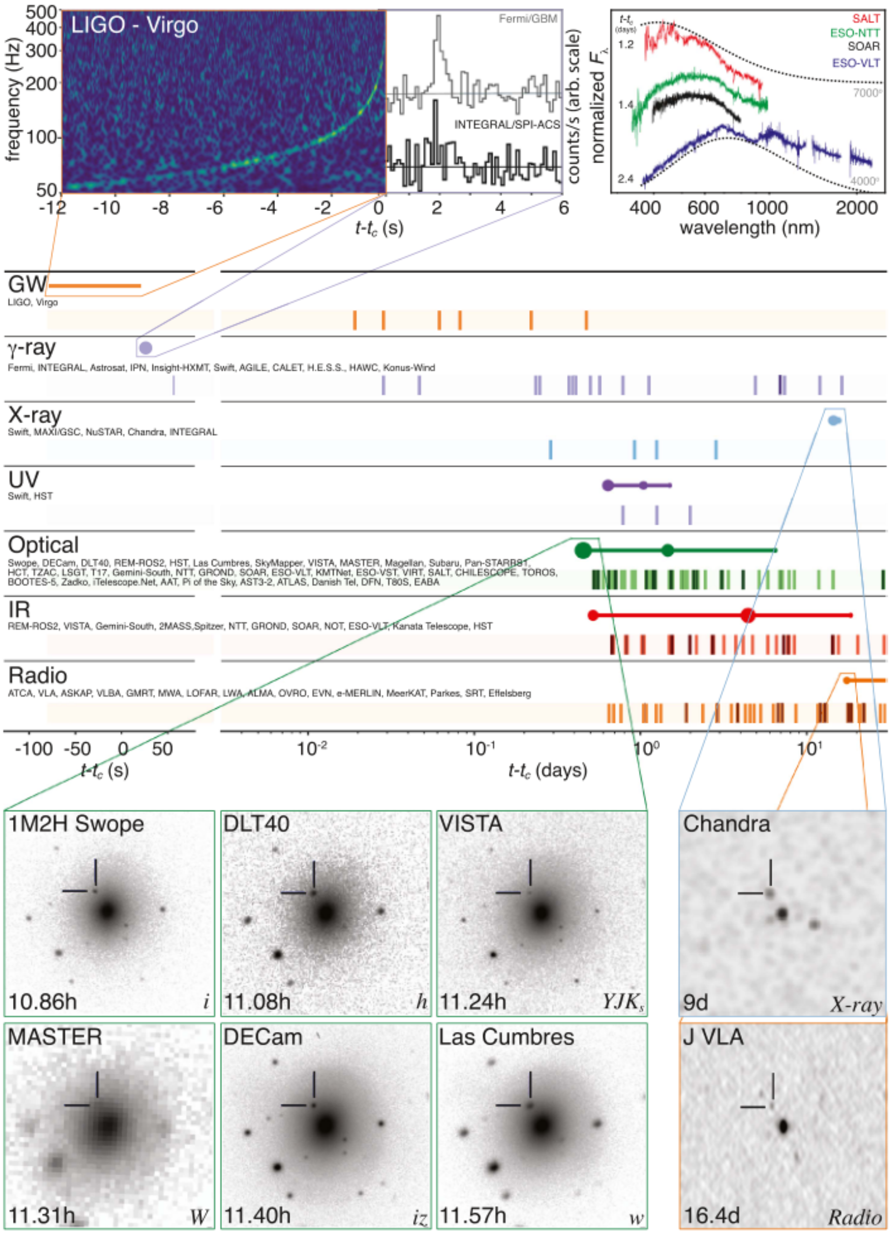

Figure 1.3: Timeline of discover of GW170817, GRB170817*A*, SSS17a and follow-up studies by different messenger and wavelenght relative to the time of observations. From top left to bottom right, magnification inserts give a picture of the first detections in the gravitational-wave (LIGO), gamma-ray (FERMI-GBM, INTEGRAL), optical (spectra and imaging, see didascalies), X-ray (Chandra) and radio band (JVLA) [2].

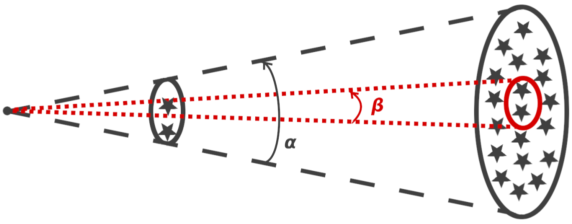

Figure 1.4: Number of sources in a patch of sky grows with the third power of the distance. In order to guarantee prompt optical counterpart detection, in the next decade localization accuracies in the order of the arcmin will be necessary.

We will determine the localization accuracy needed to keep the source pool in the range of few tenth of units, as it did happen in NGC4993 identification during August '17.

Arcmin localization

With reference to Figure 1.4, we assume the spherical region at left, representing the GRB-LIGO/Virgo area of detection, to be distant $d \sim 40$ Mpc and containing ~ 50 candidate sources, as during August 2017. The angular extension of this region is $\alpha \sim \sqrt{30}$ deg. At right, in black, we suppose to have a spherical region at distance $d' \sim 200$ Mpc with angular extension still $\sim \alpha$. We neglect cosmology and suppose the galaxies to be distribuited uniformly through the sky. The number of candidate galaxies in this region is $50 \cdot d'^3/d^3 \sim 3200$. Depicted in red we have a second, smaller, region at distance $d' = 200$ Mpc with angular extension $\sim \beta$. In order to have this region containing 50 sources, just as supposed for the first one, the angular extension should be $\beta \sim \alpha \cdot d/d' \sim 10$ arcmin.

In addition to the new generation of gravitational interferometers, the next decade is expected to bring us a major boost in the ground study of very high-energy electromagnetic sources.

CTA: A new generation of fast-slewing ground gamma telescopes

The Cherenkov Telescope Array (CTA) is expected to come online by 2022. CTA will consist of two arrays of telescope covering the northern and southern hemisphere. They will look the sky in the energy band between 20 GeV and 300 TeV providing 'tenfold increase in the number of known gamma-ray-emitting celestial objects' [57]. The CTA fast re-positioning capabilities (20 seconds) and the largely improved sensitivity as compared to Fermi-LAT makes the study of GRB high-energy afterglow radiation possible and appealing.

Since CTA will have limited field of view while operating at GeV energies (4.3 deg), in order to guarantee the telescopes afterglow observation, it is necessary to employ an instrument able to first provide source localization with accuracy better than a few degrees.

1.3 X-RAY ASTRONOMY OBSERVATIONS, STATE OF THE ART AND NEAR FUTURE

In this paragraph we will briefly review the current state of the X-Ray space telescopes fleet. In particular, we will try to answer: are we prepared enough to confront the next decade of multi-messenger astronomy observation?

To date, the missions devoted to the search and study of hard X-Ray transients are NASA's SWIFT and Fermi.

- Fermi is orbiting Earth since 2008 and hosts the GBM experiment, consisting of 12 sodium iodide and 2 bismuth germanate scintillators. The field of view covers almost two-thirds of the celestial sphere, the whole portion of the sky not occluded by Earth. The Large Area Telescope (LAT) is an imaging gamma-ray detector able to detect photons with energy raging from 20 MeV to 300 GeV, with a field of view of about 20% of the sky. Combining GBM and LAT, Fermi is able to cover a broad energy band from 50 keV to 300 GeV. Accuracies in the energy interval of interest - up to a few MeV - are of the order of ten squared degrees.
- SWIFT has been launched in 2004. It is equipped with BAT, a coded mask instrument operating between 15 and 150 keV with a field of view around 1/6 of the full sky. Alongside BAT, XRT is a narrow field X-Ray telescope able to provide localization of weak sources with arcseconds accuracy.
- INTEGRAL has been launched in 2002. IBIS camera operates between 10 and 150 keV with arcmin positioning accuracy and a field of view around one thousand squared degrees.
- AGILE has been launched in 2007. SuperAGILE experiment operates between 15 and 45 keV with ~ 3000 deg^2 field of view and allows localization with accuracy of a few arcmin for bright sources.

All of them are actually working after more then 10 years, beyond their predicted lifetime. The equipment and instruments aboard are ageing and it is unknown for how long they will be serviceable after the 2020. All sky monitors feature either coded-mask instruments read by cadmium zinc telluride scintillator crystals or standard scintillator crystals, poor performing by today standard.
ESA L2 mission Athena, boarding the most sensitive X-ray telescope ever built (XIFU), is expected to launch not before the end of 2020s.

In March 2018, ESA selected the interesting THESEUS mission to enter assessment phase study. Featuring a unique payload package, THESEUS proposes to investigate high redshift, high energy transients phenomena in order to better understand early universe astrophysics. However, if approved, THESEUS won't be online until the end of 2020s.

No present X-ray astronomy facility will be able to serve the pivotal role of an all-sky monitor with arcmin or better localization capability. At the same time, it is mandatory to such a role to be covered if we want to seize the incredible opportunities coming from the next decade of observations in the field of multi-messenger observations.

2

GAMMA RAY BURSTS

In this chapter we will cover the physics necessary to understand the gamma ray bursts prompt emissions. In Section 2.1 an overview of the history of gamma ray bursts observations will be presented. It will be an occasion to familiarize with the observational approach to these astrophysical events and gamma ray bursts key features, which will be the object of Section 2.2. The theory of prompt emission will be covered in Sections 2.3, 2.4 and 2.5. Understanding the issues in the current knowledge of prompt emission mechanism is the key to appreciation of the brilliance behind the design of HERMES detector, which is the subject of the studies presented in this thesis. In Section 2.7 HERMES scientific goals are systematically introduced for the first time.

2.1 HISTORY OF GRB OBSERVATIONS

On August 5 1963, after a decade of negotiation, the world nuclear superpowers agreed on signing the "Partial Nuclear Test Ban Treaty". The treaty provided for the immediate interruption of nuclear weapon test in the atmosphere, underwater, or outer space. On the same year, the US Air Force deploy to orbit the first Vela satellite. The goal of this satellite, and of the many Vela that will follow, was to grant the adherence of other nations, in particular the soviets, to the ban.

The Vela satellites

The Vela satellites orbited Earth well above the Van Allen Radiation Belt and were equipped with X-ray, gamma-ray and neutron detectors. All these types of emission were in fact expected from nuclear blast and the altitude of the orbit was intended to avoid the noise resulting from high energy particles in Van Allen Radiation Belt.

Vela satellites localized gamma ray burst measuring delays in signal's arrival time between different units.

The Vela system was composed by four satellites operating at the same time. Having different satellites simultaneously operating made possible for localization of possible nuclear test: since the light travels at finite speed, time difference between the arrival of a signal to detectors hosted by different spacecraft would result in a crude estimate of the angle of radiation incidence with respect to the satellite position, therefore the direction of any nuclear explosion.

On 2 July 1967 the satellites Vela 4 and Vela 3 detect a flash of gamma radiation. It lasted for around 2 seconds, six orders of magnitude above the expected duration of gamma flashes resulting from nuclear explosion. The origin was unkown. Supernovae and solar flare both could be responsible for such an event but neither were observed on that day.

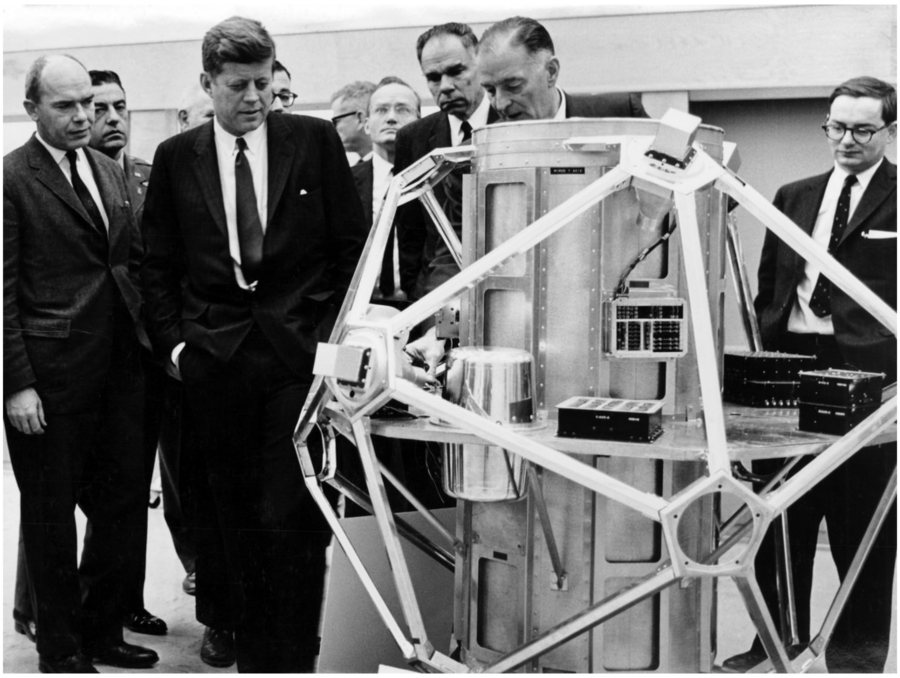

Figure 2.1: The US president John Fitzgerald Kennedy inspects a VELA satellite at SANDIA labs during December 1952. Credits: Sandia Labs.

The team researching the phenomena was based at Los Alamos Scientific Laboratory and led by Ray Klebesadel. Established the absence of any particular military risk, further studies about the mysterious flashes were delayed to later investigation. In 1972, the same Los Alamos National Laboratory team reanalyzed the data from the previous decade and determined that in fact a number of gamma flashes were observed. Moreover, all these events seemed to be originating well beyond our cosmic neighborhood, since their distribution across the sky soon made clear how those were not related to the Sun, the moon or any other body in our solar system.

The first GRB was observed in 1967 and announced in 1973

In 1973 the discovery of Gamma-Ray Bursts (GRBs) was announced to the public. In the famous paper 'Observations of Gamma-Ray Bursts of Cosmic Origin', Ray Klebesadel, Ian Strong and Ray Olson claim the discovery of 'sixteen short bursts of photons in the energy range of 0.2-1.5 MeV' coming from sources different from the Earth and the Sun. The abstract of the milestone paper is presented in Figure 2.2. The announcement of GRBs discovery was hailed with comprehensible enthusiasm by the astronomer and astrophysicist community. No well known phenomena reached GRB observed flux between hard X and gamma spectrum but no optical counterpart were identified. This immediately steered the attention towards compact, extreme cosmic objects such as black holes or neutron stars. However, the large flux was calling for source to be located nearby. If solar system was to rule out, was it possible that black holes were crowding the disk of our own galaxy? Similar questions surrounded the subject. As a matter of fact, a multitude of theories were proposed in order to explain the origin of such phenomena through the 1970's and the 1980's, no one really providing solid arguments.

GRBs observation during the 1970's and the 1980's: the Inter-Planetary Network

It was soon clear that in order to take a step further towards comprehension of GRBs a better understanding of the location of such burst was needed. Accepted as matter of fact that localization through measurement of time delay was still the route to follow, astronomers found themselves at a crossroads. In order to improve their source localization accuray, they could: 1. enlarge the network of satellites. 2. develope new instrumentations and algorithm in order to improve errors on spacecraft's location, absolute time and signal cross-correlation. 3. space the detectors farther apart.
This is really apparent when considering equation 3.1.
Increasing the number of networked detectors through dedicated spacecraft would reveal extremely cost inefficient. On other hand, working on the instrumentation and algorithm was feasibile only to a certain extent. During the 1970's, global navigation systems were still in their early days and often out of reach for applications outside the military. This severely constrained how good absolute time and position of the spacecrafts composing the network could be known.
Scientists choose to follow the last path: complementing the existing Vela satellites with new spacecrafts spaced farther apart. In order to do so, it was deemed necessary to spread the detectors thorugout the solar system. Instrumentation for gamma ray detection was boarded on satellites that would soon be launched towards outer space.
The first Inter-Planetary Network (IPN) was completed by the end of 1978. The IPN included 5 new space probes orbiting Earth, Sun and Venus: soviet Prognoz 7, german Helios 2 and the NASA's Pioneer Venus Orbiter, Venera 11 and Venera 12.
By 1987, IPN identified more than 200 GRB. However, the large uncer-

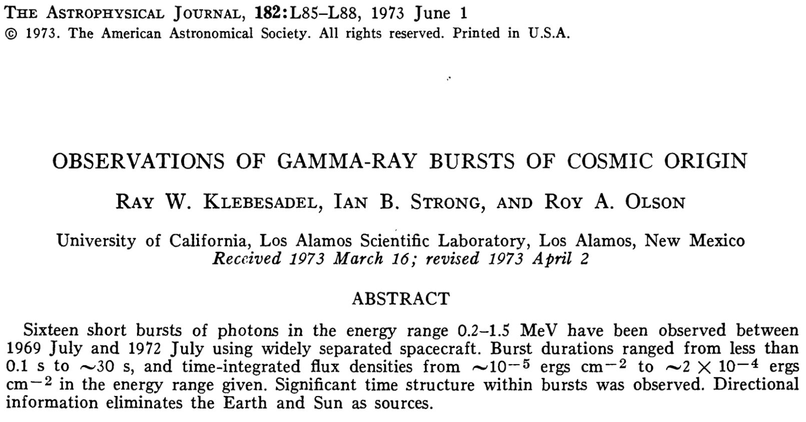

THE ASTROPHYSICAL JOURNAL, **182:**L85–L88, 1973 June 1
© 1973. The American Astronomical Society. All rights reserved. Printed in U.S.A.

OBSERVATIONS OF GAMMA-RAY BURSTS OF COSMIC ORIGIN

RAY W. KLEBESADEL, IAN B. STRONG, AND ROY A. OLSON

University of California, Los Alamos Scientific Laboratory, Los Alamos, New Mexico
Received 1973 March 16; revised 1973 April 2

ABSTRACT

Sixteen short bursts of photons in the energy range 0.2–1.5 MeV have been observed between 1969 July and 1972 July using widely separated spacecraft. Burst durations ranged from less than 0.1 s to $\sim$30 s, and time-integrated flux densities from $\sim 10^{-5}$ ergs cm^{-2} to $\sim 2 \times 10^{-4}$ ergs cm^{-2} in the energy range given. Significant time structure within bursts was observed. Directional information eliminates the Earth and Sun as sources.

Figure 2.2: The abstract of the first paper announcing to the public the discovery of Gamma-Ray Burst by military US satellites VELA. [28]

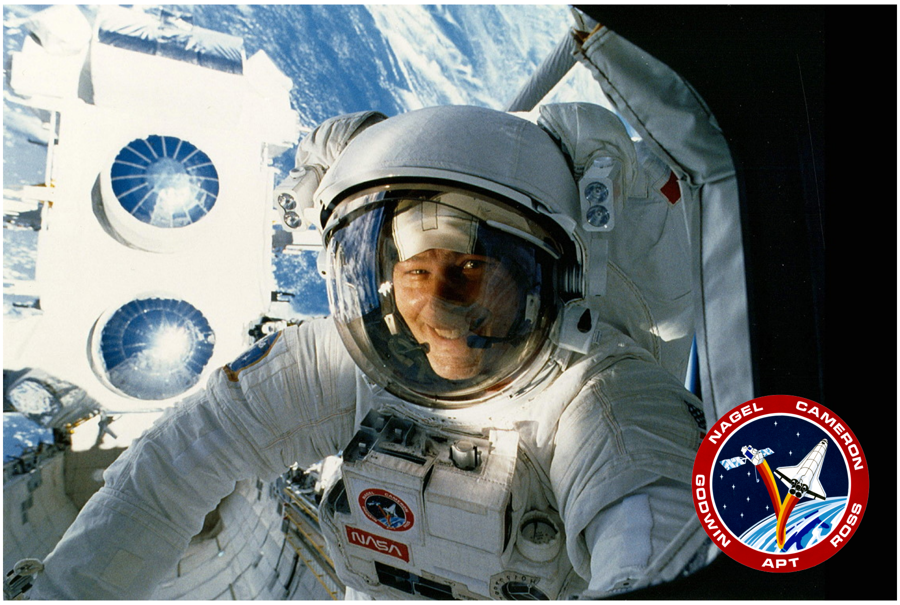

Figure 2.3: April 1991, Compton Gamma Ray Observatory (CGRO) is held upright in the Atlantis space shuttle's payload bey during deployment operations. In foreground, astronaut Jeremy Ross smiles during extravehicular activity on an high-gain antenna. At lower right corner the insignia of the shuttle mission STS37. Credit: NASA/Ken Cameron.

tainties and the difficulties associated to combine and inter-calibrate different instruments hindered the breakthrough scientists were waiting for.

At the very beginnning of the 1990's most theories about GRBs agreed implying that the mysterious bursts were originating from possibly exotic sources inside our galaxy.
In April 1991, as part of the NASA's "Great Observatories" program, the 17 tons Compton Gamma Ray Observatory (CGRO) was launched from space shuttle Atlantis. Compton was a real space observatory dedicated to photon detection between 20 keV and 30 GeV.
Part of CGRO payload was the instrument Burst and Transient Source Experiment (BATSE). Due to unprecedented sensibility - BATSE was almost 10 times more sensible than previous IPN detectors - it was able to detect GRBs at impressive rate, roughly around one per day. BATSE activity lasted until end of mission and de-orbit in 2000.
BATSE for the first time made possible to develop a significant statistics of gamma-ray bursts. Of the almost 3000 GRBs it discovered, no burst looked the same. The greatest part of GRBs were dim, while a few were briefly the brightest and most energetic object visible. Some lasted a few milliseconds, while other shined on for hours.
However, the most striking discovery that BATSE was responsible of was not achieved looking at any individual burst but at their global

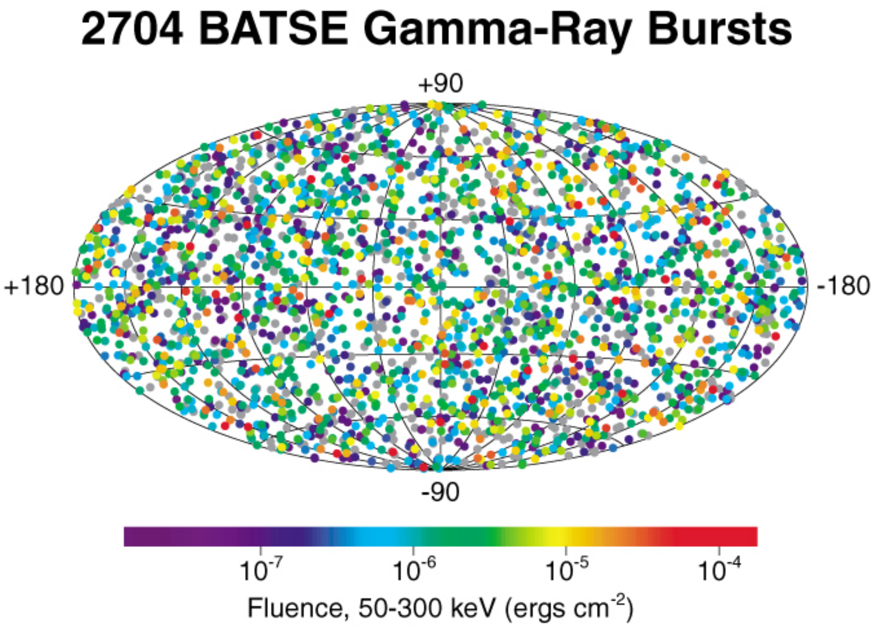

Figure 2.4: Locations of 2704 gamma-ray bursts detected by the BATSE instrument during nine years of observations. The projection is in galactic coordinates; the plane of the Milky Way Galaxy is along the horizontal line at the middle of the figure. The burst locations are color-coded based on the fluence, which is the energy flux of the burst integrated over the total duration of the event. Long duration, bright bursts appear in red, and short duration, weak bursts appear in purple. Grey is used for bursts for which the fluence cannot be calculated due to incomplete data. Statistical multipole studies and weaker occurrence of faint events strongly suggests the sources to be located at cosmological distances, well outside the Milky Way [39].

properties.

Gamma-ray bursts appear to be distributed almost perfectly randomly across the sky i.e. their distributions is *isotropical*.

1991, the BATSE breakthrough: GRBs are isotropically distributed

Figure 2.4 illustrates the locations of 2704 gamma-ray bursts detected by the BATSE instrument during nine years of observations. In 1992 it was already clear that GRBs appear to be isotropically distributed and do not track any known population of galactic object [38]. Further statistical tests confirm that the bursts are isotropically distributed on the sky since no significant dipole moment or quadrupole moment is found [8]. At the same time, a deficiency has been detected in the number of faint bursts, interpreted as an indication that the spatial extent of the burst distribution is limited and that BATSE sees the limit or edge of the distribution [19].

This was the breakthrough scientist were waiting for.

The fact that GRBs appeared isotropically distributed was already known to scientist. IPN measures were obviously in agreement with

that. However, it was expected that a more sensitive instrument such as BATSE would reveal an excess of faint GRBs towards the galactic centre, where stars are more densely distributed, in agreement with the idea that GRBs originated inside the Milky Way.
BATSE showed instead that even the faintest burst were uniformly distributed across space.
Two competing distance scales and environment were emerging for GRB sources: 1. GRB sources were located at galactic distances and, in order to be compatible with BATSE observations, they had to be placed in a massive halo surrounding our Galaxy. It is important to note that even in this scenario a small deviation from isotropy was expected but, since the BATSE catalog was still modestly sized, the galactic hypothesis remained in agreement with the observation. 2. GRB sources were at cosmological distances. Their observed distribution was explained by the Cosmological Principle.
BATSE observations opened a can of worms: the reigning model of 'local' GRB sources was falling apart while the cosmological theory - a fringe hypothesis for all the 1970's and 1980's - gained momentum.
By looking at the number of bursts within a certain brightness range, BATSE also confirmed that it had already the capability to look at nearly the 'edge' of the GRB population.
An observer can in fact infer if him is resolving the border of a population of similarly bright, isotropically distributed object determining if the fainter ones are less frequent than expected. In the galactic and cosmologic scenario the existence of a border for the GRB population carries very different meaning. In the Galactic picture, the number of sources decreases with increasing distance from the galactic centre out to a distance where there are virtually no more left. In the cosmological scenario, the decline is due to the expansion of the Universe: at earlier times in the history of the Universe the volume of space was smaller than it is now, showing up in the distribution of the most distant henceforth faint burst.
BATSE showed also that GRBs were bimodally distributed in their duration and spectral features. *Short bursts* last for less than two seconds in duration and are dominated by higher-energy photons. On the other hand, *long bursts* lasts more than two seconds, with a predominance of lower-energy photons.
In order to explain this distinction, astronomers proposed new models of GRB sources. Long GRBs were supposed to be emitted as result of the collapse of massive stars while short bursts were originating from the merging of neutron stars or neutron stars and white dwarf in exotic binary systems.

By mid 1990's astronomers had searched for counterparts to GRBs for decades. Finding what was emitting the gamma burst also meant finding where the burst were emitted. In light of BATSE recent observation, this was more important than ever since it could end the diatribe around the GRB scale distance. However, the poor resolution of the available gamma detectors prevented this from happening. The best hope seemed to lie in finding a fainter, fading, longer wavelength emission after the burst itself. An *afterglow*, the 'smoking gun' behind the bang.

1997, the BeppoSAX breakthrough: the first afterglow detection

The italian-dutch satellite BeppoSAX was launched from Cape Canaveral on April 30, 1996. Originally named "Satellite per l'Astronomia X" (SAX), it was later renamed BeppoSAX in honour to the italian astrophysicist Giuseppe 'Beppo' Occhialini.

Through different instruments, BeppoSAX was able to cover an unprecedented broad-band of energies, from 0.1 to 300 keV. The mission was thought in order that after the initial detection in the higher part of the spectrum with coarse accuracy, BeppoSAX would have turned on the more sensitive soft-X instruments towards the same area, looking for any fading afterglow with much higher positioning accuracy.

This was indeed what happened on 28 February 1997, leading to the discovery of the first GRB afterglow. A GRB was discovered by the Fermi Gamma-Ray Bursts Monitor (GBM) and the Wide Field Cameras aboard BeppoSAX. The italian scientist responsible for the detector and the mission director were able to reschedule the satellite observations and point the BeppoSAX narrow field X-ray telescopes at the gamma ray source. A few hours later an unknown X-ray source in the constellation of Orion was discovered and localized with accuracy of one hundreth of a degree. After about two days a follow-up observation was performed, showing that the source's flux had dropped by about a factor of 20. In figure 2.5 the images from original and follow up measure are showed and compared. Later images after the point source faded revealed a faint galaxy at almost the same position, the presumed host galaxy of the burst; a chance position coincidence was unlikely but possible, so the cosmological origin of GRBs was not conclusive until a few months later.

On 8 May 1997, BeppoSAX succeded again in detecting GRB970508 and accurately localizing a possibly associated X-ray afterglow. On 10 May a brightening variable optical source was reported within the error box of GRB970508. The following day, a team from the California Institute of Astronomy headed by Mark Metzger took the spectrum of the source making use of the 10-metre Keck telescope. Metzger and his team reported the first discovery of the redshift of a GRB source to be $z = 0.835$, indicating distances well above billion light years.

Gamma-ray bursts are sources at cosmological distances.

It was clear at this point that the GRBs were, by a large margin, the most luminous class of events ever to be detected. From detected

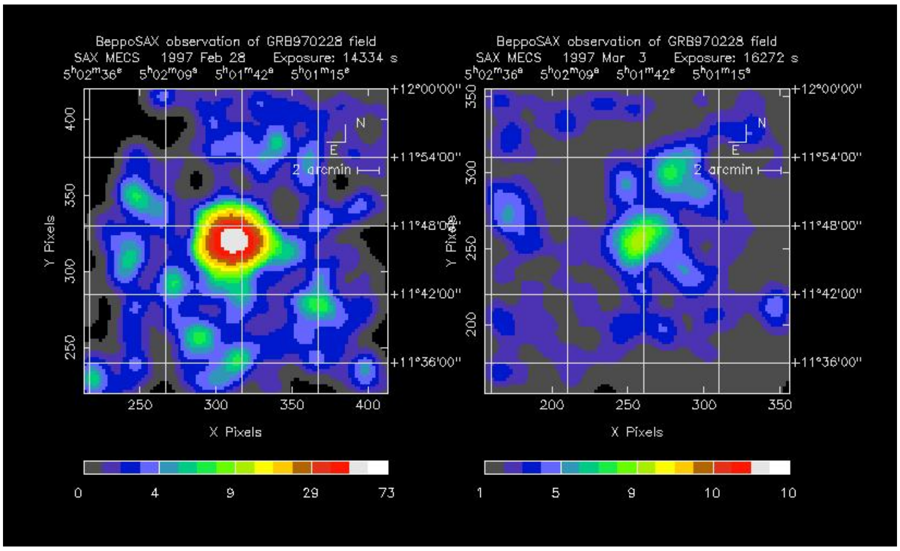

Figure 2.5: Original and follow-up GRB970228 X-ray images by BeppoSAX's Medium Energy Concentrator Spectrometer (MECS) narrow field telescope shows an unknown X-ray source fading over a week. This was the first time a GRB was observed [13].

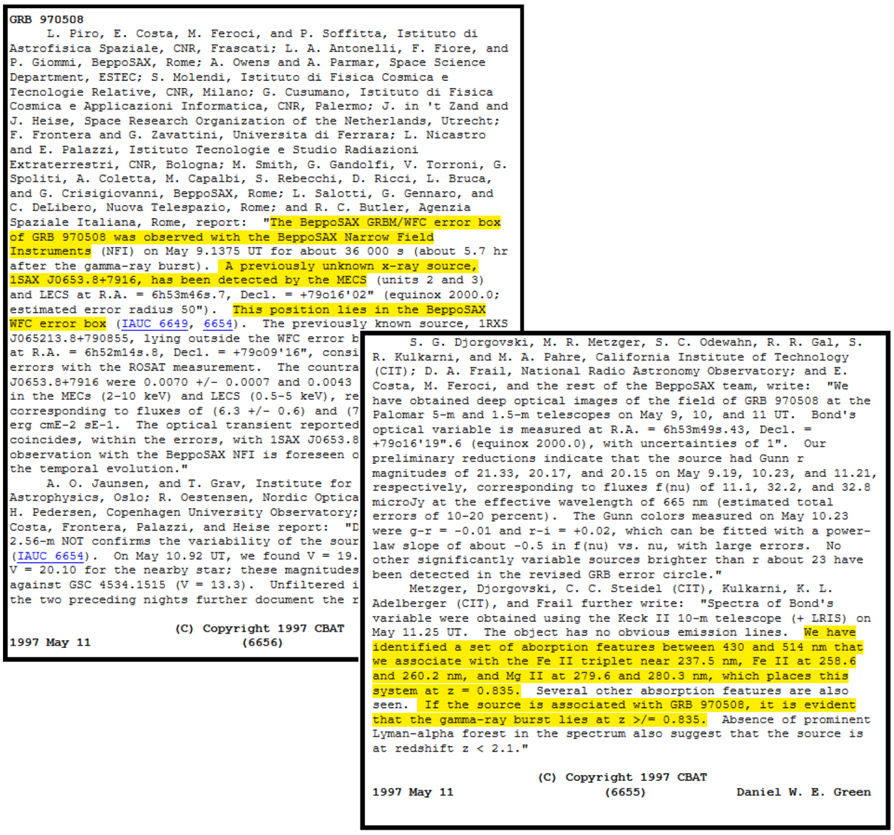

GRB 970508

L. Piro, E. Costa, M. Feroci, and P. Soffitta, Istituto di Astrofisica Spaziale, CNR, Frascati; L. A. Antonelli, F. Fiore, and P. Giommi, BeppoSAX, Rome; A. Owens and A. Parmar, Space Science Department, ESTEC; S. Molendi, Istituto di Fisica Cosmica e Tecnologie Relative, CNR, Milano; G. Cusumano, Istituto di Fisica Cosmica e Applicazioni Informatica, CNR, Palermo; J. in 't Zand and J. Heise, Space Research Organization of the Netherlands, Utrecht; F. Frontera and G. Zavattini, Universita di Ferrara; L. Nicastro and E. Palazzi, Istituto Tecnologie e Studio Radiazioni Extraterrestri, CNR, Bologna; M. Smith, G. Gandolfi, V. Torroni, G. Spoliti, A. Coletta, M. Capalbi, S. Rebecchi, D. Ricci, L. Bruca, and G. Crisigiovanni, BeppoSAX, Rome; L. Salotti, G. Gennaro, and C. DeLibero, Nuova Telespazio, Rome; and R. C. Butler, Agenzia Spaziale Italiana, Rome, report: "The BeppoSAX GRBM/WFC error box of GRB 970508 was observed with the BeppoSAX Narrow Field Instruments (NFI) on May 9.1375 UT for about 36 000 s (about 5.7 hr after the gamma-ray burst). A previously unknown x-ray source, 1SAX J0653.8+7916, has been detected by the MECS (units 2 and 3) and LECS at R.A. = 6h53m46s.7, Decl. = +79o16'02" (equinox 2000.0; estimated error radius 50"). This position lies in the BeppoSAX WFC error box (IAUC 6649, 6654). The previously known source, 1RXS
J065213.8+790855, lying outside the WFC error b
at R.A. = 6h52m14s.8, Decl. = +79o09'16", consi
errors with the ROSAT measurement. The countra
J0653.8+7916 were 0.0070 +/- 0.0007 and 0.0043
in the MECs (2-10 keV) and LECS (0.5-5 keV), re
corresponding to fluxes of (6.3 +/- 0.6) and (7
erg cmE-2 sE-1. The optical transient reported
coincides, within the errors, with 1SAX J0653.8
observation with the BeppoSAX NFI is foreseen o
the temporal evolution."

A. O. Jaunsen, and T. Grav, Institute for
Astrophysics, Oslo; R. Oestensen, Nordic Optica
H. Pedersen, Copenhagen University Observatory;
Costa, Frontera, Palazzi, and Heise report: "D
2.56-m NOT confirms the variability of the sour
(IAUC 6654). On May 10.92 UT, we found V = 19.
V = 20.10 for the nearby star; these magnitudes
against GSC 4534.1515 (V = 13.3). Unfiltered i
the two preceding nights further document the r

(C) Copyright 1997 CBAT
1997 May 11 (6656)

S. G. Djorgovski, M. R. Metzger, S. C. Odewahn, R. R. Gal, S. R. Kulkarni, and M. A. Pahre, California Institute of Technology (CIT); D. A. Frail, National Radio Astronomy Observatory; and E. Costa, M. Feroci, and the rest of the BeppoSAX team, write: "We have obtained deep optical images of the field of GRB 970508 at the Palomar 5-m and 1.5-m telescopes on May 9, 10, and 11 UT. Bond's optical variable is measured at R.A. = 6h53m49s.43, Decl. = +79o16'19".6 (equinox 2000.0), with uncertainties of 1". Our preliminary reductions indicate that the source had Gunn r magnitudes of 21.33, 20.17, and 20.15 on May 9.19, 10.23, and 11.21, respectively, corresponding to fluxes f(nu) of 11.1, 32.2, and 32.8 microJy at the effective wavelength of 665 nm (estimated total errors of 10-20 percent). The Gunn colors measured on May 10.23 were g-r = -0.01 and r-i = +0.02, which can be fitted with a power-law slope of about -0.5 in f(nu) vs. nu, with large errors. No other significantly variable sources brighter than r about 23 have been detected in the revised GRB error circle."

Metzger, Djorgovski, C. C. Steidel (CIT), Kulkarni, K. L. Adelberger (CIT), and Frail further write: "Spectra of Bond's variable were obtained using the Keck II 10-m telescope (+ LRIS) on May 11.25 UT. The object has no obvious emission lines. We have identified a set of aborption features between 430 and 514 nm that we associate with the Fe II triplet near 237.5 nm, Fe II at 258.6 and 260.2 nm, and Mg II at 279.6 and 280.3 nm, which places this system at z = 0.835. Several other absorption features are also seen. If the source is associated with GRB 970508, it is evident that the gamma-ray burst lies at z >/= 0.835. Absence of prominent Lyman-alpha forest in the spectrum also suggest that the source is at redshift z < 2.1."

(C) Copyright 1997 CBAT
1997 May 11 (6655) Daniel W. E. Green

Figure 2.6: Extracts from IAU 6655 and 6656 about GRB970508 [1].

redshift and flux we estimate that, if isotropic[1], GRBs radiate between 10^{48} and 10^{55} ergs. The serendipitous discovery of GRBs by VELA military satellites is actually comprehensible: theoretical physicists were simply not ready to cope with such phenomena at the time they were discovered.

Years of researches followed BeppoSAX breakthroughs. GRBs are still mysterious phenomena but huge steps were made towards their comprehension. BATSE, Fermi Space Telescope and SWIFT satellite made possible for in-depth knowledge of the GRB spectra and lightcurves, as outlined in the next section.

2.2 OBSERVATIONAL PROPERTIES OF GRB PROMPT EMISSION

The bibliography about observed properties of GRB prompt emission is rather large and sparse. While the core papers for this work will be referred in text body, the interested reader can refer to [33] for a comprehensive review.

GRBs duration: short and long bursts

TEMPORAL PROPERTIES The duration of a burst is defined by its "T_{90}", defined as the elapsed time between the time at which the 5% and the 95% of the total measured fluence has been detected.
Observed values of T_{90} range from milliseconds to thousands of seconds and follow a log-normal bimodal distribution with separation of components around 2 seconds, as in Figure 2.7.
Short Bursts have T_{90} lesser than 2 seconds. The short burst component's T_{90} distribution peaks at 0.2 - 0.3 seconds.
Long Bursts have T_{90} greater than 2 seconds. They are the most common burst, accounting for almost 70% of total number. The long burst component's T_{90} distribution peaks at 20 - 30 seconds.
Short bursts tend to be "harder" than the long bursts, which means that detected photon's mean energy is larger for short bursts than long bursts.
In Figure 2.8 burst's duration is related to their observed peak energy. Long and short bursts cluster different regions of the plane.

The GRB light-curves are quite irregular but still present notable features. Twelve sample lightcurves from the BATSE catalog are presented in Figure 2.9

GRB light-curves time variability

While some burst has quite smooth lightcurves, temporal variability have been detected down to millisecond range [53]. Hydrodynamic simulations and analytic studies both suggest that observations of GRBs light-curves structure below the millisecond scale could be

---

[1] We will see how and why this seems to not be the case. Emission anisotropy brings back the upper bound to the true amount of energy released during a gamma burst to 10^{52} erg.

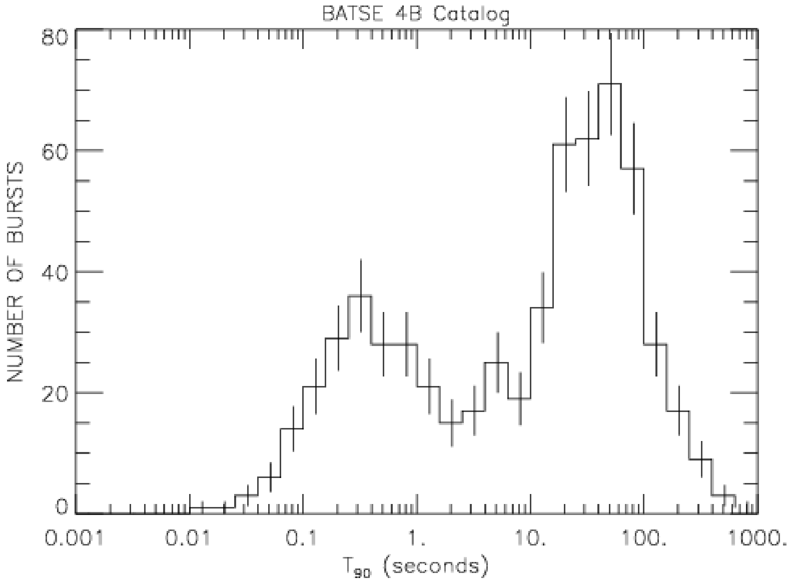

Figure 2.7: Gamma-ray bursts duration are bimodally distributed. Data from BATSE catalog.

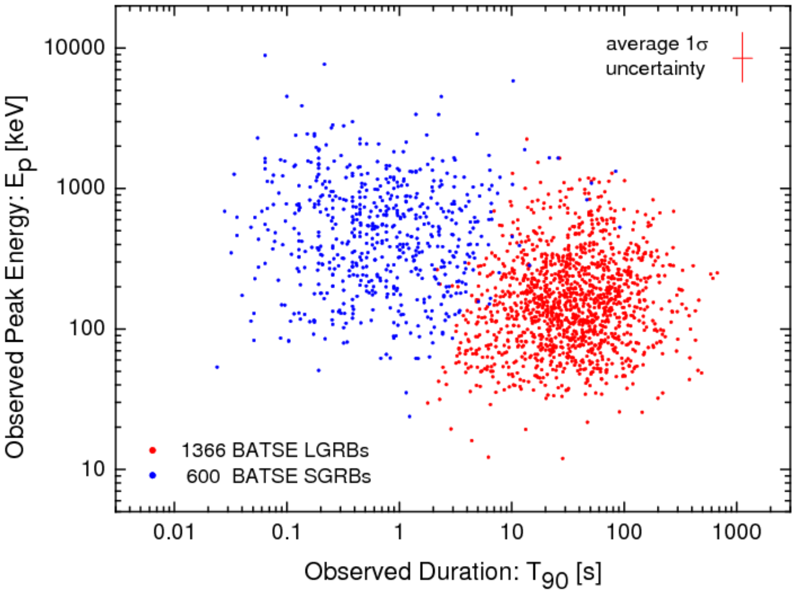

Figure 2.8: Short bursts are "harder" than long bursts. Data from BATSE catalog.

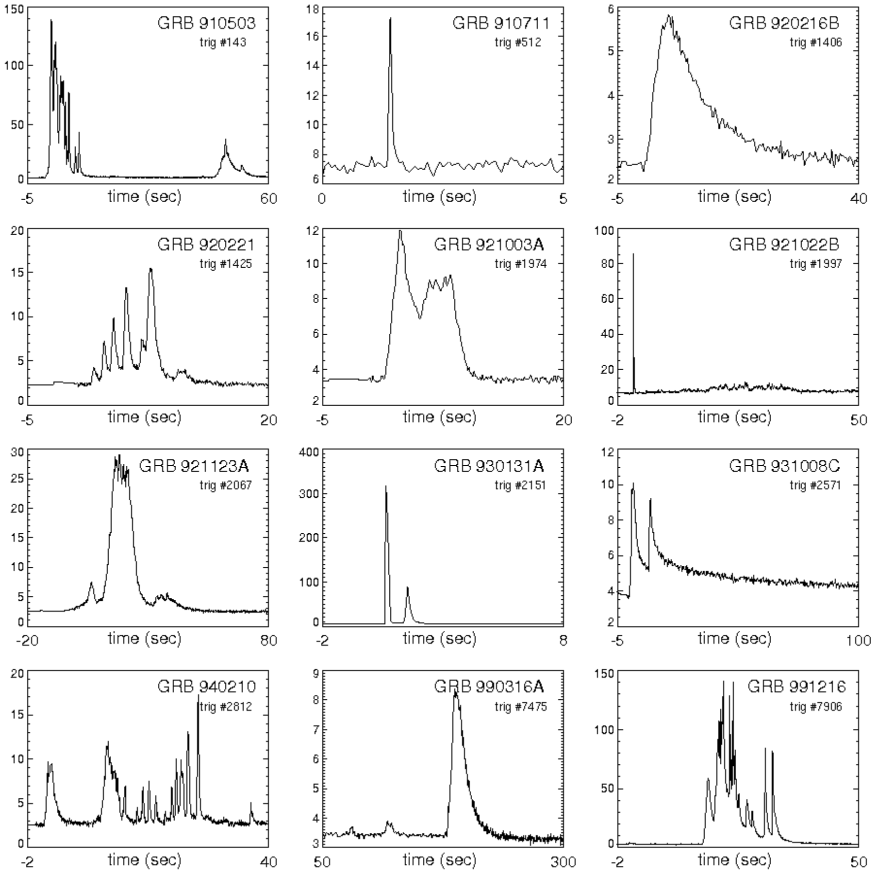

Figure 2.9: GRBs lightcurves samples showing both short and long bursts, events with smooth behaviour and events with high variability. Created with data from the public BATSE archive. Credit: J.T. Bonnell (NASA/GSFC).

related to the source activity. A detailed discussion is proposed in Section 2.5.

Bursts often have distinct emission events separated by quiescent episodes. The distribution of the separation times between emission pulses is log-normal. Power spectrum analyses reveals light-curves show no signs of periodicity.

SPECTRAL PROPERTIES GRB spectra are non-thermal. A typical spectrum fits with a smoothly broken power law known as "Band function" [3]:

Band function

$$N(E) = \begin{cases} A\left(\frac{E}{100\,\mathrm{keV}}\right)^{\alpha}\exp\left(-\frac{E}{E_0}\right), & E < (\alpha-\beta)E_0 \\ A\left(\frac{(\alpha-\beta)E_0}{100\,\mathrm{keV}}\right)^{\alpha-\beta}\exp(\beta-\alpha)\left(-\frac{E}{100\,\mathrm{keV}}\right)^{\beta}, & E \geq (\alpha-\beta)E_0 \end{cases}$$

$N(E)dE$ is the number of photons detected between energies E and $E+dE$, α and β are the photon spectral indices below and above the E_0 break energy. In Figure 2.10, the time-integrated GRB990123 spectrum

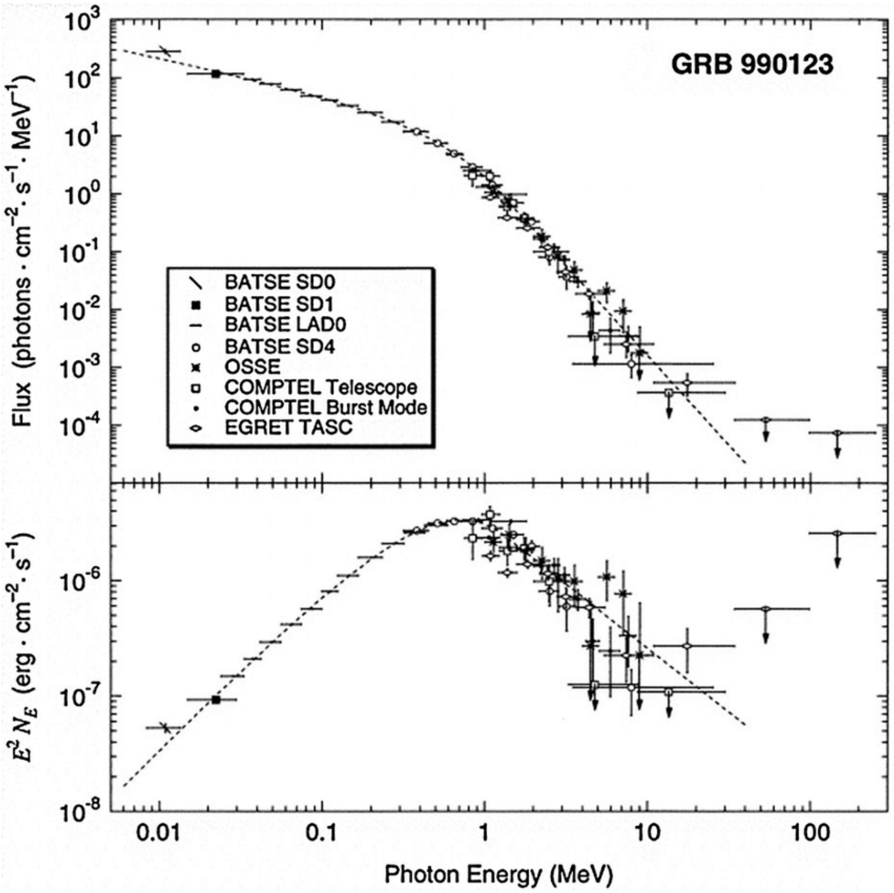

Figure 2.10: GRB990123 is fitted by a Band function. From [7].

is shown to be well fit by Band function over 4 orders of magnitude in energy.

The energy peak The spectral energy distribution $E^2N(E)$ has a peak at E_p, defined by:

$$E_p = (2 + \alpha) \, E_0$$

The peak energy E_p is widely distributed. The bright BATSE sample of GRBs, consisting of 156 bursts, have E_p clustered around 200-300 keV range [44]. However, spacecraft equipped with softer detector like HETE-II, Swift and Fermi all found burst with lower E_p values. All things considered, the E_p distribution seems to form a continuum from tenth of keV to the MeV range [6].

The spectral indices for the bright BATSE sample have a distribution of $\alpha \sim -1 \pm 1$ and $\beta = -2^{+1}_{-2}$.

It should be noted that no particular theoretical model predicts the Band function spectral shape. In the years between 2000 and 2010 the operations of Swift and (especially) Fermi significantly extended the observation spectral window. On the basis of Fermi broad-energy observations, it is speculated that there may be three spectral components shaping the time-resolved GRB spectra:

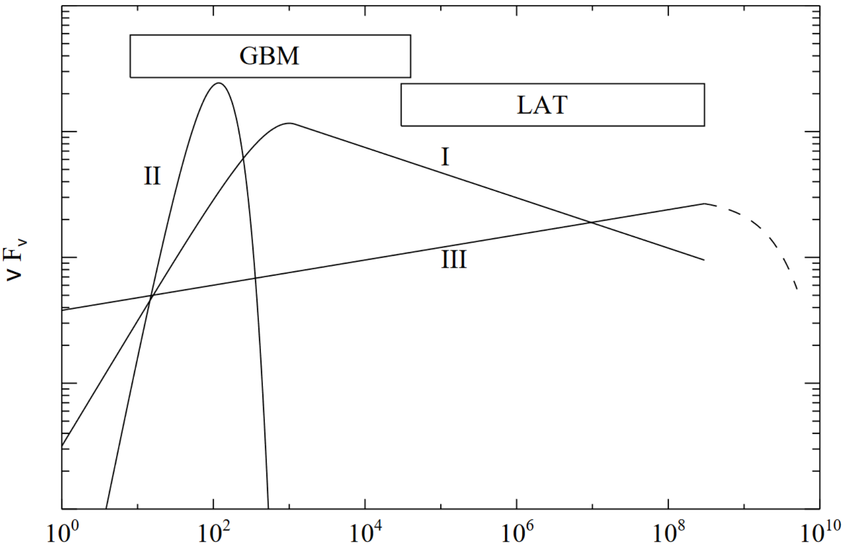

Figure 2.11: The three possible elemental spectrum components that shape the observed time-resolved spectra of GRBs. Some components can be suppressed in some GRBs. From [56].

- A Band function component, non-thermal and extending over a wide energhy range.
- A quasi-thermal component extending to low energy.
- A non-thermal component extending to high energies.

The spectra of different bursts may be decomposed into one or more of these elemental components [56]. The three components are rapresented in Figure 2.11 along the energy range of the GBM and LAT instruments aboard Fermi.

2.3 THE COMPACTNESS PROBLEM

GRB light-curves show millisecond variability [53]. This implies that the source should be an extremely compact object, with linear dimension $R < c\delta t \sim 3000$ km. The energy emitted from an isotropic source at distance D with fluence F:

$$E = 10^{50}\,\mathrm{erg} \cdot \left(\frac{D}{3000\,\mathrm{Mpc}}\right)^2 \cdot \frac{F}{10^{-7}\,\mathrm{erg\ cm^{-2}}}$$

The GRB emission is intense around $E_1 = 100\,\mathrm{keV}$. Photons at energies around $E \sim E_1$ interact with less energetic photons at $E_2 < E_1$ producing a e^+e^- couple if $(E_1E_2)^{1/2} > m_ec^2$. Noting f_p the fraction of electrons satisfying the previous relation, the optical depth of the process $\tau_{\gamma\gamma}$, for a source of linear dimension R:

$$\tau_{\gamma\gamma} = f_p \cdot \frac{\sigma_T}{m_ec^2} \cdot \frac{F\,D^2}{R^2} \propto \frac{E}{R^2} \tag{2.1}$$

where σ_T is the Thomson cross-section, m_e is the mass of the electron and c is the speed of light.
For a typical GRB the expected optical depth resulting from leptonic couple creation process would be $\tau_{\gamma\gamma} \gg 1$. Large optical depth would imply a strongly thermal spectrum and make impossible for energetic photons to reach us.
Taking into account cosmological effects is not of any help here since these could provide corrections in the order of the unity.
What we are facing now is a theoretical challenge, the *compactness problem*: it seems that the estimated source dimensions cannot be conciliated with the observed bursts spectra.

Relativity solves the compactness problem, as long as..

How do photons escape from the source? A solution to the problem comes from special relativity.
We consider now a source of radiation that is moving towards an observer at rest with relativistic velocity characterized by the Lorentz factor:

$$\Gamma = \frac{1}{\sqrt{1-(\frac{v}{c})^2}}$$

The following statements hold true:

- Photons reaching the observer are blueshifted in agreement with: $h\,\nu_{obs} = h\,\nu\Gamma$. Since the energy at the source are reduced by a factor Γ, the observed fraction of photons able to produce lepton pairs $e^-\,e^+$ is smaller by a factor $\Gamma^{-2\alpha}$. Here $\alpha \sim 2$ stands for the high-energy photon spectra index.
- The emitting region $R < \Gamma^2\,c\,\delta t$ is larger than the original estimate by a factor Γ^2.

As a consequence, the optical depth $\tau_{\gamma\gamma}$ in equation 2.1 becomes:

$$\tau_{\gamma\gamma} = 10^{13}\cdot\frac{f_p}{\Gamma^{(4+2\alpha)}}\Big(\frac{F}{10^{-7}\,\mathrm{erg\,cm^2}}\Big)\Big(\frac{D}{3000\,\mathrm{Mpc}}\Big)^2\Big(\frac{\delta t}{10\,\mathrm{msec}}\Big)^{-2} \tag{2.2}$$

where we had substitued $f_p \longrightarrow \frac{f_p}{\Gamma^{4+2\alpha}}$ and $R \longrightarrow \Gamma^2\,c\,\delta t$.
For a tipical GRB, in order for $\tau_{\gamma\gamma}$ to be less than 1, it should happen that $\Gamma \gtrsim 100$.
The compactness problem would not arise if the source emitted the energy in some form with a high Lorentz factor and this energy got converted to the observed gamma-rays at a large distance, where the system is optically thin.

2.4 THE GRB PROMPT EMISSION

Two main models exist in order to explain the γ-ray prompt emission from GRBs. The first, widely used, model considers a "*fireball*" consisting of photons, electron and positron pairs and an amount of baryons. A fireball could be produced in extreme astrophysical events, such as

mergers and collapse of massive stars. The largest part of energy is initially mainly stored in radiation but, as the fireball expands, energy is transferred to the baryons that are in turn kinetically accelated to a high Lorentz factor. A fraction of the initial thermal energy is expected to be radiated away at the photosphere. At larger distances internal shocks tap into the jet kinetic energy in order to accelerate electrons which in turn produce non-thermal γ-rays via the synchrotron and inverse-Compton radiation. The fireball model will be the subject of this section.
The main competitor model suppose the energy outflow to be dominated by Poynting-flux. In this model, the magnetic field energy is dissipated into particle energy via magnetic reconnection. Since its basic mechanisms are still obscure and their description heavily rely on simulations, Poynting-flux model has little predictive capability.

THE BARYONIC FIREBALL MODEL We consider an ouflow with luminosity L and initial radius R_0. According Stefan-Boltzmann law, the initial temperature T_0 is determined by the relation:

$$k_B T_0 \approx k_B \left(\frac{L}{4\pi R_0^2 g_0 \sigma_B} \right)^{1/4} = (1.3\text{MeV}) L_{52}^{1/4} R_{0.7}^{-1/2} \tag{2.3}$$

where k_B and σ_B are respectively the Boltzmann and Stefan-Boltzmann constants, and $g_0 = 2.75$ is half of the effective degrees of freedom for a plasma consisting of photons, electrons and positrons at the thermal equilibrium. At right and in the following we make use of the notation: $X_n \equiv X/10^n$.
We demonstrate that:

> *The Lorentz factor of an adiabatically expanding spherical shell increases proportionally to the distance from the center up until a terminal value Γ_s, for as long as the system is optically thick to Thomson scattering.*

Consider a spherical[2] shell of radius r and width δr in the inner engine inertial frame, adiabatically expanding with a Lorentz factor $\Gamma(r)$.
The fireball dynamics is constrained by conservation of energy flux and entropy.
Luminosity in the inner engine frame does not change as the shell expands:

$$L = 4\pi r^2 g(r) \sigma_B T'^4 \Gamma^2(r) \tag{2.4}$$

---

[2] It is enough to consider a "quasi-spherical" shell such as the spherical-like section of a relativistic jet with semiaperture $\theta \gtrsim \Gamma^{-1}$

Where $T'(r)$ denotes the shell temperature in the comoving inertial frame.
The entropy contained in the shell is:

$$s = 4\pi r^2 \delta r^{'} g(r) T^{'3} \tag{2.5}$$

The entropy is conserved for an adiabatically expanding shell as well as invariant under Lorentz transformation.
The shell width in the comoving frame: $\delta r^{'} = \Gamma \delta r$. Using equation 2.5 and entropy conservation:

$$\frac{T^{'}}{T_0} = \left[\frac{1}{\Gamma} \cdot \left(\frac{R_0}{r}\right)^2 \left(\frac{g_0}{g}\right)\right]^{1/3} \tag{2.6}$$

Substituting now in equation 2.4:

$$\Gamma(r) = \left(\frac{r}{R_0}\right) \left(\frac{g}{g_0}\right)^{1/2} \tag{2.7}$$

The Lorentz factor Γ continues to increase proportionally to r for as long as the system is optically thick to Thomson scattering so that photons and particles are coupled[3].
The terminal Lorentz factor is given by:

$$\Gamma_s = \frac{L}{\dot{M}c^2} \equiv \eta \tag{2.8}$$

where $\dot{M}$ is the baryonic mass flux associated with the outflow. The Lorentz factor terminal value Γ_s is attained at saturation distance $R_s \sim R_0 \Gamma_s$.

You need baryons if you want to cook a fireball

In order for the prompt emission to reach us it is needed for the electron/positron pairs to cease being in thermal equilibrium with the plasma and annihilate, making the fireball transparent to radiation. We will see that this crucial observation comes with a caveat regarding the presence of a baryonic component in the fireball.

> *Pair annihilation/creation freezes when the expanding, cooling shell reaches $T_{freeze} \approx 20.5\,keV$ or $\Gamma_{freeze} \approx 64$. If the baryonic load is zero, the freeze-out radius equals Thomson photospheric radius while $\Gamma_s \longrightarrow \infty$ and so pair annihilation/creation continues for as long as the shell accelerates.*

The cross-section for pair annihilation is

$$\sigma_{e^{\pm} \longrightarrow 2\gamma} = \frac{\sigma_T}{\langle v \rangle / c}.$$

---

[3] i.e. if the photon energy per baryon is much larger than baryon rest energy, $3k_b T^{'} n_\gamma \gg m_B c^2$

Thus, the comoving frame time for a positron to annihilate with an electron is:

$$t'_{e^{\pm}\longrightarrow 2\gamma} = \frac{2}{\sigma_{e^{\pm}\longrightarrow 2\gamma} n' \langle v \rangle} \approx \frac{2}{\sigma_T n' c}. \tag{2.9}$$

The factor 2 in the numerator is due to the fact we are just considering electrons (and not pairs); n′ is the electron-positron pairs number density in comoving frame:

$$n'_{\pm} = \frac{2(2\pi k_B m_e T')^{3/2}}{h^3} exp\left(-\frac{m_e c^2}{k_B T'} \right) \tag{2.10}$$

The process of pair annihilation/creation freezes when $t'_{e^{\pm}\longrightarrow 2\gamma}$ approximates the dynamical time $\sim r/c\Gamma(r)$, which happens at $T'_{freeze} \approx 20.5\,\mathrm{kev}$. It is immediately evident from the above equations that when baryon loading is negligible the freeze-out radius equals the Thomson-photospheric radius. If the freeze-out occurs while the jet is accelerating, then $\Gamma(r)/r \sim 1/R_0$ and, from equation 2.9, we have:

$$\sigma_T n'_{\pm} R_0 \sim 2.$$

Making use of equation 2.10 we obtain the following equation for the freeze-out temperature:

$$T'^{3/2} e^{-\frac{5.9\times 10^9}{T'} \approx 62 R_{0,7}^{-1}}.$$

The solution of which is $T'_{freeze} \approx 20.5\,\mathrm{keV}$. The Lorentz factor at the freeze-out:

$$\Gamma_{freeze} \sim \frac{T(R_0)}{T'_{freeze}} \tag{2.11}$$

Considering that when freeze-out take place the fireball is dominated by photons and $g = 1$, we can estimate the freeze-out radius:

$$R_{freeze} \sim R_0 \Gamma_{freeze} (g_0/g)^{1/2} \sim 1.7 R_0 \Gamma_{freeze}. \tag{2.12}$$

We now consider the effect of a baryonic component on the fireball dynamics and demonstrate that:

> *The presence of minimal baryon loading makes possible for the fireball to continue to accelerate after the pair annihilation/creation freeze-out, up until the Lorentz factor reaches its terminal value or the outflow breaks over the Thomson photospheric radius.*

The number density of electrons associated with protons is:

$$n'_p = \frac{\dot{M}}{4\pi r^2 m_p c \Gamma} = \frac{L}{4\pi r^2 m_p c^3 \eta \Gamma} \tag{2.13}$$

The number density of electrons associated with protons at the freeze-out is:

$$n'_p = \frac{L}{4\pi R_0^2 m_p c^3 \eta \Gamma_{freeze}} \tag{2.14}$$

If fireball dynamics after freeze-out is dominated by electrons associated with protons we have that:

$$n'_p(R_{freeze}) > n'_{\pm}(R_{freeze}) \sim \frac{2}{\sigma_T R_0}.$$

Using the precedent equation as well as equations 2.14, 2.13 and 2.3 we obtain that whenever the condition

$$\eta = \frac{L}{\dot{M}c^2} < \frac{L\sigma_T}{8\pi R_0 m_p c^3 \Gamma^3_{freeze}} \sim 2 \times 10^6 L_5^{1/4} 2R_{0,7}^{1/2} \tag{2.15}$$

is satisfied, the jet continues to accelerate for $r > R_{freeze}$ until $\Gamma \sim \eta$ or the outflow reaches the Thomson photospheric radius. It is evident that in order for condition 2.15 to be satisfied a certain baryonic outflow $\dot{M}$ is needed. This minimal amount of baryons is found to be very low, $\sim 10^{-7} - 10^{-5}\,\mathrm{M}_{\odot}$. For this reason, it is reasonible to expect the condition 2.15 to hold true for most GRBs.

INTERNAL SHOCK SCENARIO The last ingredient needed to sort out GRB prompt emission is some kind of mechanism able to convert the kinetic energy transported in large part by the jet baryons into the gamma-rays we observe at distance.

The most well accepted answer is known as *internal-shock* scenario.

Consider a relativistic, baryonic outflow regulated by a time-dependent Lorentz factor. The fastest shells composing the outflow catch up the slower ones, moving ahead of them. Collisions between relativistic shells transform the kinetic energy, in largest part transported by baryons, into thermal energy, thermal energy that is in turn radiated away, in largest part by electrons, via synchrotron radiation in presence of a magnetic field.

From a thermodynamic point of view we may rephrase as follows:

Collisions make possible to pass from an ordered relativistic bulk motion to an highly disordered state. Relativistic electrons in stochastic motion are then able to irradiate via synchrotron emission in presence of an external magnetic field.

A rather schematic view on the fireball-internal shock model is given in Figure 2.12.

For the purpose of this thesis it will suffice to say that the *afterglow emission* is similarly expected to be the result of collision between fireball shells and the external medium surrounding the source.

ISSUES WITH THE FIREBALL-INTERNAL SHOCK MODEL OF GRB PROMPT EMISSION The fireball-internal shock model for GRB

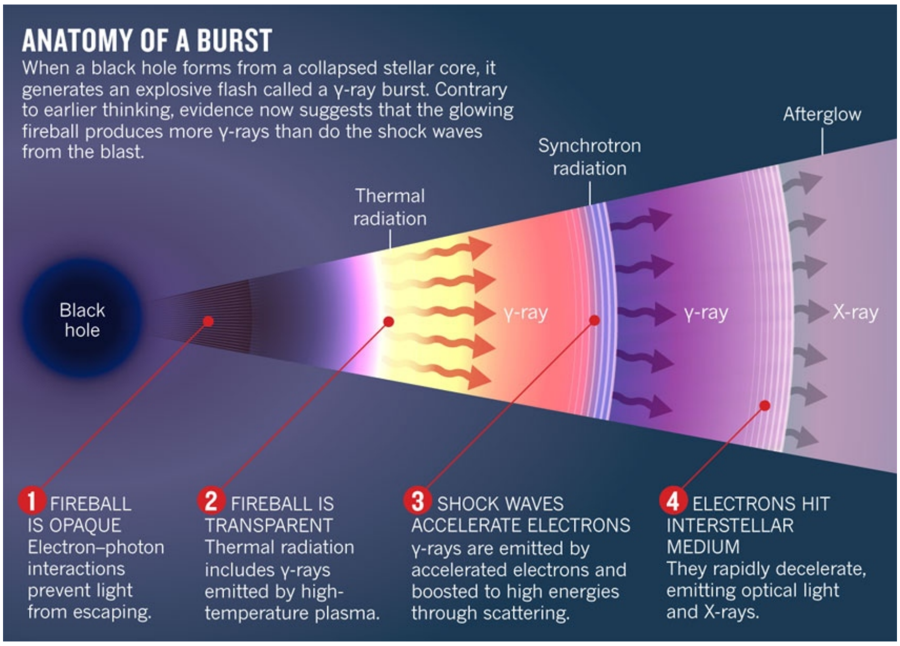

ANATOMY OF A BURST

When a black hole forms from a collapsed stellar core, it generates an explosive flash called a γ-ray burst. Contrary to earlier thinking, evidence now suggests that the glowing fireball produces more γ-rays than do the shock waves from the blast.

1 FIREBALL IS OPAQUE
Electron–photon interactions prevent light from escaping.

2 FIREBALL IS TRANSPARENT
Thermal radiation includes γ-rays emitted by high-temperature plasma.

3 SHOCK WAVES ACCELERATE ELECTRONS
γ-rays are emitted by accelerated electrons and boosted to high energies through scattering.

4 ELECTRONS HIT INTERSTELLAR MEDIUM
They rapidly decelerate, emitting optical light and X-rays.

Figure 2.12: Fireball-shock models predicts the GRB prompt and afterglow emissions. Source: NASA Goddard Space Flight Center.

prompt radiation is not flawless. It does in fact suffer from two major problems:

- The GRB prompt emission spectra do not agree with synchrotron emission at low energies.
- Internal shocks are highly inefficient at converting energy [35]. On other hand, the external shocks powering afterglow emission are expected to be efficient. This asimmetry does not reflect in the measured emitted energy of afterglow and prompt radiation, which is similar.

Synchrotron emission in fast-cooling regime

As briefly discussed in the previous paragraphs the most popular emission models interpret GRB prompt emission as synchrotron emission by relativistic electrons embedded in an intense magnetic field. The synchrotron model is also the most natural option, since its basic ingredients - namely accelerated electrons and intense magnetic field - are provided by the internal shock scenario, in which strong shocks determined by collisions between relativistic shells emitted by the inner engine accelerate particles to relativistic velocities and compress and amplify magnetic fields.

Unfortunately, the synchrotron model does not come without its own problems. Shock-accelerated electrons are expected to have the following energy distribution:

$$\frac{dN_e}{d\gamma} \propto \begin{cases} \gamma^{-p}, & \text{if } \gamma \geq \gamma_m \\ 0, & \text{if } \gamma < \gamma_m \end{cases} \tag{2.16}$$

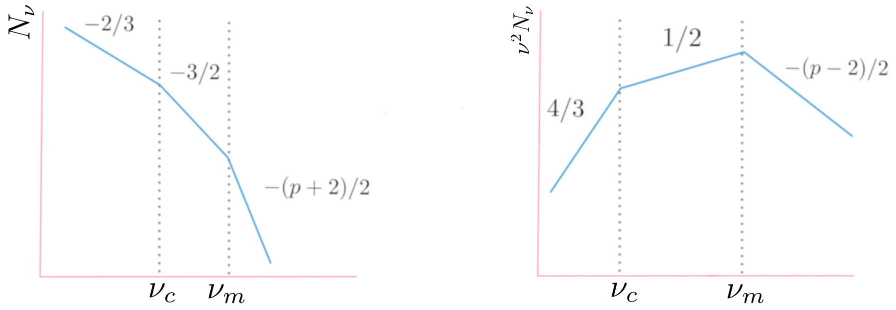

Figure 2.13: Number of photon vs photon frequency and spectral energy distribution of synchrotron emission in fast-cooling regime. Readapted from [17].

The fast-cooling synchrotron photon flux N_ν is:

$$N_\nu = N_{\nu,max} \begin{cases} (\nu/\nu_c)^{-2/3}, & \text{if } \nu_c > \nu \\ (\nu/\nu_c)^{-3/2}, & \text{if } \nu_c > \nu > \nu_m \\ (\nu_m/\nu_c)^{-3/2}(\nu/\nu_m)^{-(p+2)/2}, & \text{if } \nu > \nu_m \end{cases} \tag{2.17}$$

where $N_{\nu,max}$ is the peak flux, ν_c is the cooling frequency, ν_m is the characteristic synchrotron frequency and $p \sim 2.5$ is the power index characterizing the electrons energy distribution.

The synchrotron characteristic frequency ν_m is related to the minimum Lorentz Factor (cf. Section 2.2) by the approximate relation $\nu_m \propto \gamma_m^2 B\Gamma$. The cooling frequency ν_c is the frequency associated to γ_c defined as the Lorentz factor of relativistic electrons that after the cooling time $t_c \propto \gamma^{-1}B^{-2}$, comparable to the dynamical time $t_{dyn} \sim \frac{R}{\Gamma^2 c}$, have radiated most of their energy by synchrotron emission. In Figure 2.13 the photon flux and the spectral emission distribution $\nu^2 N_\nu$ are rapresented along with the power indices.

Although still lacking in the low energy ($< 10-20$ keV) part of the spectrum, prompt emission spectral data suggest the photon index α before the peak to be distributed around a typical value $\langle\alpha\rangle \sim -1$ higher than the value expected in case of fast-cooling synchrotron radiation, $\alpha \sim -3/2$ [42].

The problem has been widely discussed. The largest part of proposed solutions fall into two classes: 1. models that refuse synchrotron and invoke alternative emission mechanisms in order to explain the observed prompt spectra; 2. models proposing 'adjustments' to the basic fast-cooling synchrotron scenario.

Fact is that both approaches come with their own load of theoretical problems. As a result, to date there is still no consensus on the origin of prompt emission.

Recent interesting developements come from the work of Oganesyan, Nava and others [42]. From analyses of 14 GRBs for which Swift XRT data were available during the prompt emission phase it emerged that

for 67% of the sample the usual Band function model fails reproducing the 0.5 - 1000 keV spectra. Infact low-energy data suggest the presence of a spectral break around a few keV, compatibly with the theoretical expectations from synchrotron radiation in fast cooling regime, where a break is expected at the cooling energy $E_c = h\nu_c < E_p$.
Similar analyses have been extended to larger samples, leading to very close results [43].
The XRT aboard Swift is the only instrument online at moment capable of a detailed description of the low energy prompt spectra. However XRT is a narrow-field instrument that needs to be timely slewed to source to gather data. Considering the brief duration of GRB prompt emissions this is not feasible in the vast majority of cases.
We deduce that the activity of a new instrument capable of a detailed and timely characterization of the low energy prompt spectra could result in an improved theoretical comprehension of GRB emission mechanisms.

Tentative evidences of fast-cooling synchrotron emission's blueprint

GRB prompt emission models built around the internal shocks scenario have a problem with efficiency. In collisions, efficiency depends on the relative kinetic energy available to be dissipated. When dealing with the internal shock scenario we confront a number of shells accelerated to similar Lorentz factors. As a result only a few percent of the total kinetic energy is available to be transferred to the fireball particles to be irradiated. Moreover, since the synchrotron power is $\propto m^{-2}$, protons are terrible synchrotron emitters and of this relatively small amount of energy only the fraction available to the electrons will be radiated. Quantitatively, the expected efficiency of internal shocks is attested around 5%.
On the other hand, when the relativistic merged shell impacts on the external medium surrounding the source a large fraction of the total kinetic energy can be dissipated. This actually means that external shocks, responsible of the afterglow emission, are expected to be highly efficient. However observations fail to show the expected difference between prompt emission and afterglow total energy: the observed emitted prompt energy is often comparable, or even greater, than the afterglow emitted energy.
Proposed solutions to the efficiency problem traditionally exploit a distribution of Lorentz factor among different shells in order to make possible for internal collisions to happen with very high Γ-contrasts.
Again, these solutions are not flawless. In this scenario very fast shells move in the photon field created by the previous collisions. Photons getting scattered result in 1. slowing down of the fast shells ultimately leading again to internal collision with small Γ-contrasts; 2. high energy ($\sim$ TeV - GeV) inverse-Compton emission which have still to be clearly identified.

2.5 LIGHT-CURVES VARIABILITY: CLUES ON THE INNER ENGINE

The fireball model supposes the existence of an 'inner engine' able to accelerate a barionic wind into highly relativistic motion. The nature of the 'inner engine' is to this day still mysterious. After all it could not be otherwise: the fireball model implies a thick photosphere preventing direct observation of the inner engine to happen. When looking at gamma-ray bursts astronomers are left in the frustating situation where they can see the most powerful accelerators of the universe at work while not being able to take a glance at the engine compartment.

Numerical simulations of internal shocks suggested that the observed variability could track the activity of the emitting source [30]. If this was the case, GRB light-curves could be providing us an useful timetable of the processes having place in the inner engine.

In a 2002 paper [40], Nakar and Piran purposed a simple analytical model in order to clarify the relations between the observed light-curve variability and the inner engine's activity.

In the internal shock scenario we assume two shells of matter with widths l_1 and l_2 to be ejected while separated by L at times

$$t_2 \sim t_1 + (l_1 + L) \tag{2.18}$$

with Lorentz's coefficient $\Gamma_1 = \Gamma$ and $\Gamma_2 = a \cdot \Gamma$. In the previous relation and in the following, c is supposed to be normalized to the unity.

We also suppose the second shell to be faster than the first so that $a \gtrsim 2$. The second shell will impact on the first at :

$$R_s \sim \Gamma^2(2a^2/(a^2-1)) \sim 2\Gamma^2 L \tag{2.19}$$

The photons emitted during the collision will reach the observer at:

$$t_{obs} \sim t_1 + l_1 + \frac{R_s}{2\Gamma^2} \sim t_1 + l_1 + L$$

GRB light-curves time variability tracks the activity of the inner engine

Substituting L from equation 2.18, we observe that:

$$t_{obs} \sim t_2$$

The photons from the collision will be observed almost simultaneously with an hypothetical photon emitted from the 'inner engine' with the faster shell.

Moreover, since the width of observed pulse can be estimated considering that beaming photon moving towards the observer will arrive before photons moving at an angle $\theta \sim 1/\Gamma$, we have that $\Delta t \sim R_s/2c\Gamma^2 \sim L/c$. Substituting 2.19 in the last equation:

$$R_s \sim 2\Gamma^2 c\Delta t$$

Fast variability gives a scale of the distance R_c between inner engine and emitting region, where collisions take place. Considering $\Gamma \sim 100$ and $\Delta t \sim 1\,\mathrm{ms}$, we get a distance in the order of half an astronomical unit.

Distance of the emitting region from the inner engine can be estimated from the minimum light-curve time variability

The GRB variability window below a few milliseconds is, to date, still little explored.
The main constraining factors limiting our ability to detect fast variability in GRBs are: 1. the timing accuracy of detectors, 2. the detector area. As for the latter, since photon count in the energy band between 50 and 300 keV for a typical GRB is $\sim 10\,\mathrm{phs}^{-1}\mathrm{cm}^2$, in order to provide 1 count every 10 μs a large collecting area of $\sim 1\,\mathrm{m}^2$ is needed.
Still there is strong evidence for millisecond structure to be a rather common bursts feature.
Power density spectrum analyses of a few hundreds joint Fermi and BeppoSAX GRBs sample, using temporal resolution down to 0.5 ms, did find signal up to 10 Hz, suggesting average intrinsic variability time-scale $\lesssim$ 0.1 s below which the temporal power changes regime [16]. Walker et al. analyzed a sample of 20 GRBs from the BATSE catalog, showing that flickering on timescales from 256 μs to 33 μs was common to all the bursts and that millisecond variability is a common feature in classical bursts [53]. Similar studies have been performed on the Fermi GRB catalog. These studies, while reporting somewhat longer minimum variability time-scales, also conclude that variability of the order of a few ms is not an uncommon GRB feature.

Variability on scale of ms and below is still little explored.

2.6 GAMMA-RAY BURSTS PROGENITORS

The fireball model explains reasonably well the physics of gamma bursts. However, it does not answers the most interesting question from an astrophysical point of view: which astronomical objects produce GRBs?
In order to answer this question it will be useful to keep in mind some remarkable feature of GRB emission.

- We estimate an enormous amount of energy to be released during a GRB. Since we estimate energy release up to $\sim 10^{51}$ ergs, the inner engine must be able to accelerate $\sim 10^{-5}$ solar masses to relativistic velocities.
- GRB emission is tipically collimated within small opening angles. The inner engine should then be capable to collimate a relativistic flow of energy and matter.
- GRBs show variability down to the millisecond while typically lasting from a fraction of second to tenth of seconds. This indicates two different time scales characterize the inner engine

and its processes. The millisecond scale suggests the progenitors to be compact objects. The prompt emission duration seems to design some sort of prolonged activity.

- Depending on their duration, GRBs fall in two main categories: long and short GRBs. Since the burst duration is determined by the processes having place in the inner engine the existence of these two categories may imply the existence of two different classes of inner engine.
- GRB take place roughly once per 3×10^5 years per galaxy, about one part in three thousands the rate of supernovae. It should follow that GRBs progenitors are rare, extreme astronomical objects.

All the clues point to one suspect: black holes. GRBs may arise due to rapid accretion from a massive disk (0.1 solar masses per second) onto a compact object, such as a black hole. A disk of this dimensions can only form simultaneously with the compact accreting object, leading to the conclusion that GRBs accompany the formation of a newborn black hole. The model is supported by the observations of relativistic jets in active galactic nuclei, which again are powered by accretion onto black holes.
Simultaneous generation of a black hole and massive accretion disk can arise from different scenarios such as compact binaries mergers and "failed supernovae" in rapidly rotating, massive stars.
It has been shown that of all the above scenarios, only neutron star-neutron star and neutron star-black hole mergers could produce short bursts, while only collapsar could produce long bursts [41]. Observative evidence about the former case came from the simultaneous detection of short GRB and gravitational signal with neutron stars mergers "signature" during 17 August 2017, as discussed throughly in the first chapter of this thesis.
In these models the basic idea is straightforward: the duration of the accretion episode depends on the size of the disk. Since mergers could produce only "small" disks, short bursts must originate from such systems. Naively long bursts will of course be expected from large disks. However, since large disks accretion is inherently inefficient this seems not be the case. Collapsars are expected to produce small accreting disk to continuously feed a central newborn black hole for long (several dozens of seconds) period of time. In this case the efficiency can be large while the duration long.

COLLAPSAR MODEL In collapsar model [54], the GRB progenitor is a rapidly rotating ($\sim 200\ \mathrm{km\,s^{-1}}$ at surface), massive Wolf-Rayet star ($M \gtrsim 30\,M_\odot$). During their lifetime ($\sim 4 - 7 \times 10^6$ yrs), Wolf-Rayet stars lose their external hydrogen envelope through intense stellar

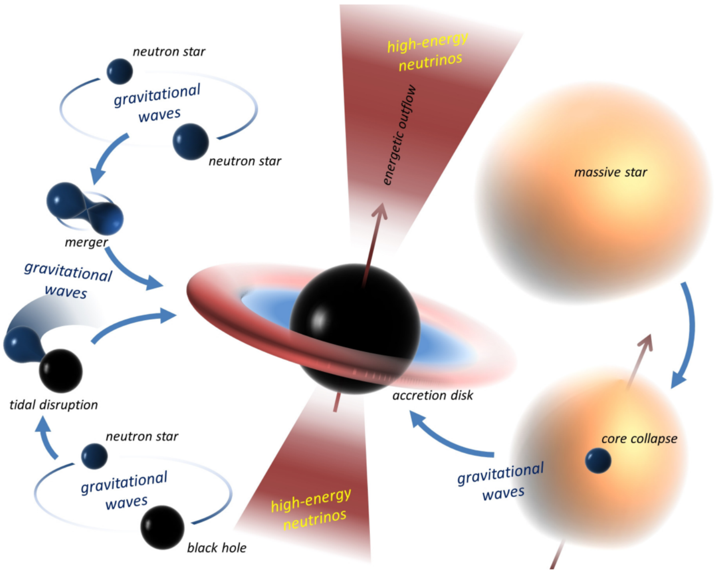

Figure 2.14: Gamma bursts accompany the formation of black holes in binary mergers and collapsing massive rotating stars. I wasn't able to find the original source, for corrections feel free to mail me at dilillo.giuseppe@spes.uniud.it.

winds resulting in an exposed helium core. When the nuclear fuel is exhausted, the ($2\,M_\odot$) iron core collapses into a black hole, either directly or during the accretion phase following core collapse.

An accretion disk of ($\sim 1\ M_\odot$) rapidly forms around the newborn black hole, funneling matter along the rotation axis where angular momentum is low.

The black hole is expected to accrete from the disk over several dozen of seconds. Accretion powers up a long GRB extracting energy via neutrino annihilation [37]. The energy deposited in the surrounding matter will leak out along the rotation axis producing jets with small opening angles , eventually penetrating through the stellar material envelope and producing the GRB.

Relativistic jets are collimated by their passage through the stellar mantle. In particular, it is expected that starting with initial half-apertures up to 20 deg, the jet will emerge with half-angles reduced to ~ 5 deg. In order for the jets to reach the star surface, progenitor stars should have lost their hydrogen envelope. Conversion of internal energy into kinetic energy results in a terminal Lorentz factors along the axis ~ 150. Such a Lorentz factor is compatible with the theoretical needs.

Observational evidences for the collapsar model

Observations hint towards an association of long GRBs with Type-Ic supernovae ([11], [27], and more). It should be noted that the contrary does not hold true: radio survey of supernovae type Ib/c suggests that less than 3% are associated with GRBs ([47]). Long GRBs often occur in brightest region of their host galaxy, suggesting very high

star formation rate at the burst site ([21]) henceforth higher occurrence of massive stars.
Studies have shown long GRBs favor low metallicity environment, being their hosts at lower metallicites than either SNe hosts or general star-forming galaxies [24]. This is consistent with the collapsar model of GRBs, since the star must have low metallicity in order to strip off its hydrogen envelope so that the jets can reach the surface.

MERGERS MODELS Mergers, i.e. neutron star binary mergers or neutron star - black hole binary mergers, can produce a black hole - accretion disk system.
Mergers take place because of the decay of angular momentum due to gravitational radiation emissions. Two degenerate objects will spiral closer and closer together, until in the last few moments, tidal forces rip the neutron star (or stars) apart and an immense amount of energy is liberated before the matter plunges from an accreting disk into a black hole along the rotation axis, similarly to how it happened for collapsars. The entire process is expected to take place over a fraction of seconds, accounting for short GRB duration.
Different simulations ([15], [45]) yield to the mergers resulting in a black hole - accretion disk system, the latter of mass $\sim 0.1\ M_{\odot}$.
Mergers do release $\sim 5 \times 10^{53}$ ergs. Most of this energy will be emitted in neutrinos and gravitational wave, but enough will be produced to power up the burst emission.

Observational evidences for the mergers model

In agreement with the merger models, searches of supernovae associated with short GRB have been carried out without positive detection [4], as expected by merger model.
Short GRBs host galaxies have been analyzed and compared with the hosts of long GRBs and Type Ia supernovae [20]. Results show that most short GRB hosts have exponential disk profiles, characteristic of late-type galaxies, but with a median size twice as large as that of long GRB hosts. More importantly, the observed short GRB projected physical offset distribution has a median about a factor of 5 times larger than long GRBs, which instead did show strong concentration into the brightest, central region of their host galaxy. The observed physical offset distribution matches the predicted value of neutron star binaries: compact stars born in asymmetric supernovae most likely received a "kick", so that the binary system drifted away from the star forming regions when mergers occur.
Kilonovae, weaker than supernovae transient optical/IR emissions, have been predicted to be associated with mergers events. After observational suggestions of a connection between kilonova events and short GRBs, kilonova emission has been observed during the events of 17 August 2017 [52].
The association of signals GW170817 and GRB170817 during the

events of 17 August 2017, provided for the first time direct evidence of a link between mergers and short GRBs.

2.7 WHY HERMES?

Highlights from the first two chapter will now be summarized in a bullet point list.

- No present X-ray astronomy facility will be able to serve as an all-sky GRB monitor with arcmin or better localization capability. This role will be pivotal in the next decade of multi-messenger observations in order to assist follow-up observers with limited field of view in afterglow detection.
- GRB prompt emissions are the brightest sources in the energy band between 50 keV and 300 keV, with typical photon count rate about $\sim 10\,\mathrm{ph\,s^{-1}\,cm^{2}}$.
- The standard model for short GRBs afterglows describes these in term of emission resulting from a decelerating and decollimating relativistic jet powered by a hidden 'inner engine'. GRBs light-curves time variability relate to inner engine activity. Moreover, detection of sub-millisecond time variability could constrain our models on how energy is carried from the inner engine to the jets, whether in form of Poynting flux or as kinetic energy transported by barionic matter. The main constraining factor limiting our ability to detect fast variability in GRBs are: 1. the timing accuracy of detectors, 2. the detector area. As for the latter, in order to provide 1 photon (50 - 300 keV) count every 10 μs a large collecting area of $\sim 1\,\mathrm{m}^2$ is needed.
- The nature of the radiative mechanism is still uncertain. Recent studies suggest the presence of a spectral break at a few keV, where a handful of bursts have been observed. The presence of the spectral break would favour a scenario in which the emission mechanism is synchroton radiation in fast cooling regime.

HERMES is a daring space project.
It will try to attack all the previous points with small financial resource and little developing and implementing time.
A similar task would be unimaginable just a decade ago. However, exploiting the growing reliability of microsatellites and innovative detector technology, as well as clever mission design, this task is today at reach.
How this will be done will be the subject of the next chapter.
We introduce HERMES and its finality with the following statement:

The primary scientific goal of the HERMES (High Energy Rapid Modular Ensemble of Satellites) project is to develop a cheap and scalable network of nanosatellites able to promptly detect, localize and investigate Gamma Ray Bursts (GRB) and other high-energy transients, such as optical counterparts of gravitational waves events.
In particular, HERMES will be able to detect GRBs prompt emission over a broadband energy band ranging from a few keV to MeV, with temporal resolution below the millisecond and arcmin localization accuracy.

Part II

THE HERMES MISSION

3

THE HERMES PROJECT

Gamma-ray bursts originate far beyond our Galaxy and reach us from all directions. For this reason a GRB sky monitor should cover the entire sky. An all-sky monitor orbiting near the Earth naturally should employ more than one unit in order to access the portion of the celestial sphere occluded by Earth for an individual detector.

A network of satellites makes for a very natural GRBs localization experiment design: since light travels at finite speed, the time difference between the arrival of a signal to detectors hosted by different spacecrafts provides an estimate of the angle of the radiation incidence with respect to the satellites position, therefore to the position on the celestial sphere of the burst source.

This method of source localization has been employed effectively since the very beginning of GRB's observation, as discussed in Section 2.1, and will be investigated in-depth from the HERMES perspective in Section 3.1.

Supporting gravitational interferometers and follow-up observations is not the only HERMES goal. HERMES will indeed be capable of doing its own, possibly breakthrough science. The enabling technology in this regard is the coupled SDD-scintillator detector, the design of which will be amongst the topic discussed in Section 3.4 and 3.5.

3.1 LOCALIZING GAMMA-RAY BURSTS

Considering a network of N detectors, separated by an average baseline distance d, the accuray in determining the position of a light source measuring delay in signal arrival time between different units is given by:

$$\sigma \sim c \cdot \frac{\sqrt{\sigma_{cc}^2 + c^{-1} \cdot \sigma_{\vec{r}}^2 + \sigma_t^2 + \sigma_{sys}^2}}{d \cdot \sqrt{N-3}} \tag{3.1}$$

where σ_{cc} is the error on the cross-correlation calculated between two light-curves, σ_t is the uncertainty in absolute time, $\sigma_{\vec{r}}$ is the error on the units location, σ_{sys} is a systematic uncertainty and c is the speed of light. HERMES units will fly in Low Earth Orbit (LEO) where the use of miniaturized spaceborne GPS receivers is possible. GPS will make possible to strongly limit units positioning and absolute time uncertainties, according to $\sigma_t \sim 10\,\text{ns}$ and $c^{-1} \cdot \sigma_{\vec{r}} \sim c^{-1} \cdot 10\text{m} \sim 30\text{ns}$. Considering baseline distances roughly similar to the earth diameter

$d \sim 7000\text{km}$ as well as σ_t and $\sigma_{\vec{r}}$ to be expressed in milliseconds, we can simplify the Equation 3.1 as follows:

$$\sigma \sim 2.4\,\text{deg} \cdot \frac{\sqrt{\sigma_{cc}^2 + \sigma_{sys}^2}}{\sqrt{N-3}} \tag{3.2}$$

σ_{cc} depends on different factors:

1. The temporal resolution of the detector.
2. The temporal structure of the transient.
3. The number of photons per temporal bin in the light-curve, which is in turn determined by the source flux and the collecting area of the detector.
4. The background noise.

For HERMES, it is expected $\sigma_{cc} \sim 10\,\mu$s for bright GRBs with a millisecond structure.

In order to estimate σ_{sys} it is useful to consider the IPN experience. IPN localization capability was constrained by the following factors:

a. The use of different detectors operating on different energy bands, with different aspects.

b. Different orbital position and relatively poor knowledge of the distance between the spacecrafts.

c. Poor time synchronization between the units.

HERMES is designed to minimize the impact of all these factors:

a. Every unit will host the same detector and will be equipped with an Attitude Orbit Control System (AOCS). The employment of an AOCS will make the units able to slew with a few degree of accuracy making it possible for different satellites to see the same event with similar aspect angles.

b. Detector flying in different orbits and orbital positions experience different contributions from the background. The background will be carefully modelled and simulated for each detector along the orbits and then subtracted. The team has a long experience in this kind of data analyses aimed at extracting faint signal much weaker than the background, accumulated in the analyses of BeppoSAX PDS, INTEGRAL IBIS and AGILE data.

c. The usage of GPS receivers strongly limits units positioning and absolute time uncertainties, as discussed above.

This should make it possible for value of σ_{ss} to be reduced down to the range between 10 and 100 μs.

With reference to Section 2.7 we invoke:

> *"No present X-ray astronomy facility will be able to serve as an all-sky GRB monitor with arcmin or better localization capability. This role will be pivotal in the next decade of multi-messenger observations in order to assist follow-up observers with limited field of view in afterglow detection."*

Overestimating the contributes from σ_{sys} and σ_{cc} to 1 ms, Equation 3.2 suggests that with 4 units it will be possible to localize GRBs with uncertainties in the order of a few degrees. Reducing the σ_{sys} and σ_{cc} to $\sim 50\,\mu$s will make possible to localize a GRB with arcmin accuracy with a network composed by 60 units.

3.2 MICROSATELLITES SYSTEM

Dealing with a decentralized system allow for a highly scalable and modular architecture: as a starting point a few units can be employed to gain operational experience to be later used in order to improve the design, therefore reliably enlarging the system to a new scale.

For example, scalability will allow to study in detail the limiting factors on σ_{cc} and σ_{sys} employing just a few units from which subsequent units design can be improved.

The concept is quite elegant. But elegance usually comes at a cost. Networking tens, even hundreds, of units contributes to the complexity of the system. This complexity should usually be payed in terms of financial budget and developing time.

Despite the obvious differences, ESA Galileo makes for a suggestive example. Galileo is the long-awaited european civil global navigation satellite system. It will be composed by 26 units of relatively small spacecrafts ($\sim$ 700kg) in medium Earth orbit plus a complex ground segment. Galileo took more then 20 years in order to be developed and will reach full operational status in 2020. The cost of the total network is quite staggering: 10 billion of euros.

Going back to gamma-ray bursts, we now recall that:

> *"GRB prompt emissions are the brightest sources in the energy band between* 50 *keV and* 300 *keV, with a typical photon count of about* $\sim 10\,ph\,s^{-1}\,cm^{2}$."

The extraordinary GRB brightness makes for extraordinary opportunities: GRB observation is possible on small detectors that in turn can be hosted by miniaturized spacecrafts.

GRBs extraordinary brightness make detection possible even on small detectors.

CubeSat is a nanosatellite standard defined by units of no more then 1.33 kg, often making use of commercial off-the-shelf (COTS) components. Initially developed for educational purposes, and for this reason designed in order for their launch to be affordable for a typical university, CubeSat allows space mission to happen on financial and

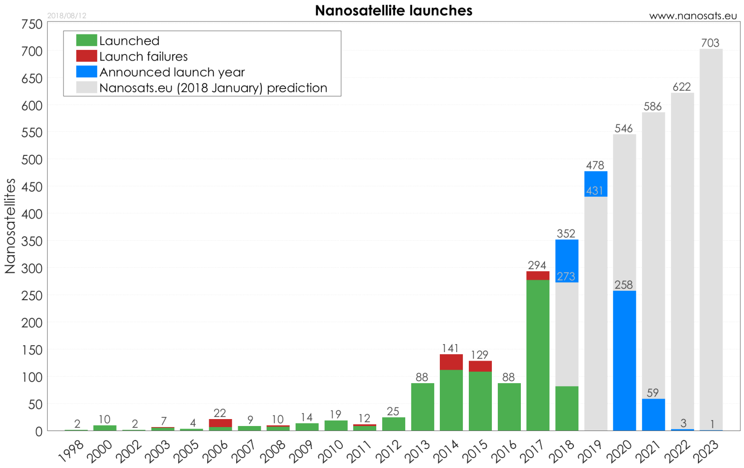

Figure 3.1: Nanosat launches and announced launch per year. Credit: Erik Kulu [32].

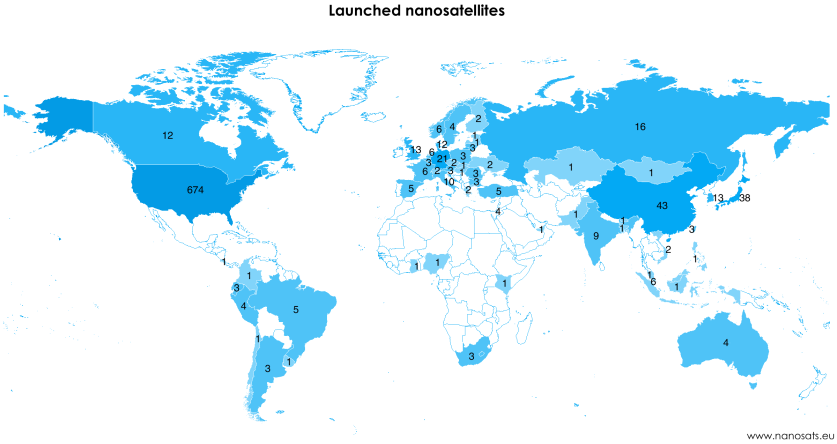

Figure 3.2: Nanosat launches per countries. Access to miniaturized spacecraft is fueling emerging countries space programs [32].

time-scale orders of magnitude below the historical mean value and is gaining momentum for its comercial and scientific application.
In order to attest the growing interest in nanosatellite technology and its reliability, quite a few programs are worth mentioning. "Planet" is a commercial - intended mainly for crop yield prediction - Earht-imaging nanosatellite constellation composed by more that 300 units that attracted the impressive funding of $183 milions. In March 2018 NASA launched the first CubeSat to deep space: Mars Cube One (MarCO). MarCO is a flyby mission consisting of two nanospacecraft, intended to follow and assist NASA InSight Mars lander mission. As for astronomy application, Bright Target Explore (BRITE) is a network of 6 nanosatellites launched between 2013 and 2014 for astrophotometry of the brightest stars in single wavelength band. However, the most interesting scientific missions are still brewing in the laboratories of universities all over the world. University of Melbourne's SkyHopper is expected to be launched in 2021. It wil be the first CubeSat for infrared astronomy. Led by Michele Trenti, one of the top 10 Hubble Space Telescope (HST) user, the SkyHopper team is developing a spacecraft that can rightfully be considered the $36 \times 22 \times 24$ cm nephew of the 11 tonnes iconic HST. Capable of ultra-stable image quality in four simultaneous filter bands and rapid slewing ($1000\times$ faster than HST), it will assist the James Webb Space Telescope as infrared space facility, search for other Earths and study GRBs afterglows at high redshift.

As for HERMES, the Italian Ministry of University and Research (MIUR) and the Italian Space Agency (ASI) funded a first project to study, design, and prototype the detector and the Service Module. The study – HERMES Technology Pathfinder - will result in the deployment of the first three flying units by mid 2020.
Three additional units will be launched in different orbits briefly after, building a minimal network able to run a first GRB localization experiment with good localization capability ($\sim$deg) of relatively bright transient. The six-unit fleet will go under the name of HERMES – Scientific Pathfinder (HERMES - SP) and is expected to be online in just 3 years. At the time of redaction it's recent news that EU granted 3.3 million euros for the development and launch of HERMES - SP in the framework of Horizon 2020 programme for research and innovation. HERMES-SP will be exploited to carry out a Phase A feasibility study for a future HERMES full constellation system (HERMES-FC): a larger CubeSats network composed of tens of units, able to localize weak transient sources with arcmin accuracy.

3.3 THE KEY BEHIND HERMES DESIGN: BROAD ENERGY BAND DETECTION

In Section 2.5 we discussed how having access to GRBs light-curves with high time-resolution could result in a much needed insights about jet composition and inner engine activity.
As stated in Section 2.7:

> *"The standard model for short GRBs afterglows describes these in term of emission resulting from a decelerating and decollimating relativistic jet powered by an hidden 'inner engine'. GRBs light-curves time variability relates to inner engine activity. Moreover, detection of sub-millisecond time variability could constrain our models on how energy is carried from the inner engine to the jets, whether in form of Poynting flux or as kinetic energy transported by barionic matter. The main constraining factor limiting our ability to detect fast variability in GRBs are: 1. the timing accuracy of detectors, 2. the detector area."*

In Section 2.5 we estimated that, in order to provide 1 photon count every 10 μs in a band ranging from 50 to 300 keV a large detector area of about $\sim 1\,\mathrm{m}^2$ is needed.
The effective area of each HERMES detector will be severely constrained by the spacecraft size. Since the detector will occupy one face of the CubeSat unit we can pose an upper bound of $10\,\mathrm{cm}^2$ to the detector's effective area. This implies that, recombining the individual signals, $\sim$ 100 units will be needed in order to achieve the desired time resolution.
Given the restriction on the detectors area, can the number of HERMES units necessary to achieve 10 μs time resolution be reduced? And in particular, can it be reduced by a factor 2, allowing the expected number of units for achieving arcmin source localization and high light-curves time resolution to coincide?

GRBs emit between 50 keV to 300 keV roughly as much they emit from 5 keV to 50 keV

The answer is yes if one realizes that a typical GRB emit roughly the same number of photons in the 50 to 300 keV band as it does emit between 5 and 50 keV.
This observation transforms the technological requirement for 100 spacecrafts into a requirement for a broad energy band, between 5 and 300 keV.
In turn, reliably detecting GRBs photons over a broad energy band make it possible to tackle the problem of GRB radiative mechanism.
Quoting from Section 2.7:

> *"The nature of the radiative mechanism is still uncertain. Recent studies suggest the presence of a spectral break at a few keV, where a handful of bursts have been observed. The presence of the spectral break would favour a scenario in which the emission mechanism is synchroton radiation in fast cooling regime."*

It should be clear by now that covering a broad band of energies is the leading requirement for detector design.

Broad energy band will in fact make possible for HERMES to pursue his own new, possibly breakthrough science while being able to serve the much needed supporting role of all-sky burst monitor, in the "fast and cheap" framework of miniaturized spacecrafts.

Broad-band energy covering allows HERMES to do its own science.

3.4 SCIENTIFIC GOALS AND MISSION REQUIREMENTS

The goals and relative scientific requirements of the HERMES mission can now be summarized as follows:

- Achieving arcmin to arcsec uncertainty on GRB localization of a sizeable ($\gtrsim 10$) number of GRB per year, with a time delay between detection and localization as short as few minutes.
- In order to probe radiation mechanisms and jet composition as well as to investigate inner engine activity, HERMES will sample the temporal structure of GRBs and other energetic transients down to a few μs while covering a broad band of energy ranging from a few kev to ~ 1 MeV.
- Prompt data dissemination, within in a few minutes from localization.

The scientific requirements translate in the following high-level technological requirements:

- Large ($\gtrsim 50$) number of detectors separated by a baseline distance of several thousands km.
- The position of every unit should be known with uncertainty of $\lesssim$ a few m. The absolute time of every unit should be known with uncertainty of $\lesssim 1\,\mu$s.
- Each detector should have a field of view $\gtrsim 2$ steradian.
- The constellation should be able to observe the same point in the sky for the longest possible time during each orbit with a position accuracy of $\sim$ deg. This implies implementation of ACS aboard every HERMES units.
- Individual detectors collecting area of $\gtrsim 50\,\mathrm{cm}^2$ and total collecting area of the order of $\sim 0.5 - 1\,\mathrm{m}^2$.
- The energy range of detectors should cover at least the band between 5 and 300 keV, with an ideal range spanning between 3 and 1 MeV.
- Temporal resolution of detectors $\sim 1\,\mu$s.

- Capability to download full burst information within minutes. This requires the employment of dedicated ground-station networks and/or Globalstar/Iridium uplink.

3.5 HERMES MISSION CONCEPT

PAYLOAD Silicon Drift Detectors (SDDs) are silicon detectors used to detect both hard and soft X-ray photons. SDDs are small and work at low voltage, making them perfectly fit to HERMES miniaturized spacecrafts. At room temperature they offer an extremely low noise level - tens of e^- rms - in the energy band between 1 and 10 keV. However, a typical 500 μm SDD is able to detect photons with good efficiency only up to some tenth of keV. Making use of a new design idea, the same SDD can be used in order to extend the detection band up to to MeV. This will provide unprecedented broad band coverage for observation of energetic cosmic transients in an extremely compact package.

The enabling technology: SDD-scintillator coupled detectors

The concept is simple. The field of view of each detector will be limited to ~ 2 steradians field up to 20 - 30 keV by a passive collimator positioned in front of the detector. The SDD is coupled to a scintillator crystal, where the hard X-ray photons are converted in visible light. In turn, visible photons are converted in electric charges and collected by a photo-detector. This photodetector will be the same SDD used to directly detect soft X-ray photons. Acting as a photodiode, it will produce an amplitude charge signal related to the amount of scintillator light observed. The discrimination between the two signals in the SDD is achieved using a segmented design: a single scintillator crystal will be seen by two different SDDs, so that events detected at only one SDD will be most likely associated with soft X-Rays, while events detected simultaneously in more than one SDD will be associated to the optical light produced in the scintillator by hard X-ray photons.
A *SDD-scintillator coupled detector* lies at the heart of every HERMES units and should be considered as the mission's enabling technology. A schematic view of an HERMES modular detector unit is presented in Figure 3.3.

The scintillator crystal selected for HERMES is Gadolinium Aluminium Gallium Garnet (GAGG). GAGG has the quite high of 6.63 g/cm^3, it's mechanically robust and not hydroscopic nor radioactive, while being particularly forgiving to handle. These new crystals present a very fast response time $\lesssim \mu$s and provide a high light output per keV ~ 56 photons keV^{-1}. Fast response is needed in order to take a breach into the submillisecond variability domain of GRBs prompt event lightcurves. On other hand, the high light output allows to reach lower energy thresholds with respect to more standard scintillators of similar density. For reference, the light output of bismuth germanium

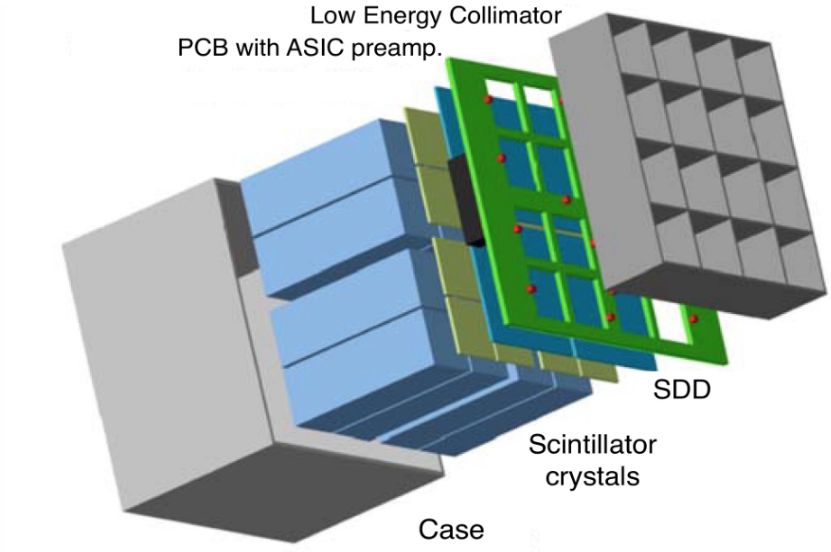

Figure 3.3: Schematic view of the HERMES detector [25].

oxide attests around 8 photons keV^{-1}. Moreover, the scintillator photons wavelength peaks at 520 nm and matches well with the sensitivity peak of SDD. Although certainly promising [55], GAGG crystals have never been used in space so far and need further characterization. A first run of irradiation tests on the detector system will be held by the HERMES team at TIFPA facilities between fall 2019 and winter 2019. These tests are expected to investigate potentially concerning aspects of GAGG crystals such as photoluminescence and will be a first ground for testing various technical implementing solutions (e.g. crystal wrapping, mechanical structure, optical glue etc.).
The SDD technology will be the subject of Section 5.2, to which the reader interested in further details is referred to. SDDs are silicon detectors that allow the decoupling of the area of photon collection - the effective detector area - from the collection area of the produced charge, hence the anode size which determines the noise through its capacitive coupling. Compared to alternative such as silicon photomultipliers (cf. Section 5.2), SDDs are relatively slow in response, as the charge produced by light or by X-rays must 'drift' in the device towards the collecting anode. Reducing SDD size does provide for faster response time and also increases the intensity of the electric field in the depletion volume.
The HERMES SDDs will be designed by the HERMES team, which includes key players in the development of these devices from INAF, Universities of Trieste and Udine and INFN-Trieste, and realised by Fondazione Bruno Kessler (FBK) following a well consolidated activity.

The volume allocated to the payload in each HERMES unit is that allowed by a single CubeSat unit, 1000 cm^3. A system with a collecting area of 55 cm^2 will be hosted in this volume. The detector consists of a mosaic of 120 SDDs with a surface dimension 7.44 × 6.05 mm and thikness 450 μm coupled to 60 scintillator crystals of a dimension 14.5 × 6.94 mm and a thickness of 15.0 mm. The original CAD design of the HERMES detector is purposed in Figure 3.4.

Front-End and Back-End electronics

Low preamplifier capacitance, power consumption, fast response and compactness are the leading features driving the Front-End Electronic (FEE) and Back-End Electronic (BEE) design. These requirements made it necessary to develop an high performance ASIC (Application Specific Integrated Circuits) for the readout of the silicon detector signal. The design employed by HERMES is named LYRA FE/BE and stems from the VEGA ASIC. VEGA is an application specific integrated circuit developed in order to serve as FEE for high time-resolution, large area detector of LOFT (Large Observatory for X-ray Timing), a proposed ESA class-M space mission devoted to investigate X-ray rapid variability in neutron stars, black holes and other compact objects. In order to keep the input capacitance as low as possible, the front-end component, LYRA FE, hosts charge preamplifiers on the same board that houses the SDDs. All the functions of the spectroscopic chain will be carried out on a separated Printed Circuit Board (PCB) and the signal output multiplexed to LYRA BE, the back-end component. At back-end level the analog signals will be converted to digital, identified as low (single SDDs) or high (scintillator, multiple SDDs) energy, time tagged and finally addressed to the Payload Data Handling Unit (PDHU), towards which LYRA BE will serve as interface.
LYRA FE/BE will be discussed in detail in Section 5.2.

Payload Data Handling Unit

The PDHU will be based on a commercial board. It will: 0. manage the house-keeping routine 1. manage the payload operative modes 2. detect a burst 3. build and storage the burst data packets 4. upload data to ground following a priority ladder.
Burst detection requires the operation of a burst search algorithm by PDHU using payload ratemeters. Since the burst signal is strongly energy-dependent, the algorithm will be based on two different ratemeters: one for low energy events (5 - 50 keV) and one for high energy events (30 - 1000 keV). Bursts will be searched over different time scales, ranging from milliseconds to hundreds of seconds.
The detector operative modes and their relation are rapresented Figure 3.5. Standby mode is the default mode. From every mode but 'Standby' the payload can switch in 'Safe mode' if any kind of anomaly occurs, effectively switching off the detector. From 'Safe Mode' the payload will switch to standby when the environment will be back to normal.

SERVICE MODULE HERMES units will be hosted by 3U class CubeSat. A 3U CubeSat offers a volume of 10 × 10 × 30 cm and a total mass $\lesssim$ 6 kg. Small solar panels severely limit the available power

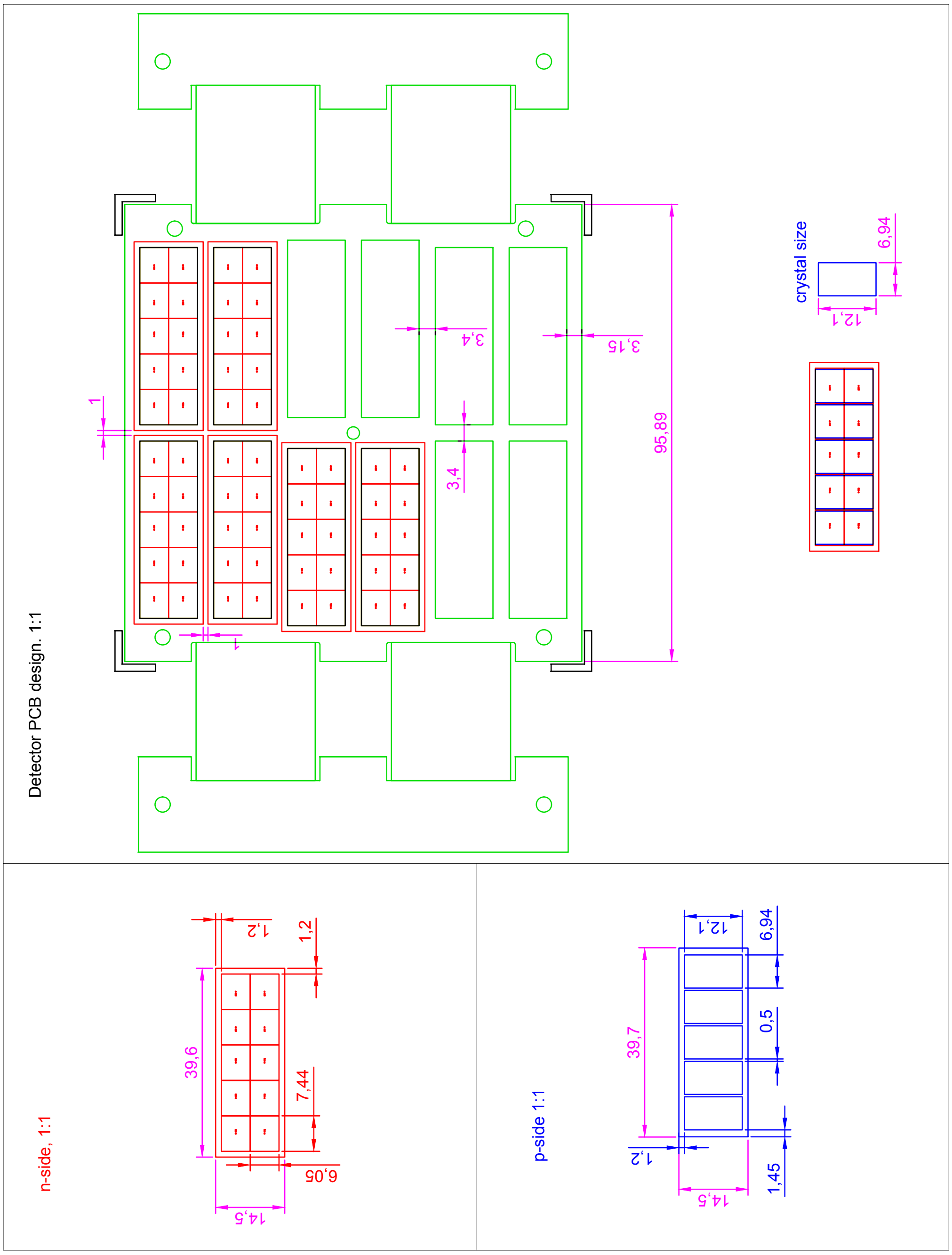

Figure 3.4: Original CAD design of the HERMES detector. Credits: Yuri Evangelisti.

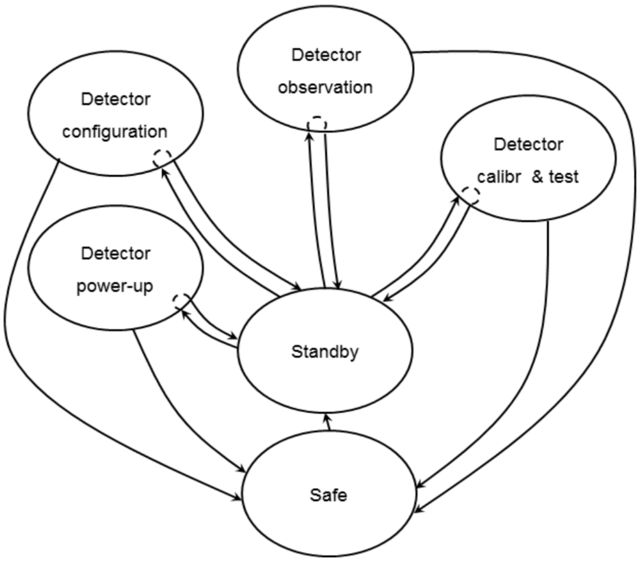

Figure 3.5: Payload modes are managed by the PDHU [25].

supply that is expected to attest at ~ 4 watts. Two-thirds of the total volume and power supply will be allocated to the service module. The limits imposed by small power supply imply the Thermal Control Subsystem (TCS) will be passive. The units will not be capable of orbit control. On other hand we have seen how the ACS is expected to play a key role in transients localization. It will include magneto-torquers and a set of reaction wheels allowing for 3-axis attitude control with tenth degree of accuracy over hours i.e. the LEO orbit time-scale.
Beside compactness and power efficiency, the service module main design driver will be to ensure the space segment basic functionalities at their minimum whenever non-nominal condition occurs. Incidentally we can observe that, although this attention to dangers may sound trivial, in the framework of nanosatellites it really is not. Being able to rely on extremely cheap developement and launch for space industries, nanosatellites are in fact often developed with a "buy-and-fly" approach as demonstrated by the high nanosatellites mortality index. Since miniaturized spacecrafts often go dead because of lack of electronics, the Electric Power (EPS) and Telemetry, Tracking & Command (TTC) Subsystems design will be especially careful. Solar panels will be body-mounted in order to keep complexity low. Batteries will support the power supply during eclipses and when the solar arrays will be not irradiated enough. TTC will focus on a robust data transmission, taking advantage of Globalstar/Iridium module to ensure RF connection whenever a burst might occur. Robust, omnidirectional antennas will be mounted on board and will protect the mission from potential ACS anomalies. The On-Board Data Handling (OBDH) subsystem will make use of software based on the open-source, ESA sponsored, TASTE [50].

4

RADIATION EFFECTS ON HERMES DETECTORS

In this chapter, and in particular in Section 4.6, we will present the first result of our studies: a worst-case scenario estimation of leakage current increase due to trapped proton radiation elaborated for a wide variety of realistic orbits.

Space is n harsh environment. It is populated by massive energetic particles, their flux varying wildly with altitude and geographical coordinates.

Radiation is well-known to pose danger to spacecrafts instrumentation and in particular to silicon detectors. The specifics of how radiation affects intrumentation will be discussed in Section 4.1. As they impact silicon detectors, space particles may change the arrangement of the atoms in the crystal lattice creating lasting structural damage. This in turn creates defect energy levels in semiconductors that can act as trapping and recombination centers. Damage in the bulk of silicon devices crystal structure is known as 'displacement damage' and results in a net increase of leakage current over exposure time. For HERMES detectors this implies a progressive deterioration of spectral resolution.

Since displacement damage depends on particle fluence, prediction of detector performances over time cannot be separated from a careful study of the spacecraft orbit.

As discussed in Section 4.3, HERMES - Technological Pathfinder units will be deployed as piggyback of commercial vectors flights towards a LEO orbit still to be defined. Henceforth, a reasonable prediction study of detector peformance degradation should span a wide region of the orbital parameters space.

4.1 RADIATION DAMAGE MECHANISMS

There are two basic mechanism behind radiation damage: ionization and displacement damage. In the following two paragraphs we will cover more in depth the physics, measurement and effect on solid-state devices, with particular attention on the effects in detectors.

IONIZATION DAMAGE Radiation energy may be absorbed in insulating layers and bulks, liberating unwanted charges through ionization. These charges are free to move through the material causing the onset of stray currents.

Ionization damage is measured in terms of energy absorption per

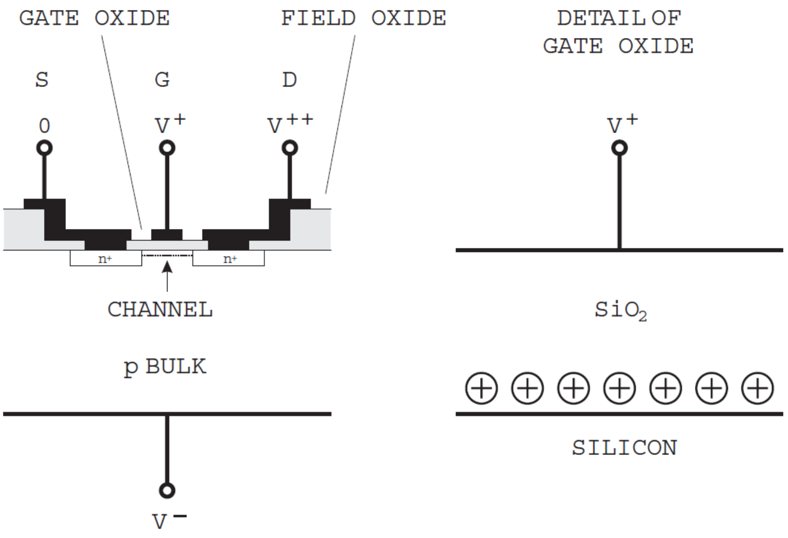

Figure 4.1: A n-type MOSFET transistor is schematically represented on the left. Detail of gate oxide with build-up of unwanted positive charges from ionizing radiation exposure may be found on the right. Image from [48].

Keep your MOSFETs away from ionizing radiation.

volume unit (dose) and commonly expressed in rad or gray (1 rad = 10^{-21} Gy = 1 J kg^{-1}). Ionization damage is dangerous for modern electronics especially because it affects the ubiquitous MOSFET transistors. Electrons freed as a result of ionization are quite mobile and move to the positive electode rather straightforwardly. On other hand, holes moves according to a complex 'hopping' mechanism favouring the chance of trapping in the oxide insulator volume. As a result, the positive charge build-up at the gate oxide interface makes for the gate voltage to be adjusted towards more negative values in order to compensate and henceforth mantain negative charge in the channel region. A graphical representation of the situation is shown in Figure 4.1.

Ionizing radiation is not a problem for most silicon detectors

What about silicon detectors? Charges freed in the bulk of the detector are readily disposed off by the external circuitry. Ionizing radiation is potentially more of a problem for surface structures. Oxide layers are essential in order to control leakage paths and mantain interelectrode isolation in segmented detectors. Since accumulated charges can lead to high local electrons densities and form unwanted conductive changes between electrons. However, in order to prevent signal leakage, it is sufficient for the insulating separator to be characterized by large impedances compared to the input impedance of the amplifier. Since typical impedances for these insulating layers are in the order of 10^2-10^3 ohms, accumulated charges are of concern only for the rare ohmic detectors, HERMES's SDDs are designed to work with very low sensor-preamplifier impedances, in the order of the pF. The ionization

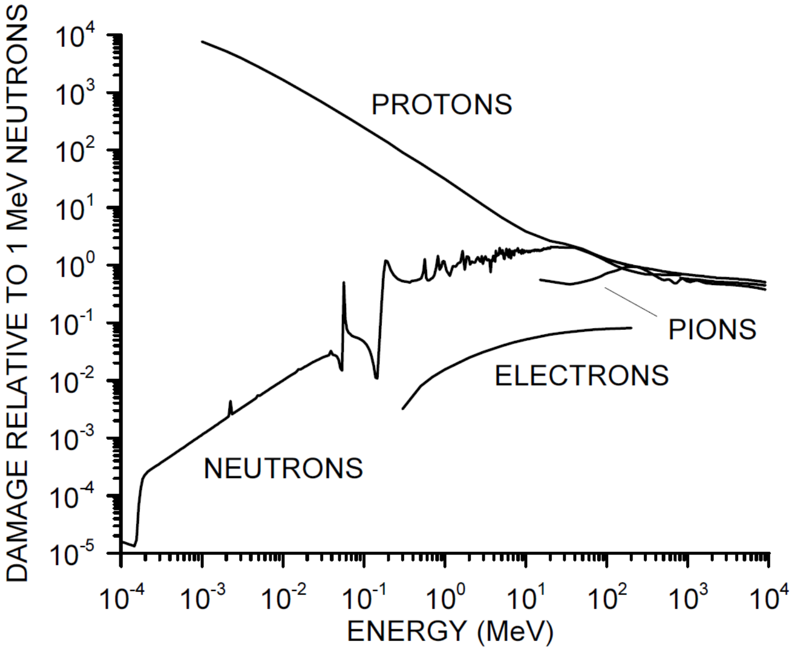

Figure 4.2: Comparison of displacement damage from photons, neutrons, protons, pions and electrons of varying energy relative to the damage of 1 MeV neutrons. Image from [48].

damage occurring from radiation exposure is therefore negligible as far as the HERMES sensor is concerned.

DISPLACEMENT DAMAGE Inciding on silicon, radiation can displace the atoms from their sites in the silicon lattice. This in turn causes the occurrence of defect states with energies between that of the valence and conduction band. These states alter the electrical properties of the semi-conductor.

Depending on the nature of the incident radiation, in particular on the particle species and energy, displacement damage is not as readily measurable as ionization damage. However, studies have shown that it is possible to correlate the damage effects in a device due to a given particle and energy to the effects of possibly different particles at different energies i.e. the damage is linearly dependent on the Non-Ionizing Energy Loss (NIEL), regardless of the particle type [14]. This concept is referred to as NIEL scaling. Accepting NIEL scaling as an hypothesis allows to predict the detector's performance degradation from exposure to complex space emissions, once the response to a simpler test radiation has been determined. A comparison between displacement damage effects from photons, protons, neutrons, pions and electrons relatively 1 MeV neutrons is shown in Figure 4.2.

The NIEL scaling hypothesis

As a side-note about NIEL scaling hypothesis: details of defect cluster formation play a role in evaluating displacement damage from radiation exposure. For example 24 GeV protons form a mixture of

clustered and distribuited damage sites that can lead to significant differences between neutron and lower energy protons damage effects, in particular semi-conductor devices, such as GaAs ones [12]. Even for silicon, NIEL scaling hypothesis should be handled carefully: studies have shown that 'at the microscopic level there is, indeed, no obvious reason for an exact NIEL scaling' and 'even a significant violation of NIEL scaling can still be consistent with experimental data'.
For this reason, accurate detector reference testing for displacement damage should always employ particles and energies well-representative of their radiation environment.

Massive, energetic particles will make your silicon a gruyere

Particles or photons able to transfer 25 eV to a silicon atom can displace it from the crystal lattice. At higher energies, the interaction with energetic particles creates defects clusters in the crystal lattice. In order to quickly quantify the effects of such interaction we will now consider a single 1 MeV neutron. Making the usual simplification, we imagine our neutron transfering about 250 keV to a Si atom through head-on elastic scattering. Recoiling, the displaced Si atom will unbound roughly 1000 other atoms in the lattice. Since bonding distance in diamond-structured silicon crystal is around $2.35 \cdot 10^{-10}$ m, we can imagine the resulting defect region in the lattice extends for about $0.1\,\mu$m. *Annealing*, a process in which thermal motion 'corrects' the lattice structure, may help to some degree, even spontaneously. Still, the damage done can safely be considered permanent, in contrast to what happens with bulk ionization damage.
Since we will deal with high energy astronomy it is importart to note that momentum conservation sets an high energy threshold at 250 keV for direct displacement damage to happen through interaction with photons. At lower energies photons can still indirectly damage silicon lattice through Compton electrons emission but, as appears from Figure 4.2, they are far less dangerous then more massive particles, such as neutrons and protons.

Displacement damage compromises silicon detector performance over time

What do defect regions mean for silicon electrical properties?
When enough defected regions have been formed, carrier lifetime and collection efficiency decrease. As a consequence, the energy resolution of the detector is degraded due to fluctuations in the amount of charge lost.
From an energetic point of view it is possible to understand what happens as a result of the formation of defect regions in terms of *mid-gap states*. To use an evocative analogy, mid-gap states provide 'stepping stones for electron capture and emission processes'
For forward-bias *pn* junction this implies a more frequent recombination and charge loss in depletion region, since the conduction band will be crowded by charges. For reverse-bias junction, such as those in photodiode or radiation detectors, electron emission will dominate, causing a growth of reverse-bias current i.e. leakage current and henceforth electronic shot noise. Furthermore the decrease in carrier lifetime

due to trapping incurs in a loss of signal as carriers recombine while traversing the depletion region.
An example of spectroscopic performance degradation in germanium-lithium detectors due to the displacement damage following energetic neutron irradiation is illustrated in Figure 4.3.

4.2 RADIATION DAMAGE IN SILICON DETECTORS

Reverse-bias junctions are the basic components in many complex devices. In particular, reverse-biased diodes with large - typically hundreds of microns - depletion depths are used as components in photodiodes and radiation detectors, including HERMES's SDDs.
Henceforth, considering ionizing radiation mostly affects surfaces, radiation damage is the damaging mechanism of main concern when it comes to detectors.
As discussed in the previous section, displacement damage causes increasing leakage current in reverse-bias diodes.

The increment of leakage current due to displacement damage ΔI in a detector of volume V, irradiated by Φ_{eq} particle fluence, rescaled to the equivalent effect of 1 MeV neutrons, is determined by the following relation:

$$\Delta I = \alpha \Phi_{eq} V \tag{4.1}$$

The constant α is the "current-related damage rate". In the following we will adopt the value measured at -50°C by Segneri et al. [46] specifically for space application, $\alpha = (11.1 \pm 0.2) \times 10^{-17}\ \mathrm{A\,cm^{-1}}$.
Leakage current does depend on temperature. For this reason, the Equation 4.1 is conventionally normalized at 20°C through the relation:

$$\frac{I(T_1)}{I(T_2)} = \left(\frac{I(T_1)}{I(T_2)}\right)^2 exp\left[-\frac{E_g}{2k_B}\left(\frac{1}{T_1} - \frac{1}{T_2}\right)\right] \tag{4.2}$$

where $I(T_1)$ and $I(T_2)$ are leakage currents measured at the temperatures T_1 and T_2, $E_g \sim 1.11$ eV is the energy gap in silicon and k_B the Boltzmann constant. Leakage current roughly halves every 7°C.
In Section 4.1 we discussed how predictions about displacement damage in a detector are made possible by assuming NIEL scaling hypothesis validity. Is it then possible to relate the fluence of particle p at energy E to 1 MeV neutron fluence Φ_{eq} through the relation:

$$\Phi_p(E) = \kappa \Phi_{eq} \tag{4.3}$$

κ is named hardness factor and defined:

$$\kappa = \frac{D_p(E)}{D_n(1MeV)}$$

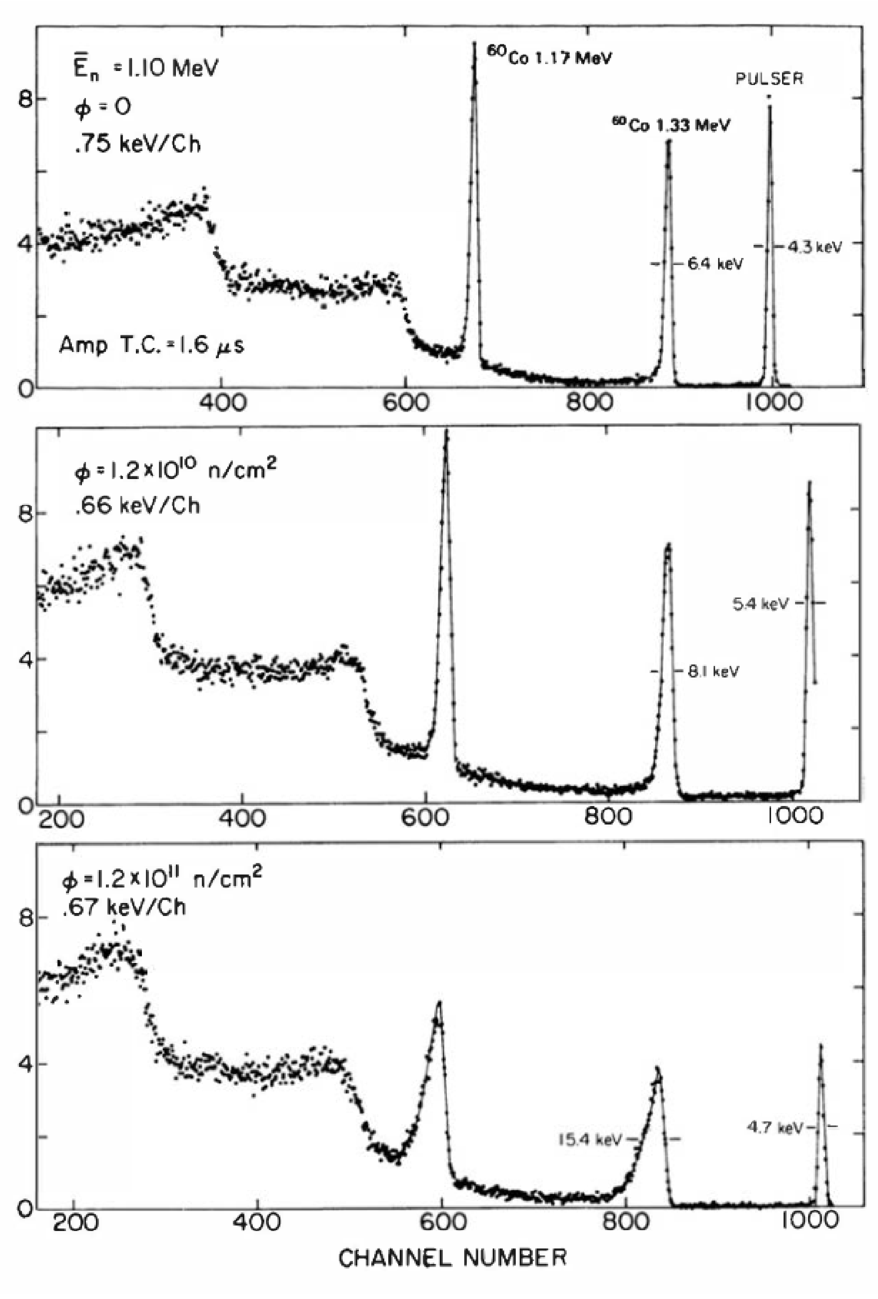

Figure 4.3: Deterioration of a Ge(Li) detector spectral performance after increasing exposure to energetic neutrons. Picture from [29].

$D_p(E)$ and $D_n(1MeV)$ are the induced displacement damage for a given p particle with an energy E and a 1 MeV neutron.
Values of $\kappa(E)$ for various particles and energies can be found in literature. Progressive decrease over time of the current-related damage rate is due to the annealing of various defects with different time constants, as shown in the following empirical relation:

$$\alpha(t) = \alpha_0 \exp\left(-\frac{t}{\tau_1}\right) + \alpha_1 - \alpha_2 \log\left(\frac{t}{\tau_2}\right) \tag{4.4}$$

All the parameters depend on the annealing temperature. At room temperature ($\sim 21°$ C) these values are: $\alpha_0 = 1.23 \times 10^{-17}$ A cm^{-1}, $\alpha_1 = 7.07 \times 10^{-17}$ A cm^{-1}, $\alpha_2 = 3.29 \times 10^{-18}$ A cm^{-1}, $\tau_1 = 1.4 \times 10^4$ min and $\tau_2 = 1$ min.

4.3 CHARACTERISTICS OF THE HERMES SDDS AND ORBIT

The HERMES Technological Pathfinder units will be deployed as piggyback of VEGA flights. The first opportunity will be the VEGA-C maiden flight in 2020, which should qualify the carrier and prove its good service to commercial orbits. This poses at least two issues: 1. the precise orbital elements will not be known until the main payload will be defined; 2. given the higher frequency of commercial launches compared to scientific ones, it is safe to assume that the first three units of HERMES will end up in a suboptimal orbit.

HERMES - TP units will most likely end in sub-optimal orbit.

For these reasons a comprehensive study of the threats that near-Earth environment - in particular particle radiation - poses to HERMES scientific instrumentation, should cover a wide region of the parameters space spanned by the orbital elements. Particular attention should be paid to LEO high-inclination orbits, towards which a large part of commercial vector flights are launched. Of course a careful characterization of space radiation damage on HERMES detectors cannot ignore the features of the detector itself.

Geometry and baseline noise levels of HERMES SDD detectors.

SDDs are silicon detectors in which the charge cloud produced after photon interaction is transported towards small anodes by means of a constant electric field, sustained by a series of cathode junctions at decreasing negative voltage. The SDD technology is discussed throughly in Section 5.2, to which the interested reader is referred. The HERMES detector will feature a collimated mosaic of 120 SDDs, each with a surface dimension of 7.44×6.05 mm^2 and a height of 450 μm. In the following calculation we will always refer to a SDD cell of such dimensions. The HERMES SDDs detector quality provides a baseline for the expected leakage current of 200 pA cm^{-2} at +20°C. Considering the HERMES SDD cells dimensions and leakage current temperature dependence as Equation 4.2, we expect a baseline value of ~ 2 pA from each cell.

4.4 THE HERMES RADIATION ENVIRONMENT

Space is a harsh place for scientific instrumentation. It pullulates with energetic particles, their flux varying widely with altitude and geographical coordinates.

With the exception of orbits at really high inclination, satellites in LEO orbits are effectively shielded from most of charged galactic and solar particles with energy below ~ 10 GeV by the Earth magnetic field. For this reason, the majority of particle flux is thus rapresented by the particles trapped in Earth's magnetosphere: protons and electrons. In the energy range of the most abundant particles in LEO orbits, the NIEL from protons is highly dominant over electrons for equatorial up to moderately inclinated orbits. The reason is really apparent considering Figure 4.2. An example will be useful in order to further elaborate. Even for a 70° inclinated orbit at an altitude of 600 km, the average integral electron flux varies from $\sim 10^5\,\mathrm{cm}^{-2}\mathrm{s}^{-1}$ to $\sim 10^3\,\mathrm{cm}^{-2}\mathrm{s}^{-1}$ over the energy interval between 0.1 and 1 MeV. On the same energy inteval, proton average integral flux varies from $\sim 10^3\,\mathrm{cm}^{-2}\mathrm{s}^{-1}$ to $\sim 10^2\,\mathrm{cm}^{-2}\mathrm{s}^{-1}$[1]. However, the hardness factor $\kappa(E)$ of electrons is about 4 orders of magnitude smaller than the one of protons between 0.1 and 1 MeV.

A note of caution should be made about albedo neutrons, a minoritary component of near-Earth radiation enviroment. Albedo neutrons are produced from the interaction between cosmic rays and atmospheric particles. Since cosmic rays are able to reach the atmosphere much more frequently at high latitudes, albedo neutrons fluxes increases from the equator to the poles. If on one hand considerations similar to those we made about the electron hardness factor hold true to some extent also for albedo neutron - the neuton hardness factor at 10 MeV is 30 time lower than protons -, on the other hand silicon detectors on higly inclinated orbits will experience a not negligible NIEL from albedo neutrons.

For equatorial, low-earth orbits an additional contribution to radiation comes from a highly directional population of protons near the geomagnetic equator, distributed below the Van Allen radiation belt, at an altitude between 500 and 1000 km.

Once all necessary caveats are made, it could be safely said that a study intended to predict displacement damage from low-Earth radiation in silicon detectors should start from the most dangerous radiation source of the near-Earth environment: trapped protons.

Trapped proton radiation is the main source of displacement damage in LEO.

Trapped protons are highly concentrated over a region of the magnetosphere known as South Atlantic Anomaly (SAA). At SAA, the inner Van Allen Radiation belt comes closest to the Earth surface going as deep as to an altitude of 200 km. At approximately 500 km, the SAA spans over a wide area, from $-50°$ to $0°$ geographic latitude and

---

[1] Data from SPENVIS AP/AE8 models.

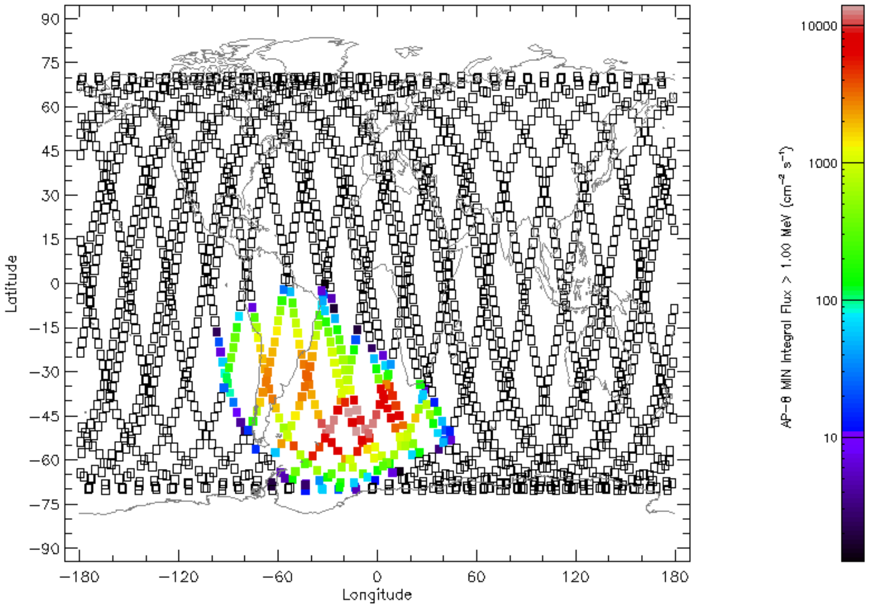

Figure 4.4: World map of the trapped proton flux encountered over twenty 70°, 600 km orbits. The extension of SAA is very apparent. From SPENVIS AP8 models.

from −90° to +40° longitude. A world map of the trapped proton flux encountered over twenty 70°, 600 km orbits is presented in Figure 4.4 and shows very well the SAA extension.

The 11-year solar cycle affects pretty much all the near-Earth particle concentrations. In particular, it induces a periodicity of low altitude trapped proton fluxes. During the solar maximum the Earth neutral atmosphere expands compared to solar minimum conditions, so that the low altitude edges of the radiation belts get 'eroded' due to the increased interactions with neutral constituents. As a consequence, the trapped proton flux at the solar minimum is generally higher than trapped proton flux at solar maximum. A comparison between the differential and integral photon flux at the minimum and maximum of solar activity as expected for an orbit at altitude of 600 km and an inclination of 70° is given in Figure 4.5.

4.5 ESTIMATE THE HERMES TRAPPED RADIATION ENVIRONMENT

SPENVIS [26][18] (SPace ENVironment Information System) is a web interface to a collection of software packages intended for space environment modelling. SPENVIS has been developed by ESA since 1999 and features the NASA AP/AE8, considered by ESA as the standard for radiation belt modeling [34].

The AP8 and AE8 models describe respectively trapped protons and

electrons. They include AP/AE8 MAX and MIN for trapped radiation modeling at the maximum and minimum of solar activity and feature extensive spatial coverage.
Since, as discussed in Section 4.4, the proton flux during a solar minimum is generally higher than the proton flux at solar maximum and since we are interested in quantifying a worst-case scenario of NIEL from trapped protons, the presented calculation will always be based on AP8MIN data. The AP8MIN average integral and differential proton flux expected for for orbits at various inclinations and an altitude of 500 km is presented in Figure 4.6.
SPENVIS also provide a package specifically for NIEL calculation, developed by BIRA-IASB and, showing quite a lack of imagination, named "*NIEL*" itself. The contribution to NIEL from trapped protons is calculated as the equivalent fluence through a range of (spherically symmetric) aluminium shielding to user-defined energy. In the following calculation we will adopt the default proton energy value of 10 MeV, for which the hardness factor is $k(E) = 4.8$ [49]. The calculated equivalent 10 MeV proton flux for various orbits as function of the equivalent Al shielding is presented in Figure 4.7. The shielding depth for HERMES detectors is expected to be around a few mm. For the present calculations a shielding value of 1 mm will be assumed.
Where indicated we will also take into account orbital degradation by atmospheric drag making use of realistic orbital decay curves simulated specifically for HERMES by the Aerospace Science and Technology Dept. of Politecnico di Milano for different solar activity scenarios, presented in Figure 4.8. The considered solar activity scenarios are: 1. nominal activity; 2. nominal activity minus 2 standard deviations; 3. (early) maximum plus 2 standard deviations. From the perspective of orbital degradation, the solar activity at maximum is the worst case scenario: during a solar maximum the atmosphere's inner and more dense layers raise at higher altitudes causing more atmospheric drag. It should be noted that for the following calculation the same orbital decay curves, calculated for an orbit with 70° inclinations, will be employed regardless of the actual orbit inclination. This is an approximation. Since atmospheric density at a fixed altitude varies with geographical coordinates because of the Earth's non-sphericity and geographical variation of atmospheric temperatures, the decay curves will depend on the initial orbital parameters such as inclination and RAAN.

4.6 RESULTS

In Section 4.1 we discussed the mechanism of displacement damage and how NIEL determines an increase of leakage current in silicon detectors, leading to a progressive degradation of the spectroscopic performances.

The increase of leakage current in HERMES-like SDD detectors at $-20°C$ as expected from Equation 4.1 are presented in Figure **??**, for a spacecraft in LEO orbit with an initial altitude of 500 km and a 70° inclination, convolving with orbital decay at day-long time steps in different solar activity scenarios. The assumptions made through Sections 4.5 and 4.3 have been applied.
Calculating the maximum allowable leakage current is not an easy task, since the precise value depends on the specifics of the payload electronics. Estimations made by LOFT-like SDD detectors and VEGA ASIC (from which HERMES LYRA FE/BE stems, cf. Chapter 3) suggest a maximum allowable leakage current of roughly 500 pA in order to ensue nominal payload activity at $+10°C$, corresponding to a trapped proton's radiation lifetime of ~ 900 days or two years and half.
Similar calculations have been performed for an array of orbit inclinations $I = \{5°, 10°, 20°, 30°, 50°, 70°, 98.2°\}$ at altitudes of 500 and 550 km. Figure 4.10 shows the expected increase in leakage current for an HERMES SDD cell after 6 months, 1 year and 2 years of activity at 500 km and 550 km and has been obtained by interpolating over a range of inclinations spanning 0° and 100°. Gaussian fit of the peaks at $\sim 40°$ results in a FWHM $\sim 50°$ and shows a strong correlation with the geographical extension of the SAA. We see that the increase in leakage current may result in a payload unable to guarantee nominal performance after 2 year of activity at orbits with the largest number of passages over SAA at an altitude of $\gtrsim 550 km$.
Is this a concern for HERMES mission? It is not. The HERMES units are cheap and small therefore easy to replace with new, possibly improved, spacecrafts. This *disruptive innovation* approach is typical of the microsatellite framework and HERMES makes no exception.

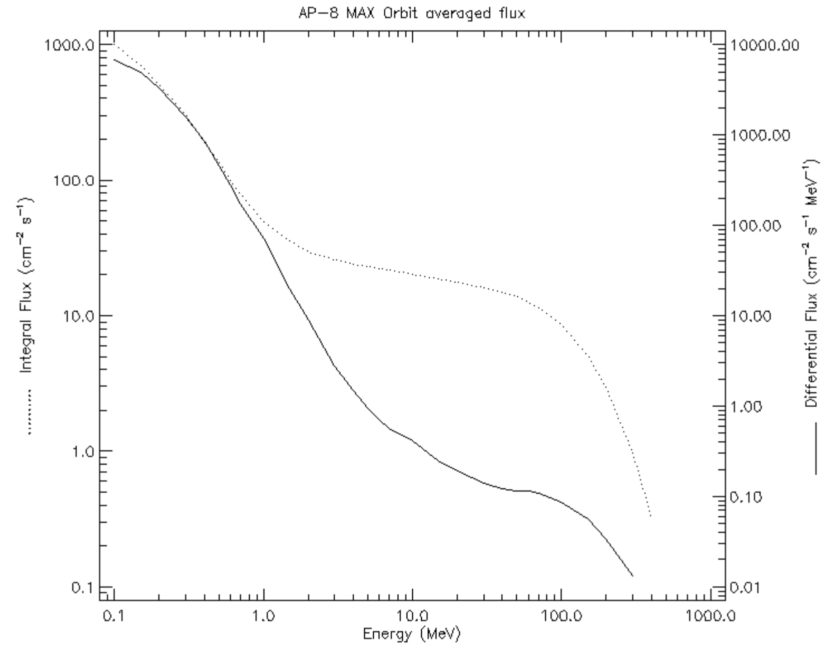

(a) Solar Maximum.

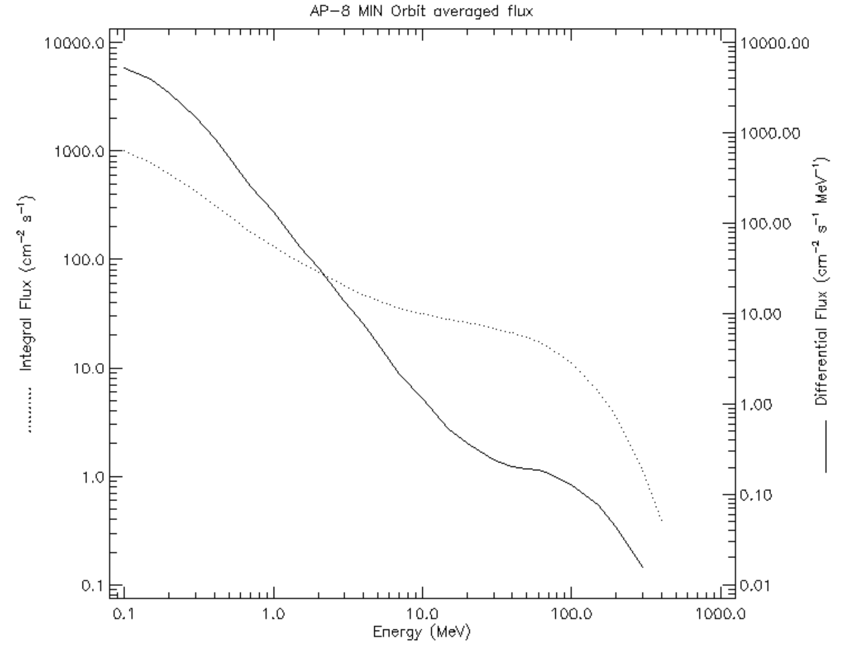

(b) Solar Minimum.

Figure 4.5: Differential and integral photon flux at minimum and maximum of solar activity as expected for an orbit at an altitude of 600 km and an inclination of 70°. Data from SPENVIS AP8 models.

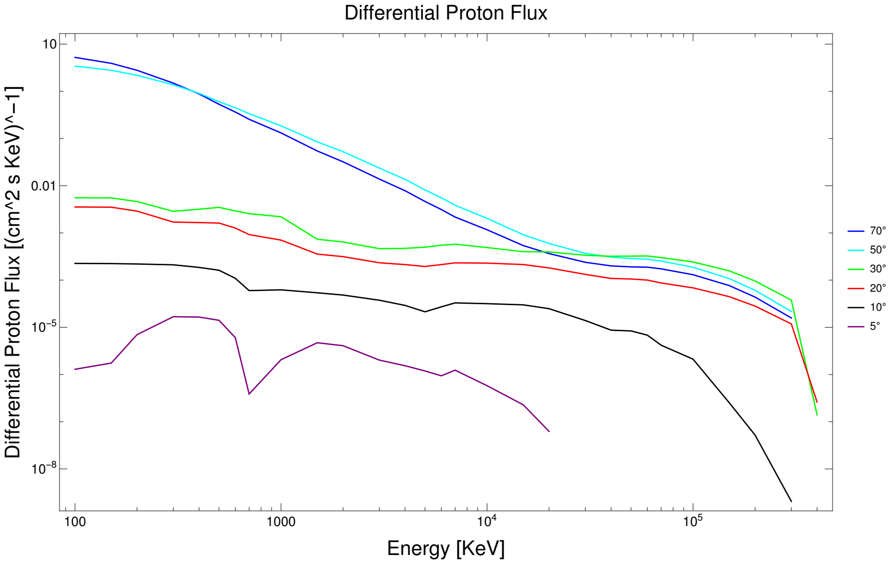

(a) Differential Proton Flux.

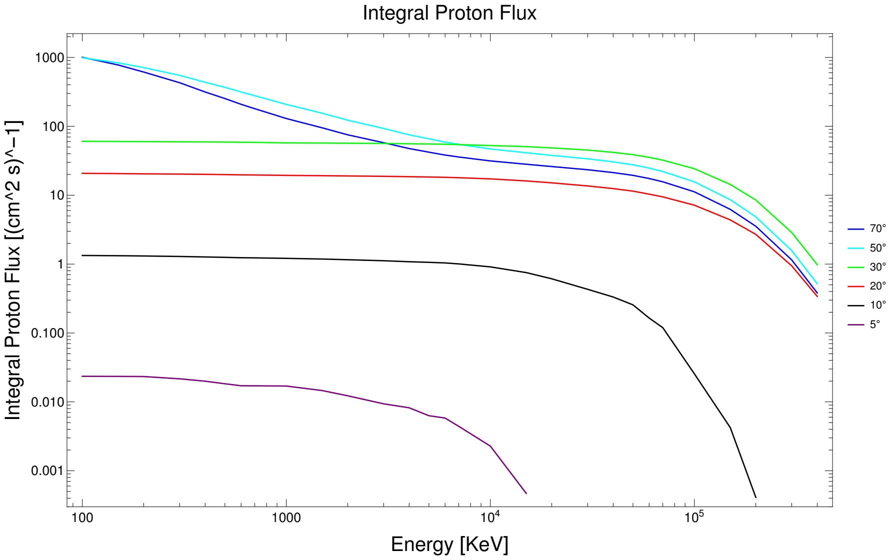

(b) Integral Proton Flux.

Figure 4.6: Differential and integral photon flux at minimum solar activity averaged over a year of operations, as expected for an orbit at an altitude of 500 km and indicated inclination. Data from SPENVIS AP8 models.

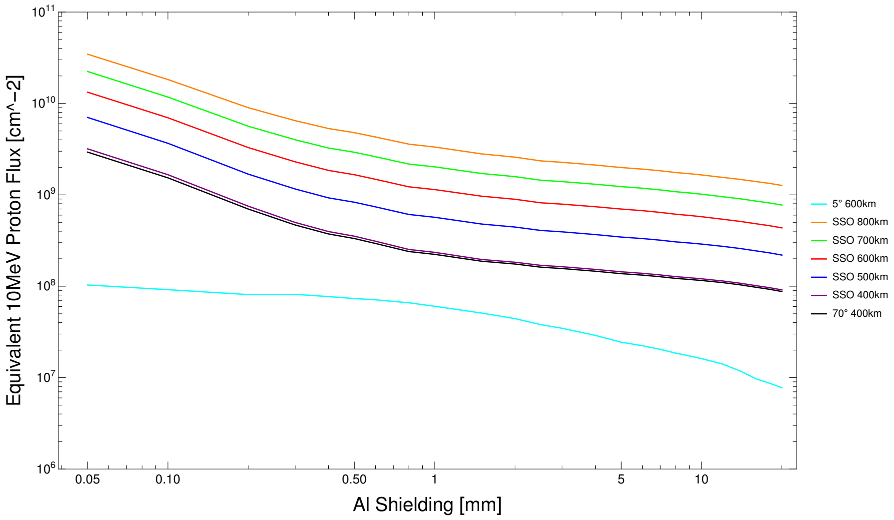

Figure 4.7: Equivalent 10 MeV proton flux behind aluminium shielding for different sun-synchronous orbits at varying altitude, a really low altitude 70°-inclinated orbit and a near-equatoriial 5° LEO orbit at altitude 500 km. Data from SPENVIS.

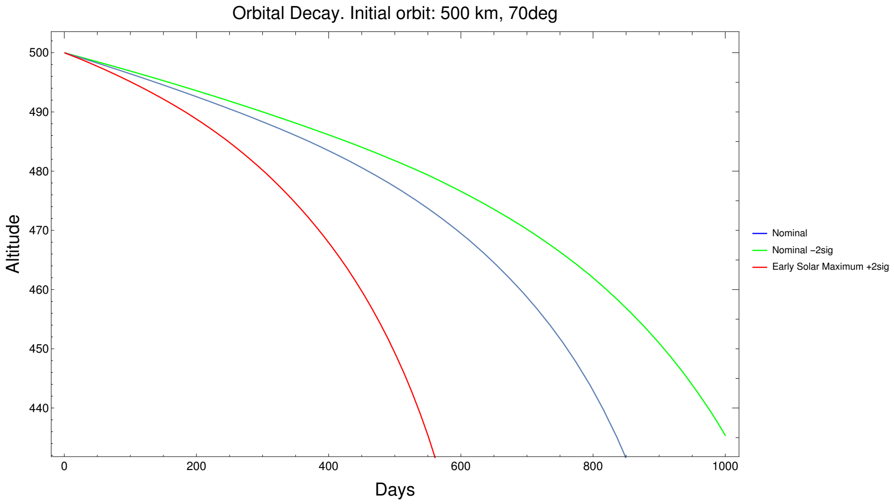

Figure 4.8: Orbital decay curve estimated for an HERMES spacecraft unit considering an initial orbital inclination of 70° at an altitude of 500 km and orbital decay in different solar activity scenarios. Data from simulations performed by Aerospace Science and Technology Dept. of Politecnico di Milano.

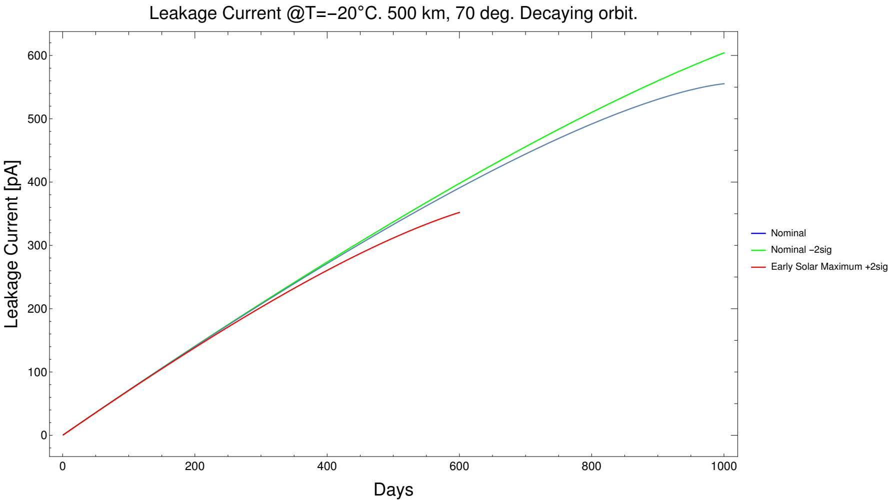

Figure 4.9: Leakage current increase as estimated for a HERMES SDD cell considering an initial orbital inclination of deg 70 at an altitude of 500 km and orbital decay in different solar activity scenarios (as calculated by Aerospace Science and Technology Dept. of Politecnico di Milano).

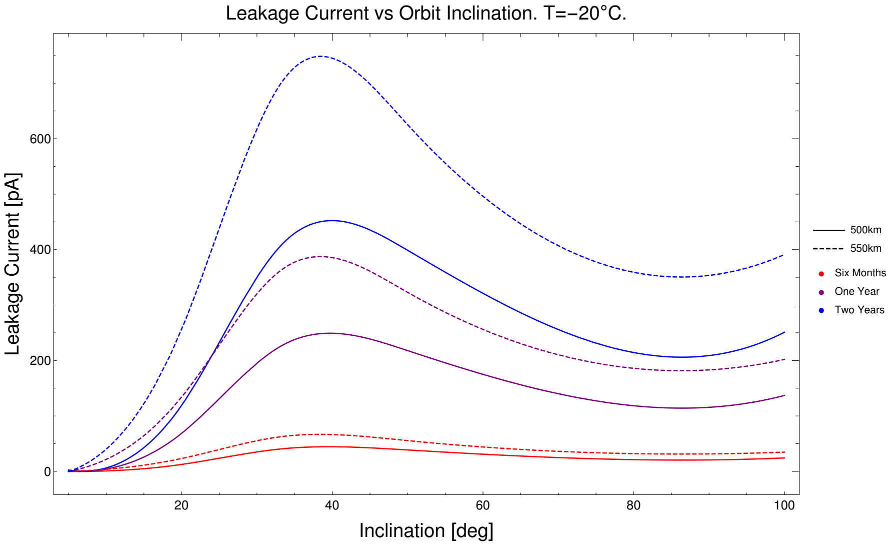

Figure 4.10: Expected increase of leakage current over a range of orbital inclinations for a single HERMES SDD cell on initial orbits at altitudes of 500 km and 550 km after 6 months, 1 year and 2 years of activity, considering orbital decay at nominal solar conditions.

5

DETECTOR TESTS AT THE BOLOGNA INAF CENTRE

The HERMES team will held a series of tests in order to determine the application feasibility of the scintillator crystals, as well as to extend and confirm space qualification analyses for small area SDDs and provide a first ground test for the detector implementation. The first test is expected to be held between fall 2018 and winter 2019 at Trento Institute for Fundamental Physics and Applications (TIFPA).

During the last week of July 2018 we held a hand-on analyses of the detector system at INAF laboratories in Bologna. The activity was intended to: 1. test a simple SDD-scintillator coupling strategy; 2. provide a small-scale ground to probe the experimental setup to be employed at TIFPA facility; 3. acquire the basic skills necessary to work with a full-fledged silicon detector system conceptually similar to the one to be employed on HERMES units.

In this chapter we start by briefly overviewing the components and tasks of a silicon detector system for radiation spectroscopy. This will serve as an introduction for a relatively in-depth discussion of the detector system to be employed aboard HERMES units, as will be discussed in Section 5.2. Lastly the activity and results of the laboratory activity held in Bologna will be presented in 5.3. The chapter will end with a review on the available literature about GAGG scintillator crystal and a discussion of the future activities envisioned for the TIFPA irradiation test campaign.

5.1 SILICON DETECTOR SYSTEMS

In humans eyes, light reaches the retina at the back of the eyeball where it forms back-wards, upside-down images. Cones and rods read and convert the image into a neural message. This message is delivered to the brain through the optic nerve.

In the animal world an incredible wide variety of eyes exist. Sensitivity to light, orientation, dimension, color and many other features vary to a great extent. In order to help the animals survive in their particular environment, components - such as cones and rods - differ accordingly.

Howevever, animal eyes all work towards the same goal: observe the sourrounding world. In most cases this task is accomplished through systems conceptually similar to the one just described for humans.

HERMES has its kind of eyes and they are made of silicon.

Silicon Drift Devices are the key component of HERMES's detector system, which is a particular case of silicon detector systems. As for eyes in the animal world, silicon detector systems may differ wildly in their details but share a common task achieved by different components with the same basic functions.

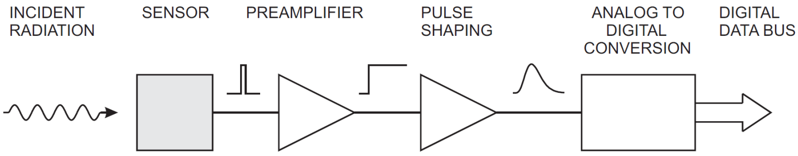

Figure 5.1: Basic detector components and functions: radiation is absorbed by the sensor and converted into an electrical signal. This low-level signal is integrated in a preamplifier, fed to a pulse shaper, and then digitized for subsequent storage and analyses [48].

The basic components of a silicon detector system are *sensors*, *preamplifiers*, *pulse shapers* and *analog-to-digital converters* (ADCs). They are represented with their respective functions in figure 5.1.

- The *sensor* converts the energy transferred by a photon (or particle) into an electrical signal. In semiconductors this happens when charge carriers are produced as a result of the photon's energy transfer. The number of carriers is proportional to the absorbed energy. An electric field is applied to the sensor and moves the carriers towards the electrodes, inducing electrical current for a brief time. More carriers means more current so that, after calibration, the initial photon energy can be reconstructed integrating the signal.

- The *preamplifier* has the task of amplifying the signal charge from the sensor. The sensor signal is associated to statistical and electronic noise. A good preamplifier should be designed in order to minimize noise contribution. In this regard key features are the total capacitance in parallel with the input. Low input sensors and preamplifiers capacitances makes for low noise in output from the preamplifier.

- The *pulse shaper* is meant for improving the signal-to-noise ratio. Shapers are often complex but can be conceptually reduced to a device constraining upper and lower bound of the input signal characteristic frequency spectrum. This is possible since the signal's and the noise frequency's distribution differs, so filtering out contribution from the regions dominated by noise - such as the very low and very high part of the spectrum - improves the signal-to-noise ratio. Modeling the signal frequency distribution cannot happen without changing the pulse shape in the time domain, henceforth the device's name.

  A simple model of pulse shaper is presented in fig. 5.2. The step signal coming out the integrator-preamplifier is moduled

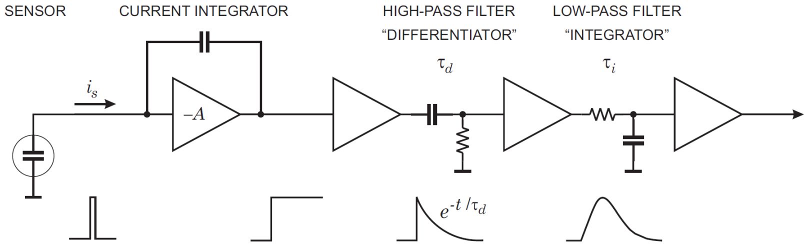

Figure 5.2: Components of a pulse shaping system. The signal current from the sensor is integrated to form a step impulse with a long (infinite) decay. This integrator serves as model for a preamplifier. A subsequent high-pass filter ("differentiator") limits the pulse width and the low-pass filter ("integrator") increases the rise-time to form a pulse with a smooth cusp [48].

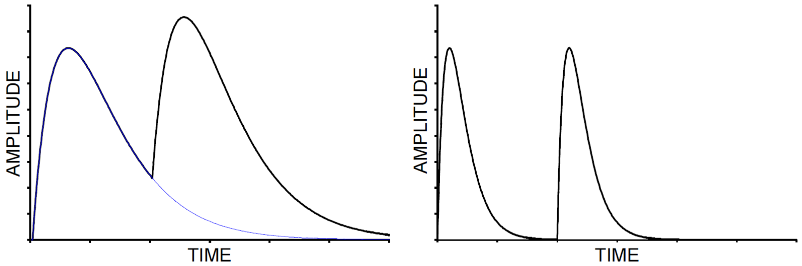

Figure 5.3: Amplitude pile-up occurs when two pulses overlap (left). Reducing the shaping time allows the first pulse to return to the baseline before the second pulse arrives [48].

by a pulse shaper composed of a CR high-pass and RC low-pass circuit, respectively introducing a decay and rise time to the signal. This is the result of limiting bandwidth of signal frequency distribution. The cut-off frequencies and decay-rise charateristics time are solely determined by the product R_dC_d at the differentiator and R_iC_i at the integrator.

In order to reconstruct the energy of the photon that caused the pulse interest should be payed in one major feature of the signal: its height. In 5.3 we can se what happens when two subsequent identical events are detected for two different shaping times. On the left panel the shaping time is not short enough to correctely separate the two detections, leading to a mismeasurement of the second peak amplitude. This effect is known as *pile-up* . On the right panel a briefer shaping time allows for a clean detection of the two events. Unfortunately a "quick" shaping time means greater noise..

Pile-up and pulse shaping

In designing a detector system is so important to find an optimum between the conflicting requirements of reducing noise and increasing speed.

- The *analog-to-digital converter* reads the continuous signal at finite time steps, converting it into unique output bit patterns.

SCIENTIFIC REQUIREMENTS	TECHNOLOGICAL CONSTRAINTS
Arcmin positioning.	$\sim$60 detectors on LEO orbit. Detector FoV ~ 2 steradian. GPS units positioning and timing. ACS with accuracy $\sim$ deg over hours.
Energy range* 5 - 300 keV. Time resolution $\sim \mu$s.	Innovative compact detector design. Temporal resolution of detectors $\lesssim 1\,\mu$s.
Fast dissemination.	Dedicated ground station network.

Table 5.1: Summary of HERMES scientific requirements and related technological constraints. *= Minimal target.

Generally speaking ADCs trade off higher converting speed for resolution and required power. ADCs are commonly interfaced to the pulse shaper through *sample-and-hold* circuits. A sample-and-hold circuit in an analog device that samples the voltage of an analog, possibly quickly varying, signal then holds its value at a constant level for a minimum period of time so that the ADCs can complete the processing and conversion operations.

5.2 HERMES SILICON DETECTOR SYSTEM

The scientific and high-level technological requirements leading the HERMES design were outlined in section 3.4 and are now briefly summarized in table 5.1. All these requirements are not impossible to achieve in the context of a normal-sized space mission. However, achieving these goals in the limiting environment of miniaturized spacecrafts is a challenge that requires careful design and the employment of innovative technology.
In particular, the CubeSat framework imposes the following lower-level technological constraints:

- The mass of the units must be kept below 6 kg.
- Power supply is limited to 4 watt, only one-third of which is allocated for the payload.
- The payload will be hosted by a single CubeSat unit of the three composing a HERMES unit. For this reason the geometric area of the detector will be under 10x10 cm^2.
- HERMES units should be able to operate on a sub-optimal orbit.

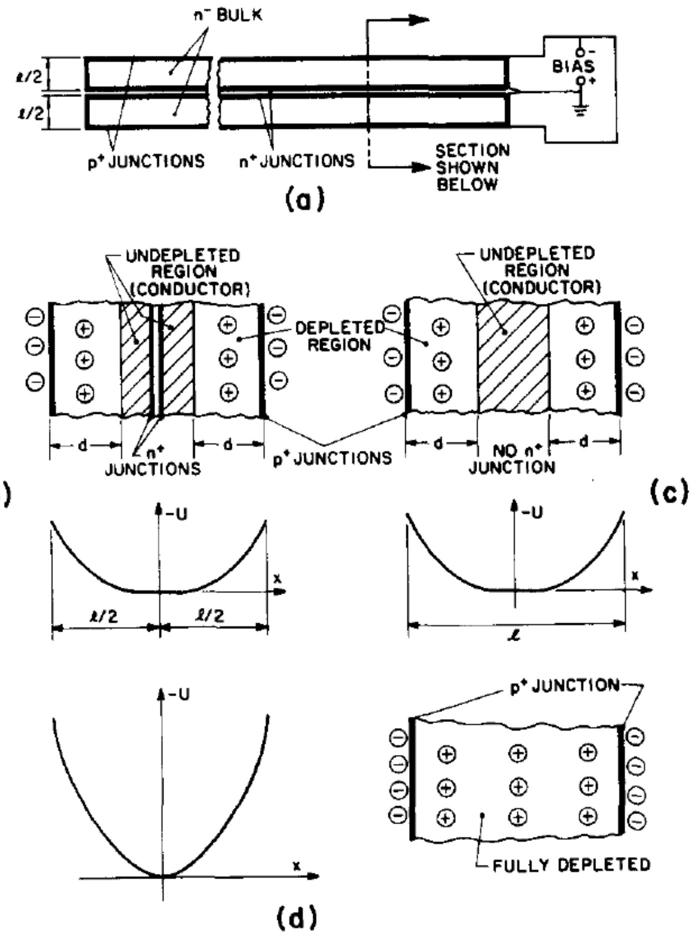

Figure 5.4: (a) Two np^+ junction are posed in contact with each other by n^+ contact, then the same bias voltage is applied to both; (b) depletion region after bias voltage is applied; (c) the same depletion region is obtained by a single np^+ junction twice the thickness; (d) bias voltage is increased until full depletion. From [22].

THE SENSOR: SILICON DRIFT DEVICE The requests for compactness, low mass and power supply, together with the robustness necessary for a detector to sit on a rocket, makes ruling out traditional gas-filled photomultipliers sensors unavoidable.
For its silicon detector system, HERMES will make use of a Silicon Drift Device (SDD) as the sensor.

The Silicon Drift Detector technology

SDDs were introduced for the first time by Emilio Gatti and Pavel Rehak in 1983 as high-resolution position-sensitive detectors for fast-ionizing particles and for X-rays spectroscopy. At the time silicon drift detectors were introduced, buried channel Charge Coupled Devices (CCD) were a well-known technology. CCDs confine photogenerated charges in a thin layer ($\sim 0.1\,\mu$m) at relatively shallow depth (< 4 mm). Charges are then laterally collected to read-out electronics by a clocking technique. CCD do not work well for high-energy. Typical

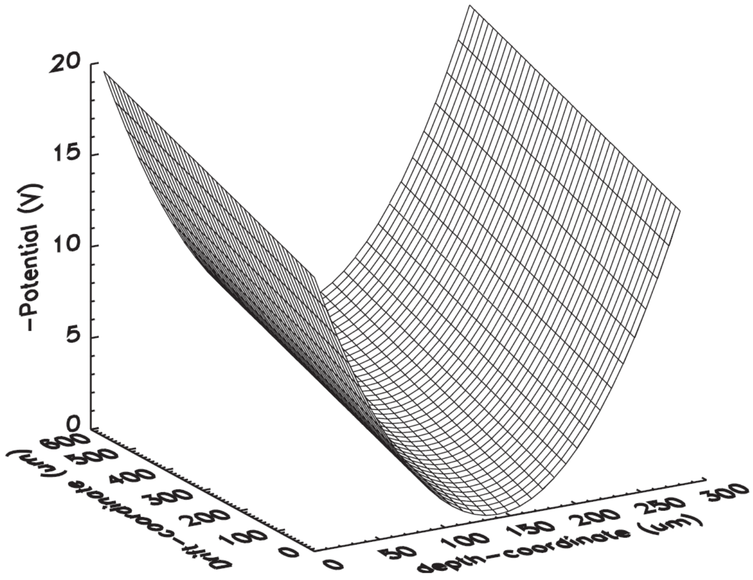

Figure 5.5: Ideal potential for a fully depleted silicon wafer with an additional linear field superposed along drift axis [23].

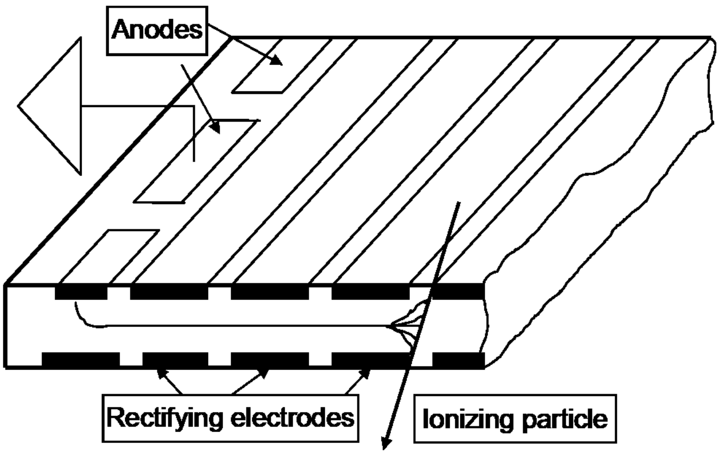

Figure 5.6: SDDs in multianode configuration. A linear potential is applied to rectifying electrodes in order to "incline" the potential [23].

application in radiation detection requires charge collection from silicon with a thickness of about about $0.1 - 0.5$ mm. In SDDs, collection from the complete body of the detectors is achieved by full depletion of the bulk of the silicon while sensitity is kept high employing DC voltage action for lateral removing instead of a clocking action.
How is this done? In 5.4.a two n-type silicon detectors with p^+ and n^+ junction at opposite sides of the wafer are depicted. A reverse bias is applied to both detectors. Figure 5.4.b shows the resulting depleted region and the potential across the two detectors. The n^+n junction does not play any role since its only function is to conduct the removed electrons from the depletion region to the external contact. Figure 5.4.c now shows the same situation achieved with a single semiconductor wafer with twice the thickness of the original ones, instead of two separate wafers. Since the undepleted central region act as a conductor, it can be used to replace the n^+ junction. Increasing the bias voltage, the depletion region increases its width at the expense of the thickness of the undepleted conductive channel. Applying a linear potential to a strip array of rectifying p^+n^- junctions on both faces of the detector (cf. figure 5.7), it is possible to "incline" the potential of figure 5.4 in such a way that thermally generated electrons are continuously swept towards a downstream anode. The uniform electric field applied along the channel axis also transports electrons towards the anode. The resulting potential is shown in figure 5.5.
In multianode configuration very accurate planar positioning is achievable. The distance between the anode and the regione where the ionizing particle crosses the middle plane is obtained from measurement of electron drift time. The second coordinate is given by the location of the particular anode collecting the charges. Since it is possible to keep the anodes dimensions very small, the resulting very small anode capacitance allows the development of extremely low noise electronics.

Although capable of position sensing, SDDs employed in HERMES act as photodiodes and produce an amplitude charge signal related to the observed amount of light. In order to provide a broad energy coverage, an array of SDDs is coupled to a scintillator crystal. Silicon detectors of ordinary depth can in fact detect X-rays with good efficiency only up to a few tenth of keV. Photons with energies up to a few MeV, are detected in the silicon device indirectly: hard X photons interaction with the scintillator cause the emission of optical light collected by the SDD. The discrimination between the two signals in the SDD (soft X-rays and optical light from scintillator) is achieved using a segmented design, as discussed in section 3.5.

Advantages of silicon drift devices as sensors

Why using SDDs? In SDDs electrons can be drifted over large distances and collected on electrodes of a very small size. The small size of the electrode makes for low sensor input capacitance, a key factor for achieving *low noise* level. Quantitatively, we are talking about tens

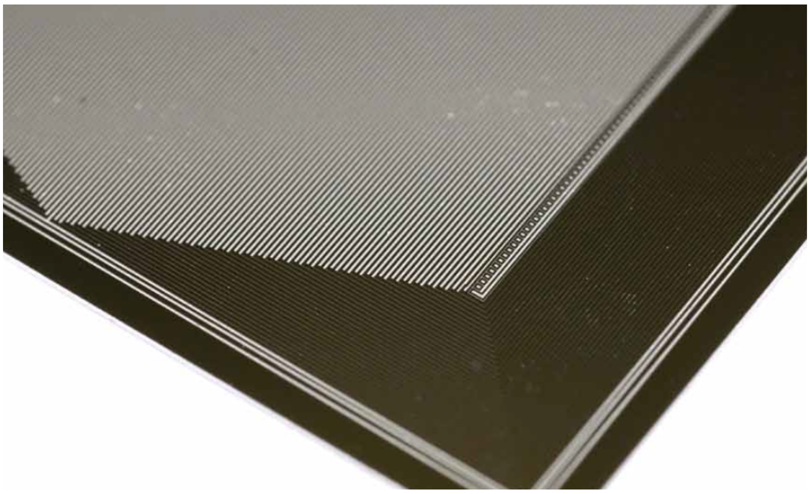

Figure 5.7: Close up of an SDD. The rectifying junctions and anodes are clearly recognizable. I wasn't able to find the original source, for corrections feel free to mail me at dilillo.giuseppe@spes.uniud.it.

of e^--rms at room temperature for a detector with a size of a few cm^2. Moreover, because the optimal shaping time for the minimization of the electronic noise shifts to lower values with decreasing detector capacitance, shorter shaping times and so consequently *high counting rate* are possible. For drift detectors, shaping times as short as tenth of nanoseconds can be achieved, while in traditional silicon detectors design shaping times are in the tens of microseconds range.

Using SDDs, it is possible to achieve a low noise level with modest cooling which the small HERMES spacecrafts will be able to provide. For comparison, regular silicon photodiodes at -50 C provide a comparable noise level of similar SDDs at 0° C.

Alternative sensors do not suit HERMES technological and scientific requirements

SDDs are not the only detectors for X spectroscopy to offer a low noise level. Silicon photomultipliers (SiPMT), the modern cousins of traditional phototubes, are capable of a very low noise level in a compact package. However these sensors are much more sensible to radiation damage then SDDs, making them less interesting for space application. Low noise level can also be obtained using photodiodes made of a material with a wider band gap than silicon. For example, mercuric iodide photodiodes have been shown to be attaining an energy resolution superior to that obtainable even with the best photomultipliers tube for gamma observation. Increased energy gap makes however for a much lower efficiency in the soft X band, where most of the GRB photons are emitted. Also, silicon is a well known material when it comes to space application. The same definitely does not hold true for a more exotic semiconductor such as mercuric iodide.

The SDD will be designed in collaboration with University of Udine and developed by *Fondazione Bruno Kessler* (FBK). The detectors in recent production bunch reached exceptional performances. Dark current was attested at 25 pA cm^{-2} and the noise level at room tem-

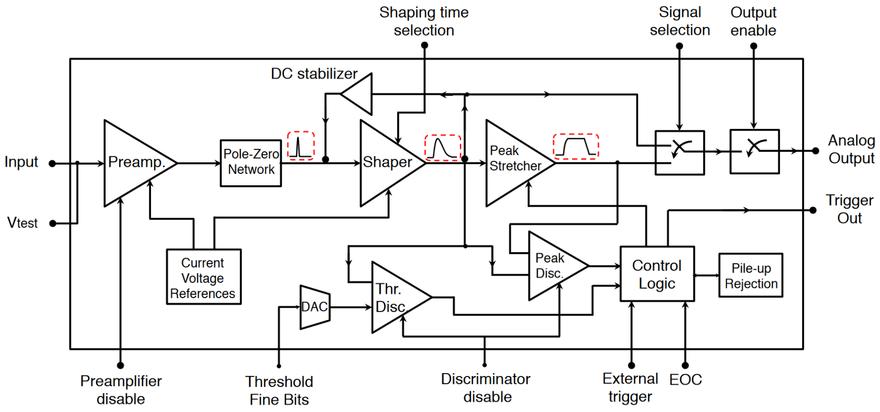

Figure 5.8: Diagram block for the VEGA ASIC [10].

perature of 7.4 e^{-}rms [5].

PAYLOAD ELECTRONICS: LYRA FE/BE The low input capacitance of SDDs makes it possible to attain a very low noise level with modest cooling. However, the final performance of the detector system will depend both on the quality of the sensor itself and on the behaviour of the electronics serving the readout of the sensor signal. As seen in the previous section, the detector system also need to be small and with a very low power consumption.

HERMES electronics need to be compact, low-noise and low-power consuming

These requirements makes the developement of high performance ASIC for the readout electronic necessary.

The design employed for HERMES is named *LYRA FE/BE*.

The heritage for HERMES electronic stems from the VEGA ASIC project [10]. VEGA is a mixed analogue/digital signal, low-noise, low-power multichannel ASIC developed by *Politecnico di Milano* and *Università di Pavia* in order to serve as FEE for the large area SDD detector of LOFT, a proposed ESA class-M space mission devoted to investigating X-ray rapid variability in neutron stars, black holes and other compact objects.

The VEGA ASIC

For this reason it was designed for rapid, high-resolution X-ray spectroscopy in the energy range between 0.5 and 60 keV and specifically optimized for the read-out of SDDs.

VEGA ASIC features 32 channel arrays with a dimension of 200 μm $\times$ 500 μm per channel. Each channel has been designed to have a total power consumption of less than 500μW.

A block diagram of the VEGA ASIC is presented in Figure 5.8. The analog section includes a low-noise, charge sensitive preamplifier for each channel, a CR-RC shaper and a peak stretcher/sample-and-hold circuit. Shaping times can be set in the range from 1.6 to 6.6 μs. The digital section features an amplitude discriminator with an adjustable

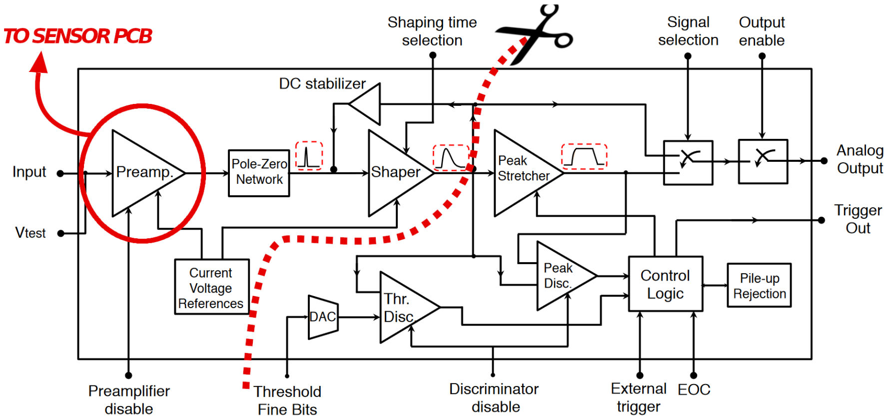

Figure 5.9: The concept behind FE/BE LYRA and its relation to the VEGA ASIC. The analog and digital part from VEGA have been separated in two different ASICs for FE/BE Lyra. The charge preamplifiers will be located on the same printed circuit board that will host the sensor in order to minimize input capacitance. Readapted from [10].

global and single channel threshold, and a peak discriminator. Signal sampling, pile-up rejection and generation of the reset trigger for preamplifier discharge are managed by a dedicated logic control unit. The shaped and stretched analog signal for each channel is multiplexed at the ASIC output. The ASIC is designed to be integrated with an embedded ADC.

Adapting VEGA ASIC for HERMES: LYRA FE/BE

In Figure 5.9 a concept block diagram of LYRA FE/BE is presented, relating the design to the "parent" VEGA ASIC.

The preamplifier serving the SDDs has been moved to the PCB hosting the SDD sensors. In this way we can keep the input sensor capacitance at a low avoiding unnecessary cabling to preamplifiers hosted by a different board. The analog signal processing units from VEGA will be hosted on an individual ASIC that will serve as FEE unit. This ASIC will be named LYRA FE.

The ADCs and the digital processing section from VEGA will be hosted by a different ASIC, named LYRA BE. LYRA BE will serve as the BEE and will be directly interfaced to the Payload Data Handling Unit (PDHU). It will host the ADCs, a control logic, the Event Data Generator (EDG), a clock for time marking and the FIFO memory and I/O interface with the PDHU. At the back-end level the analog signal coming from the LYRA FE will be time-tagged, converted to digital and then sent to the EDG. The EDG will be responsible to discriminate between low energy events (the ones coming from single SDDs) and high-energy events (the ones coming from multiple SDDs), give an energy estimation and manage the addressing to PDHU via the FIFO memory.

5.3 TEST ACTIVITY AND RESULTS

During the last week of July a hand-on analyses of the detector system has been held at INAF laboratories in Bologna. The activity was intended to: 1. Test a particular SDD-scintillator coupling technique; 2. provide a small-scale ground to test the experimental setup to be employed at TIFPA facility for the irradiation tests of SDD and scintillator crystal; 3. acquire the basic skills necessary to work with a full-fledged silicon detector system conceptually similar to the one to be employed on HERMES units;

GOALS We studied the spectroscopic performance and measured shaping time noise-corner for two setups. The first consists of an SDD, a preamplifier and a digital pulse processor (DPP). The second setup features a SDD-scintillator sensor attached to the same preamplifier and DPP of the first. The scintillator crystal was coupled to the SDD through silicon grease. The optical contact face was polished, while the remaining five were opaque and wrapped in teflon. The performance of this simple coupling technique were estimated measuring the effective scintillator light output and energy resolution .

THE SET-UP The scintillator crystal was a Gadolinium Aluminium Gallium Garnet (GAGG) sample commericalized by Advatech inc. with dimensions $1 \times 1 \times 3$ cm^3. Five of the six crystal faces were brushed. Optical coupling with SDD was obtained through silicon grease over a polished contact face. The SDDs under test in both setup had thickness 450μm and geometric area of 1×1 cm^2 . In both setups, the SDDs were mounted on a PCB also hosting the XGLab CUBE ASIC and housed in an aluminium case. CUBE is a charge sensitive preamplifier which operates in pulse reset mode designed for low-noise application at short peaking time. The preamplifier was operated by a single channel CUBE bias board. The output signal fed an Amptek DP5 high perfomance digital pulse processor. The sources used for irradiation were Am-241 and Cs-137. In particular, since Cs-137 strongly emits at 662 keV, it was used for the scintillator light characterization. Tests were performed in air and at room temperature (~ 21°C).

STRATEGY AND SUMMARY OF OPERATIONS The preliminary operations included checking the CUBE ASIC bonding and the wirings that will be used in order to connect the CUBE preamplifier and the power supply to the bias board. The bias board was powered and the output voltage checked and trimmed before attaching the CUBE ASIC. At this point the unit could be turned on for the first time. The output

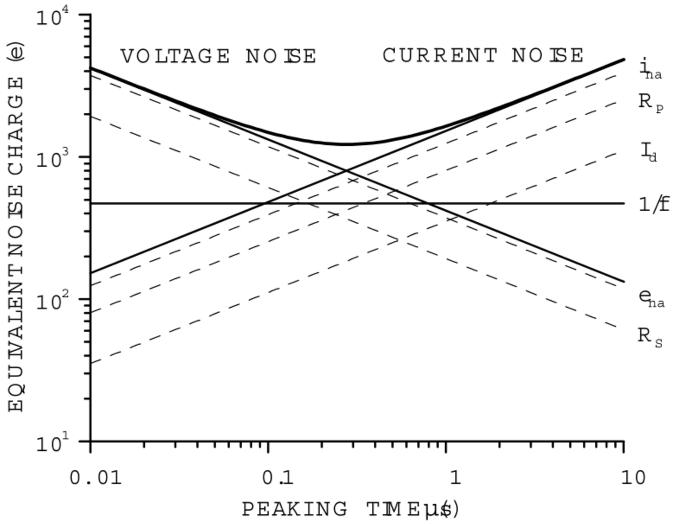

Figure 5.10: A typical plot of equivalent noise charge vs. peaking time with different contribution from individual noise sources. At short peaking times the voltage noise (preamplifier) dominates while at longer peaking time current noise (leakage current) takes over [29].

signal from leakage current was sent to an oscilloscope where the expected preamplifier reset waveform was observed .
The SDD was then irradiated with a radioactive Am-241 source. The signal was observed at the oscilloscope, also making use of a simple differentiator. After connecting with the DP5 pulse processor we were able to acquire and calibrate the first emission spectrum.

The DP5 is optimized for accurate pulse height measurement. It utilizes digital trapezoidal pulse shaping providing optimum signal-to-noise ratio for many systems and reducing pile-up. Users are able to adjust the rise/fall time i.e. the peaking time.

Determining the best shaping time is a key passage in silicon detector system optimization

Adjusting peaking time to the optimal value is a key parameter in order to optimize the system configuration. There is usually a trade-off: short peaking times minimize dead time, yielding high throughput and count rates. On the other hand the electronic noise increases at short peaking times. Electronic noise generally has a minimum at a particular value of peaking time, known as the "noise corner". At peaking time shorter or longer than this value, there is more noise hence sub-optimal resolution (cf. Figure 5.10).

Ballistic deficit

Other than the noise, count rates and balistic deficit should be taken into account when choosing the right peaking time. If the peaking time is too long for the rate of incoming count, pile-up will occur. If the optimal value is too long for avoiding pile-up, a lower but noisier value could be necessary to accomodate higher count rates.
On the other hand,a risetime from the preamplifier which is too long compared to the peaking time will result in loss of pulse height, the

"ballistic deficit". In our setup, a longer risetime may result from electron diffusion following an event at the edge of the SDD cell. Longer risetime are also expected from the scintillator events, since scintillator light will irradiate the entirety of the SDD detector.

In order to determine the noise corner we acquired and calibrated multiple spectra of the Am-241 source at different peaking times and studied the energy resolution for each one. The Am-241 uncalibrated spectrum acquired at 0.8 μs peaking time is shown in Figure 5.11,a. We then proceeded to substitute the detector with the coupled SDD-Scintillator. The Am-137 spectra were acquired again for a different set of peaking times The same peaking times were used in the following set of measures performed with the radioactive gamma source Cs-137. Am-241 and Cs-137 uncalibrated spectra acquired at 4.8 μs peaking time are shown in Figure 5.11,b-c. After cross-calibrating the caesium and americium spectra we were able to measure the energy resolution and effective light output of the scintillator crystal as function of the peaking time.

RESULTS The energetic resolution of the silicon drift detector as function of the peaking time is presented in Figure 5.12. The 'noise-corner' is really apparent. The best energy resolution of $2.10 \pm 0.04\%$ has been obtained for peaking time $\tau_p = 0.8\,\mu$s
Energy resolution as function of the peaking time for the SDD-scintillator coupled detector is shown in Figure 5.13. In this case the best energy resolution $2.8 \pm 0.2\%$ has been obtained for peaking time of $\tau_p = 2.0\,\mu$s. We can observe that ballistic deficit caused a "stretching" of the energy resolution curve.
The effective light output of the scintillator crystal is presented in Table 5.2 and Figure 5.14. The best measured scintillator effective light output was attested at $9.37\,\mathrm{photons\,keV^{-1}}$ and has been achieved for the longest peaking time, $\tau_p = 4.0\,\mu$s. The growth effective light ouput over increasing peaking time is again a consequence of ballistic deficit: the optical light from the scintillator crystals hits the whole surface of the SDD resulting in a charge cloud of dimensions comparable to the silicon detector surface henceforth needing long shaping time in order to be acquired. Comparing the best measured effective light-output to the expected light-output of GAGG crystal $\sim 50\,\mathrm{photons\,keV^{-1}}$, we conclude a low value of efficiency $\lesssim 0.2$ was reached for our simple optical coupling technique through silicon grease.

5.4 THE GAGG SCINTILLATOR CRYSTAL

The Gadolinium Aluminium Gallium Garnet (GAGG, $Gd_3Al_2Ga_3O_{12}$ with $0.2 - 2\%$ cerium doping) scintillator crystal was developed in Japan in 2010. It has been available for industry since 2014. GAGG is

τ_p [μs]	L.O [ph keV^{-1}]
0.4	2.5
1.0	4.2
2.0	6.9
3.2	8.5
4.8	9.4

Table 5.2: Scintillator effective light output calculated for the Cs-137 662 keV emission line.

one of the brightest scintillator available with an attested light output of $\sim 40000 - 60000\,\mathrm{photons\,MeV}^{-1}$. Radiation decay time is $\sim$ 90 ns. The emission spectrum is presented in Figure 5.15 and does peak at 520 nm. Physically it is very rugged and not hygroscopic. Its density is high at $6.63\,\mathrm{g\,cm}^{-3}$, its melting point is 1850°C and its hardness on the Mohs scale is 8. The energy resolution at 662 keV is $\sim$ 5%, a value comparable to thallium-doped caesium iodide (CsI:Tl) scintillator.

Because of its novelty, the literature about GAGG scintillator crystals is still lacking. Nonetheless, studies about possible space application are being encouraging.

In particular, in 2018 Yoneyama et al. [55] demonstrated that:

- GAGG scintillator crystals shows excellent linearity between light yields and deposited energy over a wide range of energies ($50 - 1836$ keV). Cf. Figure 5.16.a.
- Optimal light yield is achieved at -20°C. Temperature dependence is attested within $5 - 20\%$ between -20°C and $+20$°C. Cf. Figure 5.16.b. For comparison the bismuth germanate (BGO) temperature dependence over the same interval of temperatures is 50%.
  Scintillation decay time slightly increases lowering the temperature. The decay time change between -40°C and $+40$°C is $\sim$ 12% . Similar results were found by [31]. Decay time over the same temperature interval changes by $\sim$ 50% in CsI:Tl.
- Co-60 irradiation proved small light-yield degradation after a 100 krad dose (approximately the expected dose from 100 year of LEO). The spectra of Cd-109 obtained before and after the Co-60 irradiation shows peak positions differing by $\sim$ 10% , a similar value to that observed for BGO. Cf. Figure 5.16.c. It should be noted that Co-60 emits between 1170 and 1332 keV and for this reason only partially mimics the space environment.
- Substantial afterglow is observed over a few hours. This is a peculiar GAGG behaviour, only marginally shared by other scintillator such as BGO and CsI. The afterglow is expected to

	GAGG:CE	BGO
Before Irradiation	$0.25 \pm 0.01\,\mu$A	$0.14 \pm 0.01\,\mu$A
After Irradiation	$23.27 \pm 0.01\,\mu$A	$0.15 \pm 0.01\,\mu$A

Table 5.3: Afterglow current values of GAGG:Ce and BGO before and after 300 s from 100 krad of Co-60 irradiation. From [55].

significantly affect the spectroscopy accuracy. It was measured that after 30 s of LED irradiation, afterglow contributed to 2% degradation in energy resolution during the first 100s of observation. The energy resolution returned to nominal value after 400s. Cf. Figure 5.16.d. Over the temperature interval between 0°C and 20°C it was found that afterglow intensity increased with increasing temperature.

Large amounts of energy deposited by electrons may cause a similar afterglow as observed in LED light irradiations. Afterglow after irradiation of 100 krad dose from Co-60 source confirmed that GAGG emits an afterglow with a long decay time ($\sim$ days). Observed decay law suggest that afterglow owing to LED irradiation and to electrons and gamma-ray from Co-60 irradiation appear to be caused by similar process. Comparisons of afterglow currents of GAGG:Ce and BGO before and after Co-60 irradiation are concerning, as shown in Table 5.3 Experiments with magnesium-doped sampled showed that if on one hand co-doping with Mg implies a worse light yield, on the other hand it results in dramatic afterglow reduction. Similar results were found by [51].

Afterglow emission is the main cause of concern in regard GAGG application in space.

We can deduce that GAGG is a very promising scintillator crystal urging further investigation before space application. Afteglow emission behaviour is of particular concern:

> *GAGG displays an atypical and intense afterglow behaviour. The afterglow is expected to significantly affect the spectroscopy accuracy. Irradiation of 100 krad Co-60 dose resulted in worrying levels of afterglow emission (cf. Table 5.3).*
> *Experiments on afterglow temperature dependence from an unirradiated sample showed emission levels ranging over two order of magnitudes in the temperature interval between 0°C and +20°C. Temperature dependence of GAGG afterglow after substantial irradiation is still unknown.*

It is important to remark that a 100 krad dose is equivalent to roughly 100 years of a typical LEO radiation dose and should therefore be considered an unrealistic dose for space application.

Moreover, Co-60 nuclear radiation only partially rapresents the typical space radiation environment.

5.5 FUTURE ACTIVITIES: THE TIFPA TESTS

In order to shed light on the concerning points about space applicability of GAGG scintillator crystals, the HERMES team will held an independent test campaign. In particular, the tests will aim at further investigating GAGG afterglow emission after irradiation. They will also be an opportunity to further probe space qualification analyses of small area SDDs.
The goals of the tests can be summarized as follows:

- Evaluating GAGG afterglow emission and variations in optical properties at increasing dose steps of radiation rapresentative of the actual in-orbit radiation environment foreseen for HERMES operations.
- Evaluating the increase in the leakage current resulting from radiation damage and annealing effects on small area SDDs.

Where should these test be held?? To ensure the success of the test campaign, it will be fundamental to employ a radiation source rappresentative of the HERMES expected radiation environment. Since HERMES units will operate on LEO orbits the best irradiation facility candidates will source protons at tenth or hundreds of MeV energies. The Trento Institute for Fundamental Physics and Applications (TIFPA) irradiation facility hosts a 70 MeV proton beam accelerator and is henceforth well-suited for the purpose.
The analyses of Chapter 4 indicates that the 10 MeV equivalent proton fluence expected after one year of circular orbit at an altitude of 500 km and an inclination of 70° is $\sim 5.5 \times 10^8$ protons cm^{-2}. Considering an hardening factor for 70 MeV protons, $k = 1.52$, we can use Equation 4.3 in order to estimate the equivalent 70 MeV doses at increasing steps rapresentative of different space operation periods. Equivalent doses for 6 months, 1 year, 2 years, 5 years and 10 years of activities are presented in Table 5.4.

STEP	10 MEV DOSE	70 MEV DOSE	BEAM TIME
6 months	2.8×10^8 p cm^{-2}	7.3×10^8 p cm^{-2}	1 min
1 year	5.5×10^8p cm^{-2}	1.4×10^9 p cm^{-2}	1 min
2 years	1.1×10^9 p cm^{-2}	2.9×10^9 p cm^{-2}	2 min
5 years	2.8×10^9 p cm^{-2}	7.3×10^9 p cm^{-2}	6 min
10 years	5.6×10^9 p cm^{-2}	1.5×10^{10} p cm^{-2}	10 min

Table 5.4: Calculated equivalent 70 MeV proton radiation dose after increasing period of circular orbit at altitude 500 km and inclination 70°. Beam time is calculated supposing 58.4 nA extraction current.

How much time will be needed by the TIFPA accelerator in order to provide the predicted radiation doses? The beam intensity is adjustable over a range between 1 and 320 nA, corresponding to 70 MeV proton flux with intensity between 3.8×10^6 and 3.8×10^8 particles per second. The TIFPA proton beam profile is gaussian with an FWHM ($\sim$ 75% of gaussian area) $\sim$ 3.2 cm at two meters from the source. Supposing to irradiate the lateral face of a GAGG crystal with a dimension of 3×1 cm^2 posed at two meters from the source, we can estimate exposition times for the 5 years step ranging from $\sim$ 2.1 hours to 25 seconds at minimum and maximum beam intensity respectively. Consequently, at a beam extraction current of $\sim$ 58.4 nA, $\sim$ 1 minute will be needed in order to provide 6 months of radiation dose. In order to provide the total 10-years radiation dose $\sim$ 20 minutes of beam activicty will be needed. Considering 30 minutes in order to prepare the beam between one irradiation step and another, we can estimate a total time of 2 hours and 50 minutes for the complete measurement. SDD irradiation tests will follow the same steps and timetable.

The experimental setup will be very similar to that employed by Yoneyama et al. A sample of GAGG crystal with a dimension of $1 \times 1 \times 3$ cm^3 will be optically coupled to a photomultiplier tube properly shielded from the proton beam through a radiation-resistant optical waveguide a few centimeters long. The afterglow effects will be evaluated during and immediately ($\sim$ seconds) after the irradiation. SDDs increase of leakage current will be measured after each irradiation step and kept under observation for a few days after irradiation, then the effects of annealing at 50°C will be tested. The scintillator's optical properties will be studied a few days after the TIFPA irradiation.

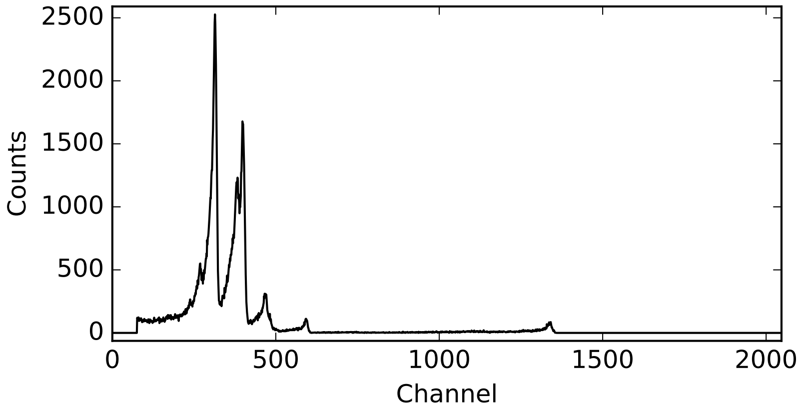

(a) SDD Am-241 X-ray spectrum at 0.8 μs peaking time.

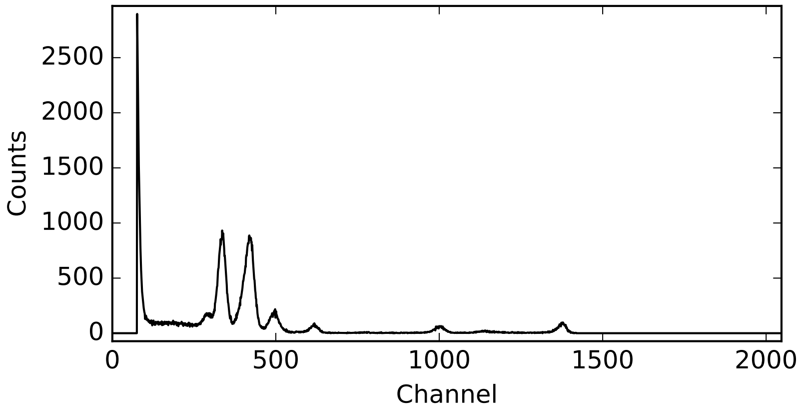

(b) SDD-scintillator Am-241 X-ray spectrum acquired at 4.8 μs peaking time.

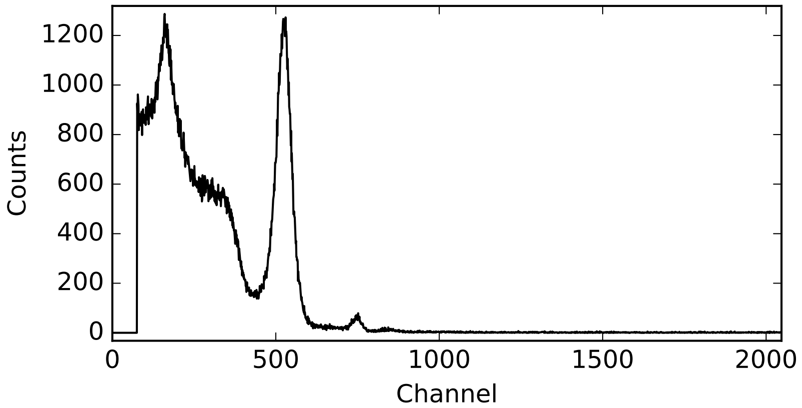

(c) SDD-scintillator Cs-137 γ-ray spectrum acquired at 4.8 μs peaking time.

Figure 5.11: Different spectra acquired during laboratory activity.

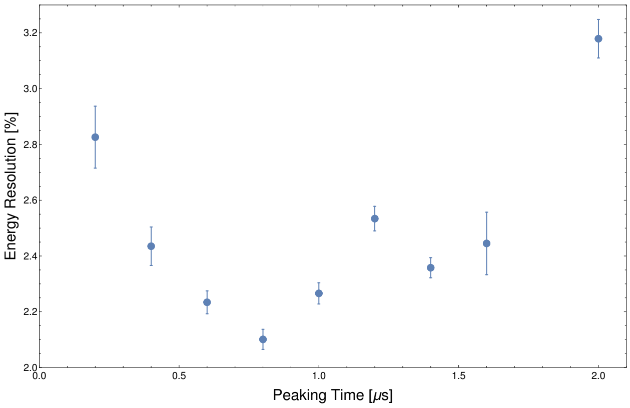

Figure 5.12: Peaking time versus SDD measured energy resolution, calculated for the Am-241 26.34 keV emission line.

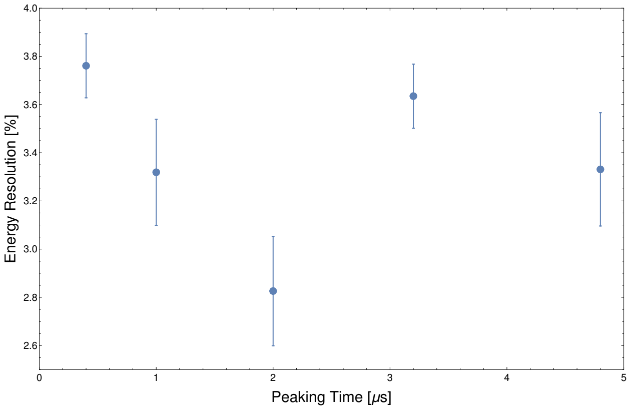

Figure 5.13: Peaking time versus SDD measured energy resolution in coupled SDD-scintillator detector, calculated for the Am-241 26.34 keV emission line.

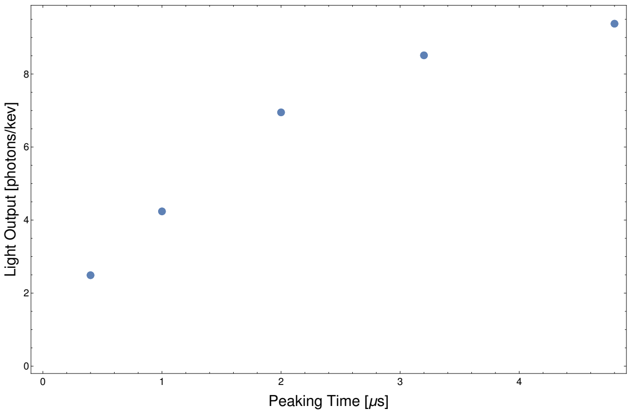

Figure 5.14: Peaking time versus effective light output measured for the scintillator crystal optically coupled to the SDD by means of silicon grease.

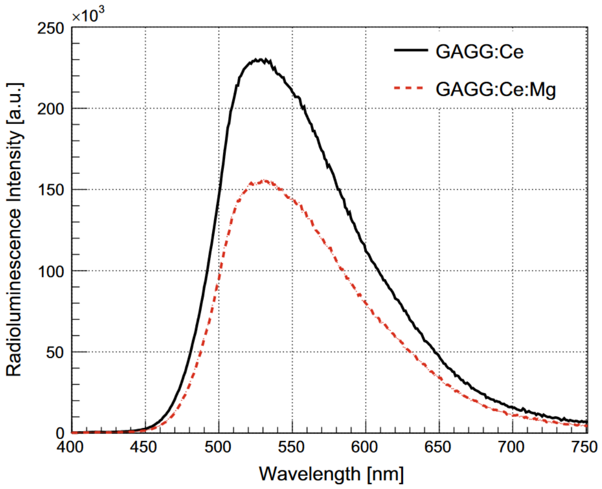

Figure 5.15: GAGG emission spectrum under excitation by X-ray tube for the GAGG:Ce and magnesium-doped GAGG:Ce crystals. From [36].

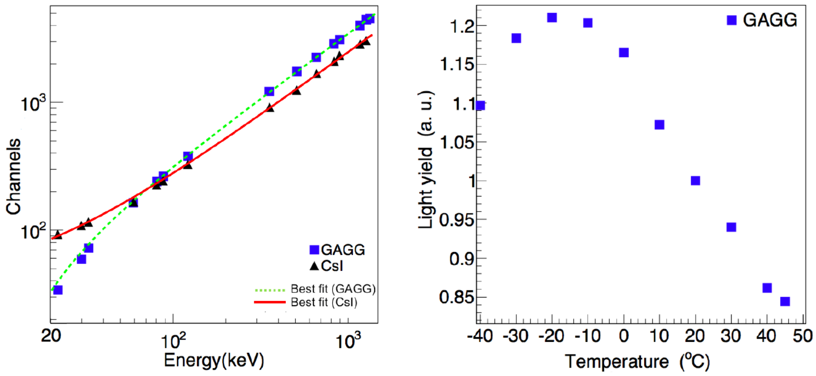

(a) Linearity between light yields and deposited energy.

(b) Optimal light yield is achieved at $-20°C$.

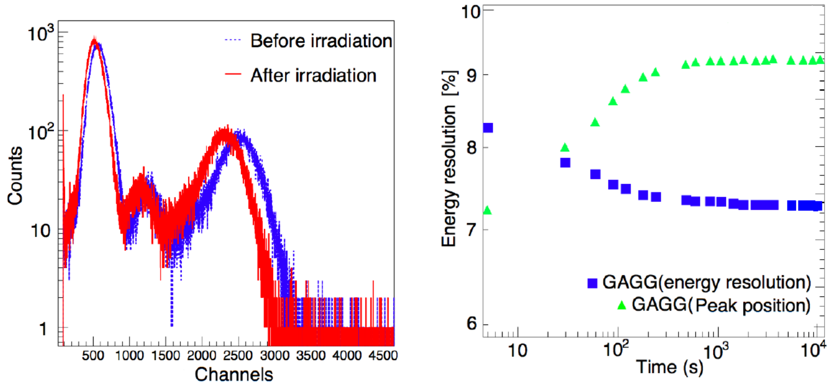

(c) Little degradation after 100 krad dose of Co-60 irradiation.

(d) Afterglow causes significative spectroscopic performance degradation.

Figure 5.16: The main results from the work of Yoneyama et al. [55].

CONCLUSIONS

Something that I've grown to love in the months spents working on this thesis, is that HERMES is a project which dares to pursue great ambitions with limited resources. This circumstance would not be possible without a brilliant mission concept, at the heart of which it lies a small and innovative detector design. With this thesis I had the chance to investigate some of the threats near-Earth environment poses to the HERMES Pathfinder units detector systems and to follow its implementation:

- The exposure of silicon detectors to space radiation results in a progressive increase of leakage current henceforth spectral resolution degradation. We estimated the increase of leakage current due to trapped proton radiation for a wide variety of realistic orbits. The results are best summarized by Figure 4.10
- GAGG is a novel and promising scintillator crystal which has never flown. At the Bologna INAF laboratories we set up a full spectroscopic detector system and estimated the performance of a simple SDD-scintillator coupling technique by means of silicon grease, determining the scintillator effective light output. Measurement results are presented in Table 5.2 and Figure 5.14.

Both analyses should be considered in the grand scheme of the preliminary efforts held towards test campaign that is expected to start in the near future, with scintillators and SDDs studies to be held at TIFPA facilities. The TIFPA tests are expected to further confirm small-area SDDs space qualification, quantify potentially concerning GAGG properties relevant to its space applications as well as be a first ground for testing implementation solutions.

Trapped protons are the main, but not only the unique, source of displacement damage in low-earth orbit. Moreover, an increase of leakage currents should be expected from ionizing radiation as well. The work on spectroscopic perfomances degradation due to radiation damage can be improved by further considering - especially at high orbital inclinations - different sources of displacement damage, taking ionizing radiation into account and determining how micrometeorids and other hypervelocity particles impact the operations of small-SDDs. Most importantly, the work on near-Earth environment should proceed in order to provide a careful simulation of the X-ray background. This knowledge will prove essential to the achievement of the best localization accuracy using the smallest number of units.

Working on this thesis I had the opportunity to acquire the know-how and skills necessary to work with GRB astrophysics and on the

technology necessary for space observation of such fascinating class of phenomena. I hope to have the chance to bring this work further during the next three years of my PhD.
I sincerely wish this small - but heartfelt - contribution will support the success of the HERMES mission.

BIBLIOGRAPHY

[1] 1997. URL: http://www.cbat.eps.harvard.edu/iauc/06600/06655.html.

[2] B.P. Abbott et al. "Multi-messenger observations of a binary neutron star merge." In: *Astrophysical Journal Letters* 848.L12 (2017), p. 59.

[3] D. Band et al. "BATSE observations of gamma-ray burst spectra. I - Spectral diversity." In: *The Astrophysical Journal* 413 (Aug. 1993), pp. 281–292. DOI: 10.1086/172995.

[4] E. Berger. "Short-Duration Gamma-Ray Bursts." In: *Annual Review of Astronomy and Astrophysics* 52 (Aug. 2014), pp. 43–105. DOI: 10.1146/annurev-astro-081913-035926. arXiv: 1311.2603 [astro-ph.HE].

[5] G. Bertuccio et al. In: *IEEE Transactions on Nuclear Science* 63.1 (2016).

[6] Ž Bošnjak et al. "The spectral catalogue of INTEGRAL gamma-ray bursts: results of the joint IBIS/SPI spectral analysis." In: *Astronomy and Astrophysics* 561, A25 (Jan. 2014), A25. DOI: 10.1051/0004-6361/201322256. arXiv: 1309.3174 [astro-ph.HE].

[7] M. S. Briggs et al. "Observations of GRB 990123 by the Compton Gamma Ray Observatory." In: *The Astrophysical Journal* 524 (Oct. 1999), pp. 82–91. DOI: 10.1086/307808. eprint: astro-ph/9903247.

[8] Michael S. Briggs et al. "BATSE Observations of the Large-Scale Isotropy of Gamma-Ray Bursts." In: *The Astrophysical Journal* 459 (1996).

[9] Santa Cruz University of California. *One-Meter Two-Hemispheres (1M2H) Collaboration*. 2017. URL: https://reports.news.ucsc.edu/neutron-star-merger/media/.

[10] R. Campana et al. "Characterization of the VEGA ASIC coupled to large area position-sensitive Silicon Drift Detectors." In: *Journal of Instrumentation* 848.8 (2014), P08008.

[11] S. Campana et al. "The association of GRB 060218 with a supernova and the evolution of the shock wave." In: *Nature* 442 (Aug. 2006), pp. 1008–1010. DOI: 10.1038/nature04892. eprint: astro-ph/0603279.

[12] A. Chilingarov et al. "Radiation Damage due to NIEL in GaAs particle detectors." In: *ATLAS Internal Notes* 134 (1996).

[13] Michael F. Corcoran. *X-ray Afterglow of a Gamma-Ray Burst: The Grail Found?* 2002. URL: `https://heasarc.gsfc.nasa.gov/docs/objects/heapow/archive/transients/grb_970228.html`.

[14] C. Dale et al. "Displacement damage effects in mixed particle environments for shielded spacecraft CCDs." In: *IEEE Transactions on Nuclear Science* 40.6 (1993), p. 1628.

[15] M. B. Davies, W. Benz, T. Piran, and F. K. Thielemann. "Merging neutron stars. 1. Initial results for coalescence of noncorotating systems." In: *The Astrophysical Journal* 431 (Aug. 1994), pp. 742–753. DOI: `10.1086/174525`. eprint: `astro-ph/9401032`.

[16] S. Dichiara et al. "Average power density spectrum of long GRBs detected with BeppoSAX/GRBM and with Fermi/GBM." In: *Monthly Notices of the Royal Astronomical Society* 431 (2013), p. 3608. DOI: `10.1093/mnras/stt445`. arXiv: `1303.2584`.

[17] *Discovery of a low-energy spectral breaks in prompt GRB spectra*. 2018. URL: `http://space.asu.cas.cz/~ewass17-soc/Presentations/S11/Oganesyan_619.pdf`.

[18] *ESA's SPENVIS*. 2018. URL: `https://www.spenvis.oma.be/`.

[19] E. Fenimore et al. "The intrinsic luminosity of gamma-ray bursts and their host galaxies." In: *Nature* 366 (1993).

[20] W. Fong, E. Berger, and D. B. Fox. "Hubble Space Telescope Observations of Short Gamma-Ray Burst Host Galaxies: Morphologies, Offsets, and Local Environments." In: *The Astrophysical Journal* 708 (Jan. 2010), pp. 9–25. DOI: `10.1088/0004-637X/708/1/9`. arXiv: `0909.1804 [astro-ph.HE]`.

[21] A.S. Fruchter et al. "Long γ-ray bursts and core-collapse supernovae have different environments." In: *Nature* 441 (May 2006), pp. 463–468. DOI: `10.1038/nature04787`. eprint: `astro-ph/0603537`.

[22] E. Gatti and P. Rehak. "Semiconductor drift chamber - An application of a novel charge transport scheme." In: *Nuclear Instruments and Methods in Physics Research. Section A: Accelerators, Spectrometers, Detectors and Associated Equipment.* A225 (1984), pp. 608–614. DOI: `10.1016/0167-5087(84)90113-3`.

[23] E. Gatti and P. Rehak. "Review of semiconductor drift detectors." In: *Nucl. Instrum. Meth.* A541 (2005), pp. 47–60.

[24] J. F. Graham and A. S. Fruchter. "The Metal Aversion of Long-duration Gamma-Ray Bursts." In: *The Astrophysical Journal* 774, 119 (Sept. 2013), p. 119. DOI: `10.1088/0004-637X/774/2/119`. arXiv: `1211.7068 [astro-ph.HE]`.

[25] *HERMES H2020*. 2018. URL: `http://www.dsf.unica.it/hermes/materiale_per_hermes_webpage/HERMES_Premiale_v19.pdf`.

[26] D. Heynderickx et al. “The ESA Space Environment Information System (SPENVIS).” In: *IAF abstracts, 34th COSPAR Scientific Assembly*. Jan. 2002, p. 475.

[27] Jens Hjorth et al. “A Very energetic supernova associated with the gamma-ray burst of 29 March 2003.” In: *Nature* 423 (2003), pp. 847–850. DOI: 10.1038/nature01750. arXiv: astro-ph/0306347 [astro-ph].

[28] R.W. Klebesadel and others. “Observations of Gamma-Ray Bursts of Cosmic Origin.” In: *Astrophysical Journal* 182 (June 1973), p. L85. DOI: 10.1086/181225.

[29] Glenn F. Knoll. *Radiation Detection and Measurement*. 111 River Street, Hoboken, NJ: John Wiley and Sons, Inc., 2010.

[30] Shiho Kobayashi, Tsvi Piran, and Re’em Sari. “Can internal shocks produce the variability in GRBs?” In: *The Astrophysical Journal* 490 (1997), pp. 92–98. DOI: 10.1086/512791. arXiv: astro-ph/9705013 [astro-ph].

[31] M. Korzhik et al. “Significant improvement of GAGG:Ce based scintillation detector performance with temperature decrease.” In: *Nuclear Instruments and Methods in Physics Research Section A Accelerators Spectrometers Detectors and Associated Equipment* 871 (2017).

[32] Erik Kulu. *nanosats.eu: World’s largest database of nanosatellites, over 2200 nanosats and CubeSats*. 2018. URL: https://www.nanosats.eu/.

[33] P. Kumar and B. Zhang. “The physics of gamma-ray bursts and relativistic jets.” In: *Physics Reports* 561 (Feb. 2015), pp. 1–109. DOI: 10.1016/j.physrep.2014.09.008. arXiv: 1410.0679 [astro-ph.HE].

[34] J. M. Lauenstein and J. L. Barth. “Radiation belt modeling for spacecraft design: model comparisons for common orbits.” In: *IEEE Radiation Effects Data Workshop, 2005*. 2005, pp. 102–109.

[35] Davide Lazzati and Gabriele Ghisellini. “Constraints on the bulk Lorentz factor in the internal shock scenario for gamma-ray bursts.” In: *Monthly Notices of the Royal Astronomical Society* 309 (1999), p. 13. DOI: 10.1046/j.1365-8711.1999.02970.x. arXiv: astro-ph/9907070.

[36] M. T. Lucchini and others. “Timing capabilities of garnet crystals for detection of high energy charged particles.” In: *Nuclear Instruments and Methods in Physics Research Section A Accelerators Spectrometers Detectors and Associated Equipment* A852 (2017), pp. 1–9. DOI: 10.1016/j.nima.2017.02.008.

[37] A. MacFadyen and S. E. Woosley. “Collapsars: Gamma-ray bursts and explosions in ’failed supernovae’.” In: *The Astrophysical Journal* 524 (1999), p. 262. DOI: 10.1086/307790. arXiv: astro-ph/9810274 [astro-ph].

[38] C. A. Meegan et al. “Spatial distribution of gamma-ray bursts observed by BATSE.” In: *Nature* 355 (1992).

[39] Astrophysics Science Division at NASA/ GSFC. *BATSE All-Sky Plot of Gamma-Ray Burst Locations*. 2012. URL: https://heasarc.gsfc.nasa.gov/docs/cgro/cgro/batse_src.html.

[40] E. Nakar and Tsvi Piran. “GRBs light curves - Another clue on the inner engine.” In: *The Astrophysical Journal* 572 (2002), pp. L139–L142. DOI: 10.1086/341748. arXiv: astro-ph/0202404 [astro-ph].

[41] Ramesh Narayan, Tsvi Piran, and Pawan Kumar. “Accretion models of gamma-ray bursts.” In: *The Astrophysical Journal* 557 (2001), p. 949. DOI: 10.1086/322267. arXiv: astro-ph/0103360 [astro-ph].

[42] G. Oganesyan, L. Nava, et al. “Detection of Low-energy Breaks in Gamma-Ray Burst Prompt Emission Spectra.” In: *The Astrophysical Journal* 846 (2017), p. 137. DOI: 10.3847/1538-4357/aa831e. arXiv: 1709.04689.

[43] Gor Oganesyan, Lara Nava, et al. “Characterization of Gamma-Ray Burst prompt emission spectra down to soft X-rays.” In: *Astronomy & Astrophysics* 616 (2018), A138. DOI: 10.1051/0004-6361/201732172. arXiv: 1710.09383.

[44] R. D. Preece et al. “The BATSE Gamma-Ray Burst Spectral Catalog. I. High Time Resolution Spectroscopy of Bright Bursts Using High Energy Resolution Data.” In: *The Astrophysical Journal Supplement Series* 126 (Jan. 2000), pp. 19–36. DOI: 10.1086/313289. eprint: astro-ph/9908119.

[45] M. Ruffert, H.-T. Janka, and G. Schaefer. “Coalescing neutron stars - a step towards physical models. I. Hydrodynamic evolution and gravitational-wave emission.” In: *Astronomy and Astrophysics,* 311 (July 1996), pp. 532–566. eprint: astro-ph/9509006.

[46] C. Segneri et al. “Measurement of the current related damage rate at -50C and consequences on macropixel detector operation in space experiments.” In: *2008 IEEE Nuclear Science Symposium Conference Record* (2008).

[47] A. M. Soderberg. “The Radio Properties of Type Ibc Supernovae.” In: *Supernova 1987A: 20 Years After: Supernovae and Gamma-Ray Bursters*. Vol. 937. American Institute of Physics Conference Series. Oct. 2007, pp. 492–499. DOI: 10.1063/1.3682950. arXiv: 0706.3047.

[48] Helmuth Spieler. *Semiconductor Detector Systems*. Great Clarendon Street, Oxford: Oxford University Press, 2005.

[49] G.P. Summers and others. “Damage correlations in semiconductors exposed to gamma, electron and photon radiation.” In: *IEEE Transactions on Nuclear Science* NS-40.1372 (1993).

[50] *TASTE*. 2018. URL: `https://taste.tuxfamily.org/`.

[51] G. Tamulaitis et al. “Subpicosecond luminescence rise time in magnesium codoped GAGG:Ce scintillator.” In: *Nuclear Instruments and Methods in Physics Research Section A: Accelerators, Spectrometers, Detectors and Associated Equipment* 870 (2017), pp. 25–29.

[52] S. Valenti et al. “The discovery of the electromagnetic counterpart of GW170817: kilonova AT 2017gfo/DLT17ck.” In: *The Astrophysical Journal Letters*, 848.2 (2017), p. L24. DOI: `10.3847/2041-8213/aa8edf`. arXiv: `1710.05854 [astro-ph.HE]`.

[53] K.C. Walker et al. “Gamma-Ray Bursts Have Millisecond Variability.” In: *The Astrophysical Journal* 537 (July 2000), pp. 264–269. DOI: `10.1086/308995`.

[54] S. E. Woosley. “Gamma-ray bursts from stellar mass accretion disks around black holes.” In: *The Astrophysical Journal* 405 (Mar. 1993), pp. 273–277. DOI: `10.1086/172359`.

[55] M. Yoneyama et al. “Evaluation of GAGG:Ce scintillators for future space applications.” In: *Journal of Instrumentation* 13.02 (2018), P02023.

[56] B.B. Zhang et al. “A Comprehensive Analysis of Fermi Gamma-ray Burst Data. I. Spectral Components and the Possible Physical Origins of LAT/GBM GRBs.” In: *The Astrophysical Journal* 730, 141 (Apr. 2011), p. 141. DOI: `10.1088/0004-637X/730/2/141`. arXiv: `1009.3338 [astro-ph.HE]`.

[57] Cherenkov Telescope Array Observatory gGmbH. *Building the world’s most advanced ground-based gamma-ray observatory*. 2016. URL: `https://www.cta-observatory.org/project/`.